

Dissertation
submitted to the
Combined Faculties for the Natural Sciences and for Mathematics
of the Ruperto-Carola University of Heidelberg, Germany
for the degree of
Doctor of Natural Sciences

Put forward by
Dipl. Phys. Dorothea Sauter
Born in Würzburg, Germany
Oral examination: June 24th 2009

4Pi live cell imaging

Referees:

Prof. Dr. Stefan W. Hell
Prof. Dr. Rainer H. A. Fink

Kurzdarstellung

Ein entscheidender Vorteil eines Lichtmikroskops gegenüber einem Elektronenmikroskop besteht darin, selektiv und dreidimensional subzelluläre Details in lebenden Zellen abzubilden. Die Abbildung lebender Zellen ist eine Domäne der Lichtmikroskopie. In dieser Promotionsschrift wird ein Aufbau zur Lebendabbildung vorgestellt, welcher auf 4Pi Fluoreszenz-Mikroskopie basiert. Um die Aufnahmegeschwindigkeit dahingehend zu steigern, die Aufnahme von zellulären Prozessen auf der Sekundenskala zu ermöglichen, wird eine neue Methode, mehrere parallele Foki mit Hilfe aufeinandergestapelter, doppelbrechender Kristalle zu erzeugen, angewandt. Das System verfügt über eine axiale Auflösung von ≈ 120 nm und die Aufnahme eines durchschnittlichen 3D-Datenstapels dauert nicht länger als 10 Sekunden. Die Eignung des Mikroskops für die Abbildung lebender Zellen wird verifiziert: sowohl mitochondriale Vereinigungs- und Trennungsprozesse in lebenden Hefen, als auch die Bewegung von PML Körpern in lebenden menschlichen U2OS Zellen wurden aufgenommen. Um die Grenzen der Anwendbarkeit des Systems weiterzustecken, werden sowohl die Erzeugung der zweiten Harmonischen als ein alternativer, markerefreier und kohärenter Kontrastmechanismus untersucht als auch binäre Amplitudenfilter implementiert. Die Erzeugung der zweiten Harmonischen stellt sich als Abbildungstechnik heraus, die auf spezifische Anwendungen begrenzt ist. Durch die Implementierung von Amplitudenfiltern wird 4Pi Mikroskopie von wasserhaltigem Gewebe praktisch und breit anwendbar.

Abstract

One distinctive advantage of light microscopy over electron microscopy is its ability to selectively image sub-cellular details three-dimensionally in living cells. Live cell imaging is the domain of light microscopy. In this thesis a live cell imaging setup relying on 4Pi fluorescence microscopy is presented. To speed up the imaging process and record cellular processes of the order of a few seconds a new method of multifoci-generation via the stacking of birefringent crystals is implemented. The axial optical sectioning ability of the system is ≈ 120 nm and the recording of an average-sized 3D data stack is accomplished in less than 10 seconds. The microscope's applicability to live cell imaging is verified by recording both mitochondrial fusion and fission events in live yeast and the movement of PML bodies in live human U2OS cells. To push the limits of applicability of the system further, second harmonic generation is tested as an alternative label-free coherent contrast mechanism and binary amplitude filters are successfully applied. Second harmonic generation turns out to be an imaging technique confined to specific applications. With the implementation of amplitude filters 4Pi microscopy of aqueous tissue becomes convenient and broadly applicable.

Contents

. List of abbreviations	IX
. List of figures	XII
1. Introduction	1
2. Spot multiplication in MMM	3
2.1. Multifocal multiphoton microscopy (MMM)	4
2.2. Experimental setup	8
2.3. Birefringent crystals	13
2.4. Experimental results	18
3. Second harmonic generation (SHG)	33
3.1. Nonlinear dielectric susceptibilities	34
3.2. Generalized theory: 4Pi type C illumination driven SHG	36
3.3. Simulations of SHG Intensity PSFs	37
3.4. Imaging of muscular actomyosin	42
3.5. Summary	46
4. Challenges in live cell microscopy	49
4.1. Imaging with water immersion objectives	49
4.2. Summary	58
5. Conclusion and Outlook	61
A. Advantages of the xz -scan option for wide-field detection	63
B. Mode of scanning and respective field of view	65
C. Algorithm for interactive removal of the axial sidelobes	69
. Acknowledgments	83

List of abbreviations

4Pi microscopy	Microscopy relying on the coherent addition of opposing focused wavefronts
APD	Avalanche Photo Diode
A.U.	Arbitrary Units
BS	Beamsplitter
CCD	Charge Coupled Device
(c/c)	constructive excitation, constructive detection
(c/d)	constructive excitation, destructive detection
(d/c)	destructive excitation, constructive detection
(d/d)	destructive excitation, destructive detection
FWHM	Full-Width at Half-Maximum
I ⁵ M	Incoherent Illumination Interference Image Interference Microscopy
k _c	Critical frequency, first minimum of the OTF
λ _{exc}	Excitation wavelength
λ _{det}	Detection wavelength, center of emission spectrum
MMM	Multifocal Multiphoton Microscopy
NA	Numerical Aperture
OTF	Optical Transfer Function, Fourier transform of the PSF
PALM	Photo-Activated Localization Microscopy
PML-NB	Promyelocytic leukemia Nuclear Body
PMT	Photomultiplier Tube
PSF	Point Spread Function
STED	Stimulated Emission Depletion
SW(F)M	Standing Wave (Fluorescence) Microscopy
TDE	2,2'-Thiodiethanol

List of Figures

2.1.	16 spots, two-photon image of a fluorescent mono-layer	9
2.2.	16 spots in tiled scan mode	10
2.3.	Sketch of the experimental setup	11
2.4.	Sketch of birefringent crystals creating multiple focal spots.	15
2.5.	Photography of the experimental setup	16
2.6.	Spot multiplication in a Wollaston prim	17
2.7.	xz -slice of a yeast cell before sidelobe removal.	19
2.8.	xz -slice of a yeast on top of a dense layer of fluorescent beads.	20
2.9.	Time-series of a first living yeast.	21
2.10.	Time-series of the first living yeast from another point of view.	23
2.11.	Time-series of a second living yeast.	24
2.12.	Time-series of the second living yeast seen from another perspective.	25
2.13.	Single PML-NB in magnification	27
2.14.	Time-series of PML NBs.	29
3.1.	Simulations of a single collagen point scatterer in the origin	38
3.2.	Simulation of four collagen point scatterers	40
3.3.	SHG intensity dependence on object size	41
3.4.	Sketch of the principle beam path of the 4Pi microscope.	43
3.5.	xy -images of fibrillar myosin	44
3.6.	Simulations of a single myosin point scatterer in the origin	45
3.7.	xz -images of fibrillar myosin	47
4.1.	Sketch of pupil function filtering in a 4Pi microscope	51
4.2.	Two-photon aperture-filter image of microtubules.	52
4.3.	Two-photon dark-ring image of microtubules	53
4.4.	Single-photon dark-ring image of microtubules	54
4.5.	Single-photon dark-ring image of microtubules after removal of the axial sidelobes.	56
4.6.	3D single-photon dark-ring image of microtubules	56
A.1.	4Pi beamsplitting device	64
B.1.	Sketch of focal spots in tiled scan arrangement	66
B.2.	Sketch of the focal spots in interleaved scan mode	67

1. Introduction

Far field fluorescence confocal microscopy ([106], [94], [93]) is now the established state of the art technique for imaging biological tissue because of its ability to resolve subcellular details noninvasively in 3 dimensions (3D). Yet the resolution of a confocal microscope is diffraction limited. The full width at half maximum (FWHM) of its point spread function (PSF), i.e., the system's image of a fluorescent point, is largely determined by $1/2$ the (visible) wave length and thus exceeds 200 nm in the focal plane (x,y) and even 500 nm along the optical axis (z) due to an asymmetry in the convergence of the focused wave front.

New techniques such as 4Pi microscopy ([60], [59], [100], [50]) and I^5M ([54]) overcame this limit: Enlarging the effective axial numerical aperture of the imaging system by coherent addition of the spherical wavefronts of two opposing lenses reduced the PSF 3–7 fold down to 100 nm. These techniques, though operating at the edge of established light microscopy are still diffraction limited.

Only recently have light microscopic techniques been developed that are not resolution limited in principle. They can roughly be divided into two groups. ‘PSF engineering’ methods such as the stimulated emission depletion microscopy (STED) which confines the net fluorophore emission to the immediate proximity of the PSF center ([62], [66], [76], [34]). This is accomplished by overlaying the diffraction limited PSF with an also diffraction limited doughnut-shaped intensity distribution. Utilizing reversible intramolecular transitions ([61], [22], [64]) of the fluorophores fluorescence emission is prohibited throughout the PSF apart from the regions which do not overlap with the doughnut, i.e., the PSF's very center. This technique of improving the system's resolution by shrinking the effective size of the PSF, i.e., read out a targeted region within the sample, is a genuinely physical one.

The second group are the ‘localization’ methods. In techniques like PALM ([111], [6], [39], [69], [41]), they try to enhance resolution by stochastic readout and mathematical localization. Only single photochromic molecules are reversibly transferred to the ‘on’ state by for example faint far-field illumination and thus it is ensured that all emitted photons in a conventional diffraction limited PSF belong to this one molecule which therefore can be mathematically localized with high lateral accuracy. However, for dynamic processes in living cells happening on short to medium time scales (nanoseconds to minutes) this method is unfit. Imaging every single molecule of a fluorescent molecular ensemble requires the ensemble to be fixed in space at least during the read-out process. Else the signal of a ‘new’ molecule and that of a molecule already imaged and just drifted or diffused to another location in the specimen to be

1. Introduction

excited there are not distinguishable. Another drawback is the necessity to reduce background noise as much as possible. Therefore, a detection threshold has to be set which limits the choice of fluorophores not only to those switchable, they also have to be bright and long cycling. To further reduce background from autofluorescence and/or scattering from thick layers of tissue localization microscopy has so far only been deployed for thin layers or slices of cells closely attached to the cover slip ([70]).

Consequently, in live cell imaging the technically elaborate ensemble methods of PSF engineering are to be preferred and, indeed, have been applied successfully [57], [125].

4Pi microscopy is a reliable three-dimensional imaging technique. Starting as a laboratory imaging setup it has been commercialized some years ago. Although the 4Pi's diffraction limited resolution is overcome by imaging techniques like STED or PALM it is still the best starting point to extend these microscopy methods to three dimensional analysis. Only recently IsoSTED (4Pi augmented STED) succeeded in generating a perfectly spherical PSF featuring a FWHM of down to 30 nm [114], albeit it has been deployed only for fixed samples for the time being.

4Pi microscopy was first adapted to two-photon live cell imaging by Egner et al. and Bewersdorf et al. [37], [10], [38]. The sector of live cell imaging is rapidly growing in importance. In order to speed up the imaging process of a conventional 4Pi microscope and record cellular processes of the order of a few seconds accurately, multiple parallel foci scanning the sample simultaneously have to be created out of one initial laser raster beam. In this thesis the conceptually new method of multispot-generation via the stacking of birefringent crystals is consequently implemented for the first time in a 4Pi multifocal multi-photon microscopy setup.

The generation of the multispots via birefringent crystals is described in detail in the first chapter. The versatility of the presented setup for live cell imaging is demonstrated recording fusion and fission processes in living yeast and the movement of PML bodies in living human osteosarcoma cells U2OS.

Another big challenge in live cell microscopy poses the staining of living cells. To avoid limitations arising from the poor availability of dyes (a) suitable for live cells and, in addition, (b) with an adequate multiphoton cross-sectional spectrum the second chapter deals with the examination of the abilities and limitations of an alternative contrast mechanism not requiring dyes: second harmonic generation [68], [46], [47].

The last chapter treats remaining problems arising from imaging with water immersion objectives. Due to the smaller aperture angles of these compared to oil immersion objectives 4Pi axial sidelobes exhibit increased sidelobes thus impeding or even inhibiting reliable image restoration. Furthermore, due to an inherent refractive index mismatch of living specimen and aqueous embedding medium specimen-induced aberrations effect the imaging quality of a 4Pi system significantly. Solutions to these problems are proposed and successfully implemented.

2. A new method of spot multiplication in Multifocal Multiphoton Microscopy (MMM)

4Pi microscopy has long proven its versatility and importance in three-dimensional high resolution imaging of fluorescent labelled fixed as well as living biological tissue [65], [38], [37], [10], [91], [74], [115].

In 4Pi microscopy the excitation light of a conventional confocal laser raster-scanning microscope is split in two halves by a beamsplitter and focused into a common focal spot in the sample by two objective lenses of high numerical aperture (NA). The opposing spherical wavefronts add up coherently in the focus and the excitation emitted is collected by the two objectives and merged at the beamsplitter before it is detected. 4Pi microscopy of type A refers to coherent illumination and incoherent detection, 4Pi microscopy of type B to incoherent illumination and coherent detection and 4Pi microscopy of type C refers to the case of both coherent illumination and detection [50], [12].

A microscope's image $i(\vec{r})$ of an object $o(\vec{r})$ is mathematically the convolution of the imaged object with the microscope's point spread function $h(\vec{r})$:

$$i(\vec{r}) = h(\vec{r}) \otimes o(\vec{r}). \quad (2.1)$$

The effective point spread function of a 4Pi fluorescence microscope is the product of the respective point spread functions for illumination and detection. The coherent point spread function is

$$h_{\text{coh}}^{\text{ill/det}} = \|\vec{E}_1(z, r, \phi) + \vec{E}_2(-z, r, -\phi)\|, \quad (2.2)$$

\vec{E}_i being the fields of the two opposing waves. These are

$$\vec{E}_i = \begin{pmatrix} -iA(I_0 + I_2 \cos(2\phi)) \\ -iAI_2 \sin(2\phi) \\ -2AI_1 \cos(\phi) \end{pmatrix}, \quad (2.3)$$

with the integrals I_0, I_1, I_2 over the aperture angle α of the objective lenses computed according to the well-known equations by Richards and Wolf [108].

The microscope's resolution is proportional to the full width at half maximum (FWHM) of the effective PSF. In 4Pi microscopy the lateral resolution is, strictly

2. Spot multiplication in MMM

speaking, that of a conventional confocal microscope. Yet the axial resolution is 3 – 7-fold increased compared to the confocal one [50]. Thus the crucial benchmark in 4Pi microscopy is the axial resolution which is generally referred to as the system's z -response

$$I(z) = \int_0^\infty \int_0^{2\pi} h_{\text{eff}}(\vec{r}) r \, dr \, d\phi. \quad (2.4)$$

Alternatively the Fourier transform of the point spread function, the optical transfer function (OTF), is taken to define the system's resolution abilities:

$$H(\vec{k}) = \widetilde{h(\vec{r})}. \quad (2.5)$$

In contrast to 4Pi microscopy where an increase in total focusing aperture is gained by the coherent superposition of (focused) spherical wavefronts of two opposing high-aperture objective lenses systems similarly aiming for an improved axial resolution like the standing wave microscope (SWM) [2], [86] or the I⁵M microscope [54], [53], [52] rely on the coherent superposition of flat standing waves. Gaps in the passband of transferred frequencies in the OTF as exhibited by the SWM and the I⁵M are proof of the poorer information transfer ability of these systems [50], [101], [11]. The critical frequency k_c is a benchmark to which degree an imaging system is able to transfer structural information about the physical object to the image. A 4Pi microscope exhibits a complete passband of frequencies within its inner region of support [50]. The axial resolution of a 4Pi microscope of type C is about 100 nm depending on the mode of detection (widefield/confocal).

2.1. Multifocal multiphoton microscopy (MMM)

Unfortunately 4Pi microscopy relying on raster-scanning suffers from a poor time resolution since scanning the sample point by point is a time-consuming procedure. Therefore, to image processes in living cells taking place on short time-scales (some seconds to some minutes), it is essential to speed up data acquisition.

The utilization of several parallel foci would speed up the imaging rate considerably.

Several ways have been proposed to create multiple excitation beams out of one initial laser beam [13], [122], [24], [44], [45], [102], [40], [73], [112], [43], [87], the most prominent being the microlens array approach [24], [44], [122] and the cascade of mirrors approach [102], [87].

The first method, creating several parallel foci via an array of microlenses in the illumination path, certainly achieves impressive frame rates of typically 300 - 400 frames per second (fps), [36], owing to the fact that the microlenses are arranged on a fast rotating disc thus avoiding dead times. Nevertheless the microlens approach suffers from a poor excitation light efficiency and residual optical aberrations due to the inevitable beam expansion on the microlenses and imperfect micro lens optics

[13], [24], [8]. Furthermore it suffers from the nonuniformity of the generated foci due to the influence of the incident laser beam profile on the intensity distribution over the created pattern of beamlets [24].

The latter approach, generating multiple parallel foci via a cascade of mirrors in the illumination path, surely improves the uniformity of the created foci and the efficiency of incident light usage [102]. The main advantage of this approach though is the inherent minimization of cross-talk which deteriorates the imaging system's axial resolution due to an overlap and interference of excitation/detection channels of neighboring foci. The different beamlets have different path lengths through the beamsplitting device causing a certain temporal delay between them, i. e., the beamsplitter has a 'built-in' time mask. The drawbacks of this method are the intricate and time-consuming adjustment of the mirrors for an optimal beamsplitting device, the lower imaging speed due to a not non-descanned detection mode [102] and a noticeable intensity distribution over the pattern of generated foci due to the mirror's different reflection properties for P- and S-polarized light.

In this chapter a novel way of live cell 3D imaging is presented which is both fast and axially superresolving: Combining the advantages of both multiphoton 4Pi illumination and a high-performance wide-field detector with a fundamentally new method of multispot generation in multifocal multi-photon microscopy (MMM) history via birefringent crystals a powerful, convenient and reliable optical live cell setup was built allowing for the recording of 3-dimensional data stacks within some ten seconds depending on the stack's dimensions and an axial resolution of ≈ 120 nm. This is demonstrated recording fusion and fission events of the mitochondrial network of the yeast *S. cerevisiae* as well as the dynamics of promyelocytic leukemia nuclear bodies in human osteosarcoma cells U2OS.

2.1.1. Advantages of two photon microscopy in live cell imaging

Visualizing the dynamics of spatially extended living structures requires fast and repeated recording of the region of interest. Concerning the amount of information, i.e., fluorescence photons, that can fundamentally be extracted from a specimen in fluorescence microscopy one factor that has to be considered in detail is photobleaching. This is especially true for repeated 3-dimensional scans of the very same region. As far as bleaching can be expected to be a linear process [27], [30], i.e., for moderate excitation intensities of some kW/cm^2 in the focus, the sample bleaches uniformly throughout the axial (z) extent of the excitation PSF [83], which is for example ≈ 500 nm in single photon 4Pi microscopy (the sectioning in confocal microscopy is achieved only in the course of detection).

In two-photon microscopy [31], [80] two photons excite in a single quantum event a fluorophore. The fluorophore emits by returning to the ground state a single photon of double frequency modulo Stokes shift (difference between excitation and emission wavelengths due to energy losses in the sample). Two-photon microscopy exhibits

2. Spot multiplication in MMM

increased nonlinear photobleaching [105]. Photobleaching due to multi-photon excitation eventually exceeds in-plane bleaching due to single photon excitation for equal amounts of fluorescence emitted [105]. On the other hand multi-photon excitation has several advantages:

- Nonlinear absorption of two photons *per se* restricts both the fluorescence emission and the photobleaching to the focal plane and thus the overall bleaching of a 3-dimensional two-photon image optically sectioned to a high degree is drastically reduced compared to single photon imaging.
- Furthermore near infrared light, used for two-photon excitation, is less scattered than visible light in thick tissue and therefore exhibits a greater penetration depth than single photon excitation.
- In addition the two photon microscopy's inherent sectioning ability cancels the necessity for backimaging the signal on a confocal pinhole thus relaxing design constraints of the scanning device: It was shown [50] that the optical transfer function (OTF) of a 4Pi microscope of type C exhibits a complete passband of frequencies within its inner region of support and thus this imaging technique robustly renders three-dimensional images with axial superresolution possible. This fact, most importantly, holds true even without the confocal pinhole.

In direct consequence of the latter item an efficient wide-field detection unit was implemented into the setup: A high-performance back-thinned charge coupled device (CCD) camera with a quantum efficiency of up to 90% was employed for wide-field detection. In this non-descanned mode of detection the detector needs to be read out only after the acquisition of a whole frame and not for every position of the scanner and a better signal-to-noise ratio is obtained compared to that of the respective confocal detector.

2.1.2. Parallelized microscopy reduces acquisition time

In order to enhance the 4Pi's capabilities of recording fast dynamics the scanning procedure has to be sped up. Increasing the rate of raster-scans though is equivalent to shorten the exposure time and reducing the number of excitation events. A lower signal on the other hand will not only lead to a loss of low-contrast features of the fluorescence image but also emphasizes Poisson-noise non-proportionally. To avoid these unwanted features an appropriate counteraction could be to increase the excitation intensity proportionally. Indeed, focusing the light of a femtosecond Ti:Sa laser, which produces laser pulses with a nominal pulse width of 30 fs and a peak power of 2.8 W (at $\lambda = 800$ nm), with NA 1.2 water immersion objectives, the excitation intensity in the focal region is virtually unlimited.

Increasing the excitation intensity, however, will eventually lead to a saturation of the fluorophores' excited singlet state. Dyes exhibiting a certain quantum yield for inter-system crossing will exhibit decreased fluorescence upon high excitation intensities since a considerable number of dye molecules is able to cross from the singlet excited state with a lifetime of $\approx 10^{-9}$ s to the long-lived triplet excited state and is therefore lost for detection on fluorescence emission time-scales. Furthermore, at high excitation intensities chemical species such as reactive oxygen are generated in the specimen [32]. Interactions of triplet oxygen and dye molecules in the excited triplet state generate singlet oxygen which has a lifetime similar to that of the excited triplet state of the dye ($\approx 10^{-6}$ s). Singlet oxygen oxidizes the dye molecules and even components of the cells and thus is not only a source of photobleaching but also of phototoxicity [32], [79].

Thus, in order to prevent nonlinear photobleaching, phototoxicity and photodamage (such as DNA strand breaks) [79] in the specimen, the amount of the maximal allowable focal pulse intensity has to be limited [9], [58] to $\approx 100 - 300$ GW/cm² for 100 – 200 fs pulses [24], [78], which for the Ti:Sa laser and the high-NA objectives described corresponds to 13 – 40 mW of time-averaged power in the focal plane. Experiments suggest ≈ 10 to 15 mW to be the upper limit of allowable time-averaged power in the focal plane though. Admittedly this is just a rough estimation for a specific sample because the individual threshold greatly depends on the respective fluorophores involved, the specific embedding medium and the sample itself (technical/fixed/living). Nevertheless exciting fluorescence with focal power intensities greatly exceeding ≈ 10 mW first will lead to photobleaching before damaging or even destroying the sample in the long run and thus more than 90% of the total time-averaged power of the Ti:Sa laser is lost for multiphoton excitation.

Faster recording becomes possible splitting up the beam into N beamlets of powers each not exceeding the maximum allowable focal intensity described above and in this way yielding N times the amount of fluorescence signal. Thus parallelization not only speeds up scanning considerably by a factor of N but also optimizes the efficiency of excitation light usage.

2.1.3. Crosstalk does not affect axial superresolution

If the number of spots is increased, the PSFs of neighboring spots may eventually interfere. This so-called crosstalk is an effect counteracting the optimization of excitation efficiency by parallelization [118], [90]: The lobes of overlapping coherently illuminated adjacent PSFs possibly interfere constructively and that in consequence leads to planes of reinforced excitation and bleaching axially shifted to the focal plane. In consequence thereof the axial superresolution of the MMM-4Pi is deteriorated. This holds, of course, also true for detection PSFs.

If crosstalk effects are to be expected, time-multiplexing can be a way of eliminating these [36]: Changing the optical pathways for pulses of neighboring foci ensures

2. Spot multiplication in MMM

excitation and detection of two neighboring PSFs to take place at different times and thus inhibits overlapping PSFs, especially in depth.

Mathematically the 4Pi type C MMM - system is according to [36] described by the effective PSF

$$H_{\text{eff}}(x, y, z) = [h(\varepsilon x, \varepsilon y, \varepsilon z)]^2 \cdot I_z(z).$$

$$I_z(z) = \iint [h(x, y, z) \otimes g(x, y, z)]^4 \, dx \, dy \quad (2.6)$$

denotes the z -response of the system, $\varepsilon = \frac{\lambda_{\text{ex}}}{\lambda_{\text{em}}}$ the ratio of excitation and emission wavelength, $h(x, y, z)$ the amplitude PSF as given in 2.2 and

$$g(x, y, z) = \sum_{n=1}^N \delta(x - x_n) \delta(y - y_n) \delta(z)$$

the grating function describing the coordinates of the array of foci. \otimes indicates the convolution operation, δ is Dirac's Delta function and the exponent 4 in Equation 2.6 marks two photon excitation. For a sparse grating,

$$x_i - x_{i-1} \gg \lambda\sqrt{N} \quad \text{and} \quad y_i - y_{i-1} \gg \lambda\sqrt{N},$$

interference effects are no longer to be considered and Equation 2.6 takes the simple form:

$$I_z(z) = N \iint [h(x, y, z)]^4 \, dx \, dy.$$

The MMM-4Pi's z -response is that of a single beam two photon excitation microscope, brighter by a factor of N . In short: the axial resolution for a MMM-4Pi with sparse grating is not harmed by crosstalk effects.

2.2. Experimental setup

In the setup used for multifocal multiphoton microscopy 2 – 16 focal spots are generated displaying a minimum distance of

$$x_i - x_{i-1} \geq 4.8 \, \mu\text{m} \geq \lambda\sqrt{N} \quad \text{and} \quad y_i - y_{i-1} \geq 4.8 \, \mu\text{m} \geq \lambda\sqrt{N},$$

thus generating a field of view of $\approx 28 \, \mu\text{m} \times 36 \, \mu\text{m}$ in tiled scan mode, see appendix section B. The focal spots in this arrangement are seen in Fig. 2.2.

The MMM-4Pi's axial superresolution is therefore not corrupted in this experimental setup which is convincingly shown in Fig. 2.1. Although slightly overlapping scan-regions create a grid-like structure in the xy -image, the z -profiles of 4 regions of interest, arbitrarily picked out, do not vary much. Indeed, measuring samples others than uniformly fluorescent layers, the grid-like structure is not any longer observed.

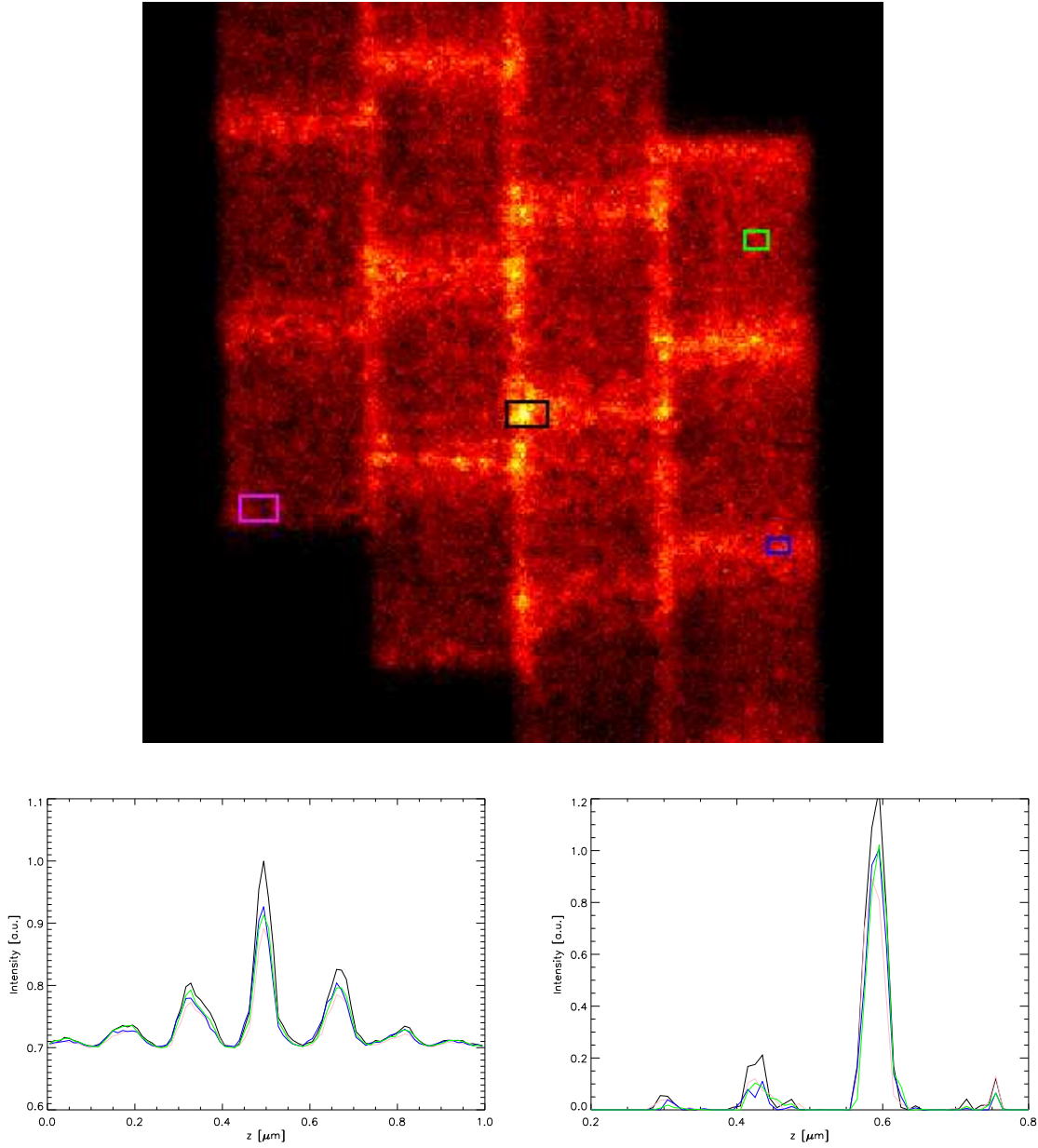


Figure 2.1.: 3D image-stack of a mono-layer of qdots515. The stack was recorded by xy -scanning while the sample was moved along z . *Top*: xy -image of the fluorescent layer of qdots. The rhombus – shaped form of the scanned area in tiled scan-mode is clearly visible. The image area is $36\,\mu\text{m} \times 36\,\mu\text{m}$. Adjacent scanned areas overlap slightly and create a chess-board pattern. This pattern is only clearly visible in uniform samples of ultra-thin fluorescent layers though. *Bottom left*: z -profiles of arbitrarily picked regions as lined out in the left image. Although the regions of interest picked out in the xy -slice show maximal variance concerning their brightness and localization within the field of view, the respective z -profiles exhibit only slight variances. *Bottom right*: z -profiles of the regions of interest as marked in the left image after simple 3 point deconvolution and subtraction of 15% of the background.

2. Spot multiplication in MMM

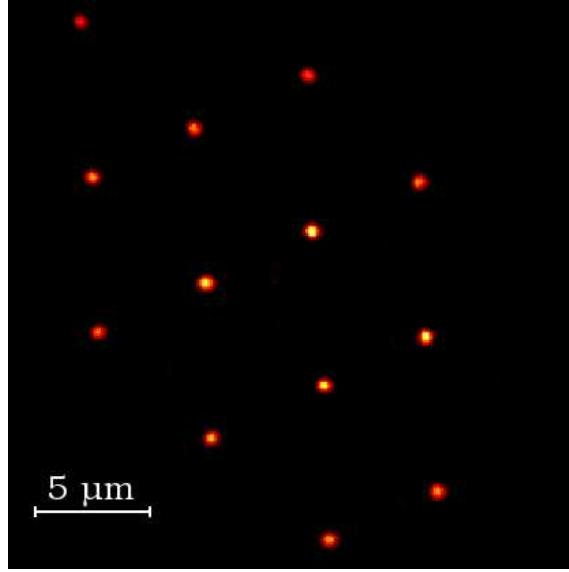


Figure 2.2.: xy -image of the focal spots in tiled scan mode. The minimum distance between neighboring spots is $4.8\text{ }\mu\text{m}$.

Deconvolution is successfully conducted by simple 3point filtering: the MMM-4Pi's axial superresolution is not deteriorated by crosstalk.

The beam of a mode-locked Ti:Sa laser (Chameleon Ultra, Coherent, Palo Alto, CA) passes an acousto-optical modulator and a polarizer before being coupled into the scanner of a standard confocal microscope (TCS SP2, Leica Microsystems, Mannheim) via the IR-port. The acousto-optical modulator provides constant illumination intensities throughout the scanned area blanking the incident light during laser fly-back. The polarizer is adjusted to ensure linearly polarized excitation light. The heart of the MMM-4Pi setup, see Fig. 2.3, consists of a home built 4Pi head mounted on the microscope turret of the confocal microscope stand featuring a free accessible conjugated pupil.

Therein a stack of Wollaston prisms is placed. Each prism doubles the number of incoming beamlets in the way described in more detail below.

The beam, multiplied by the Wollaston-prisms, see Fig. 2.4, is divided by the beamsplitter and focused into the sample by two opposing objective lenses (Leica HXCL63x/1.2 water immersion objectives, one to use with and one without (dipping) coverslip), where the opposing wavefronts add up coherently. In order to adjust the 4Pi microscope to type C mode optical path differences between excitation and emitted fluorescence light caused by dispersion mismatch have to be compensated. For this purpose a pair of glass wedges (NSF10) is inserted in one arm of the 4Pi head while in the other a glass block of equal mean thickness is placed for compensation.

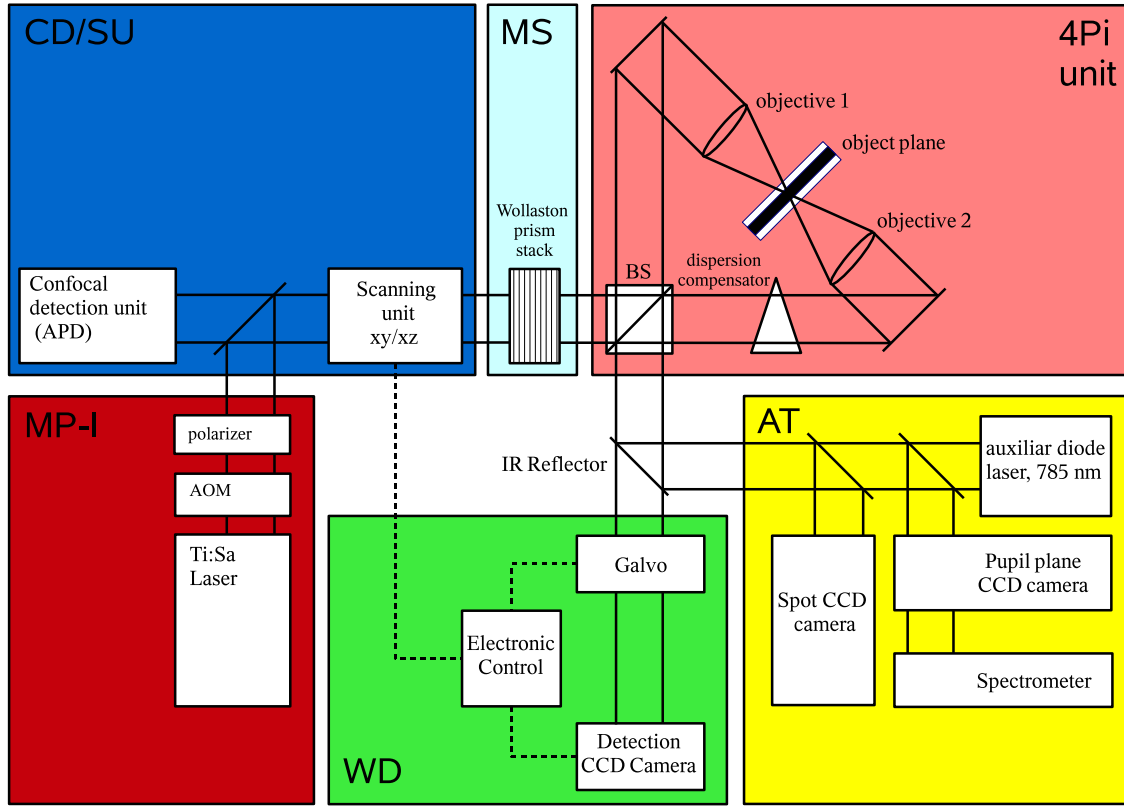


Figure 2.3.: Sketch of the experimental setup. The setup can be roughly divided in 6 separate subunits: The heart of the setup is a confocal laserscanner consisting of a microscope (not shown), the scanning unit *SU* and the confocal emission detector *CD*. The second subunit is a 4Pi head, mounted on the confocal microscope's turret instead of the microscope's default built-in revolver and table. Multiphoton illumination is provided by a third sub-part, the *MP-I* - unit and detection of the emitted fluorescence in a wide-field scheme is accomplished by the wide-field detector, *WD*, a back-thinned CCD. For the generation of multiple spots, *MS*, a stack of Wollaston - prisms is mounted in the free accessible pupil space of the microscope. A last sub-unit is the auxiliary toolbox, *AT*, consisting of an auxiliary laser diode and auxiliary cameras providing for proper adjustment and stabilization of the 4Pi optics.

2. Spot multiplication in MMM

The fluorescence is collected by the two objective lenses and combined at the beamsplitter. The part leaving its non-confocal output is coupled out of the 4Pi module, passes a short pass dichroic mirror and is finally imaged onto a back-thinned charge-coupled device (CCD) camera (iXon512, Andor, Puchheim, Munich). The part of the signal leaving the beamsplitter's second output reenters the confocal scanner, gets descanned, before it is focused on a pinhole. Therefore this output is referred to as the beamsplitter's confocal output. In this setting the detection beam passes also the stack of prisms which results in extremely poor signal efficiency since the prisms are aligned for linearly polarized excitation light rather than randomly polarized fluorescence light. Detection was conducted therefore without exceptions via the nonconfocal output. Of course the setup could be modified in order to avoid the fluorescence to pass the stack of prisms again, backimage the multiple fluorescence beamlets onto a pinhole array and detect them with an array of APDs. This procedure though would be absolutely inefficient and is therefore more a theoretical possibility.

To facilitate the alignment and provide for the stabilization of the objectives' positions (such that they focus on the very same spot in the sample) auxiliary tools have been integrated: the light of an auxiliary diode laser (785 nm, Roithner, Vienna) is coupled into the 4Pi system via the beamsplitter's nonconfocal output. Taking the same path as the excitation light a part of it is coupled out again at the beamsplitter and after reflection on the short pass dichroic mirror is imaged onto an auxiliary CCD camera (Philips ToUcam), the spotCCD. Lateral misalignments of the auxiliary laser (and thus the system) are indicated at the spotCCD by two separated spots. Perfect alignment merges the spots and the alignment was stabilized by an algorithm maximizing spot intensity. Other auxiliary alignment tools are the spectrometer (AvaSpec, Ocean Optics, Florida) used for the alignment of constant phase over the wavelength λ for type C [84] and another auxiliary CCD camera (Philips ToUcam) in a pupil plane of the system needed for the first coarse manual alignment of the objectives' positions when a new sample is put in: spherical or astigmatic aberrations caused by a tilted sample are indicated by a S-shaped interference pattern. Furthermore a galvanometric mirror was added in the non-confocal detection beam path controlled by the confocal microscope's scan signal when scanning along the optic (z) axis. Axial scanning in the confocal microscope is performed by moving the sample along z for a certain lateral position (X, Y) but since the fluorescence detected at the CCD camera is not de-scanned this will result in the signal's projection onto the according point in the image plane $P(X, Y)$ of the detector. The tilt movement of the galvanometric mirror now stretches the fluorescence image projection according to the sample's movement along z and thus sort of performs z -scans of the fluorescence beamlet array across the CCD. The option to perform xz -scans in wide-field detection is especially helpful to align the system to the preferred case of constructive interference for both detection and excitation light, see appendix, section A.

2.3. birefringent crystals: a novel way of beam multiplication in multifocal multiphoton microscopy

2.3.1. Stacking birefringent crystals generates multiple beamlets

In the presented setup a stack of Wollaston prisms is placed in the beam path near a pupil plane of the scanner at the entrance aperture of the objectives. The prisms are built out of machine-shop-fabricated optical grade silica crystal wedges (SiO_2), which exhibit only little dispersion. Silica is a positive uniaxial birefringent crystal: the refractive index (extraordinary index n_e) along one of the crystal's principal axes, the so-called optical axis, differs from the ones (ordinary refractive index n_o) along the other two principal axes. Thus an electromagnetic wave passing through the material displays different velocities for its components parallel and perpendicular to the crystal's optical axis. For quartz $n_e = 1.553 > 1.544 = n_o$ [4].

In this way an incident light beam is split up into the so-called ordinary and the extraordinary beam. The ordinary beam is polarized perpendicular to both the material's optical axis as well as the propagation direction of the beam. The extraordinary beam is polarized in the plane spanned by the incident beam's propagation direction and the crystal's optical axis and thus perpendicular to the ordinary one.

Each Wollaston prism consists of two silica wedges cemented together at their hypotenuses, with their optical axes being perpendicular to each other. The optical axis of one of the wedges is parallel and the one of the other wedge perpendicular to the prism's surface, see Fig. 2.4. The polarization components of an incident beam, polarized parallel and perpendicular to the prism's surface, thus will differ in speed but not direction of propagation upon entering the first wedge. Due to refraction at the quartz-quartz interface the beam is tilted though upon entering the second wedge and thus the polarization components are not any longer exactly parallel and perpendicular to the second wedge's optical axis. Due to the birefringent properties of the second silica wedge the beam is splitted in two beamlets, one of them polarized perpendicular to the second wedge's optical axis, the other's polarization being in the plane spanned by the second wedge's optical axis and the propagation direction of the incident beam. Two beamlets emerge the Wollaston prism.

In the case of the presented setup, there is a comfortable amount of free accessible pupil space. Only 4 prisms were used to generate up to 16 uniform beamlets. The spot multiplication can be continued as long as required by adding further prisms. Yet when the free accessible pupil space becomes a limiting factor it might be necessary to mount the prisms at another position in the excitation beam path. In this case it might be mandatory to use a stack of Nomarski prisms instead of the Wollaston prisms to ensure convergence of the generated beamlets in the pupil plane. A Nomarski prism consists of two silica wedges cemented together at their hypotenuses.

2. Spot multiplication in MMM

Their optical axes are perpendicular to each other, one parallel to the prism's surface and one oriented at an oblique angle with respect to the referring adjacent and opposite leg, see Fig. 2.4.

This configuration ensures the ordinary and extraordinary beamlets leaving the prism are converging due to refraction at the quartz-quartz interface. Tilting the prism with respect to the incident beam and thus changing the optical axis' obliqueness the crossover point is easily and accurately placed in the microscope's pupil plane.

The option to mount the prisms in the free accessible pupil space and the marginal deflexion angles of the created beamlets though did not enforce the utilization of high-priced Nomarski prisms in the case of the MMM-4Pi presented here.

2.3.2. Adjusting for perfectly uniform beamlets

Each Wollaston prism is cemented in an aluminium ring enclosure 2.5 allowing the prism to be mounted in the free accessible pupil space and to be rotated in the plane perpendicular to the beam propagation. Mounting one prism the prism's optical axes might for example be exactly parallel (upper part) and perpendicular (bottom part) to the incident beam's linear polarization. In this case the incident light does not possess polarization components in the plane spanned by the second wedge's optical axis and the propagation direction of the incident beam. Thus no second beam is generated: the incident beam is tilted but not splitted. Rotating the prism in the direction perpendicular to both beam propagation direction and direction of incident beam polarization shifts the Wollaston prism's optical axes. Thus the incident beam's polarization component in the plane of the second wedge's optical axis and the beam propagation grows. The incident beam is splitted in an ordinary and an extraordinary beamlet, see Fig. 2.6.

At an angle of 45° the ordinary beam's intensity equals the extraordinary one's: two perfectly uniform beamlets emerge the Wollaston prism.

The uniformity of the single beamlets is very important since the setup described is deployed in two-photon mode for the reasons mentioned above. Therefore the fluorescence signal depends quadratically on the illumination intensity and thus even little differences in different focus' excitation intensities will result in clearly visible intensity variations in the fluorescence picture.

The same holds true for the next prism mounted on top of the first one: If the prism is rotated by 45° with respect to the first prism four perfectly uniform beamlets will emerge the prism stack, see Fig. 2.4.

This can be continued literally infinitely to produce any number of beams required but of course in practice the size of the free accessible pupil space and the available laser power among others are limiting factors.

In the setup presented four prisms with the thickness of only a few mm each are used to produce up to 16 perfectly uniform beamlets. Yet - for a perfectly uniform

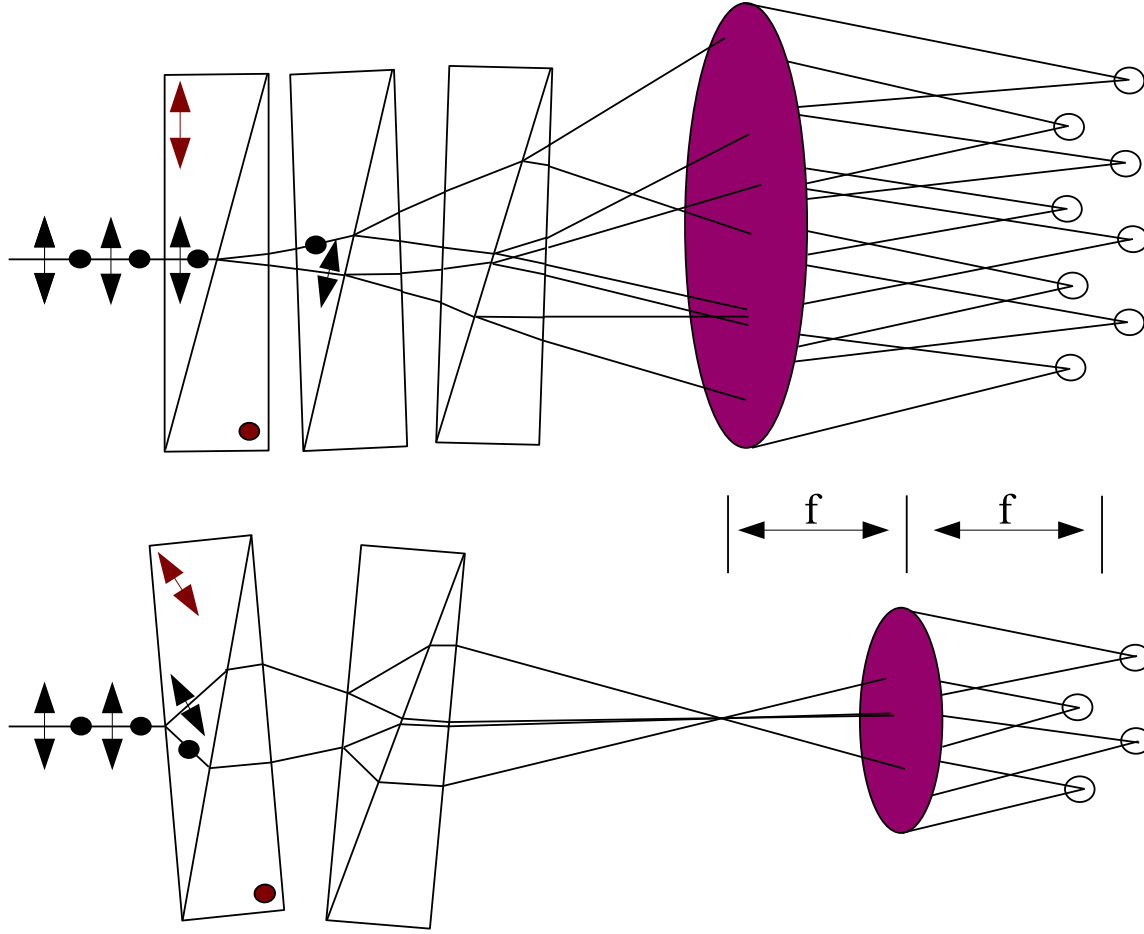


Figure 2.4.: Sketch of birefringent crystals creating multiple foci. *Bottom:* A stack of two Nomarski-prisms splits up an incident beam in up to 4 beamlets. A Nomarski prism consists of two silica wedges glued together at their hypotenuses, the optical axis (red) of one of them (left one) being oblique with respect to its adjacent and opposite leg, the optical axis of the other wedge pointing out of the image plane. Refraction at the quartz-quartz interface of the wedges ensures the splitted beamlets converge. Changing the degree of obliqueness of the left wedge's optical axis changes the point of convergence of the two beamlets. *Top:* A stack of three Wollaston prisms creates up to 8 beamlets out of a single initial one. A Wollaston prism consists of two silica wedges glued together at their hypotenuses, the optical axis (red) of the left one is parallel to the prisms surface, the optical axis of the bottom wedge is pointing out of the image plane. Wollaston prisms split up the initial beam, the resulting beamlets do not converge. For small deflexion angles and small distance to the system's aperture this non-convergence does not pose a problem.

2. Spot multiplication in MMM

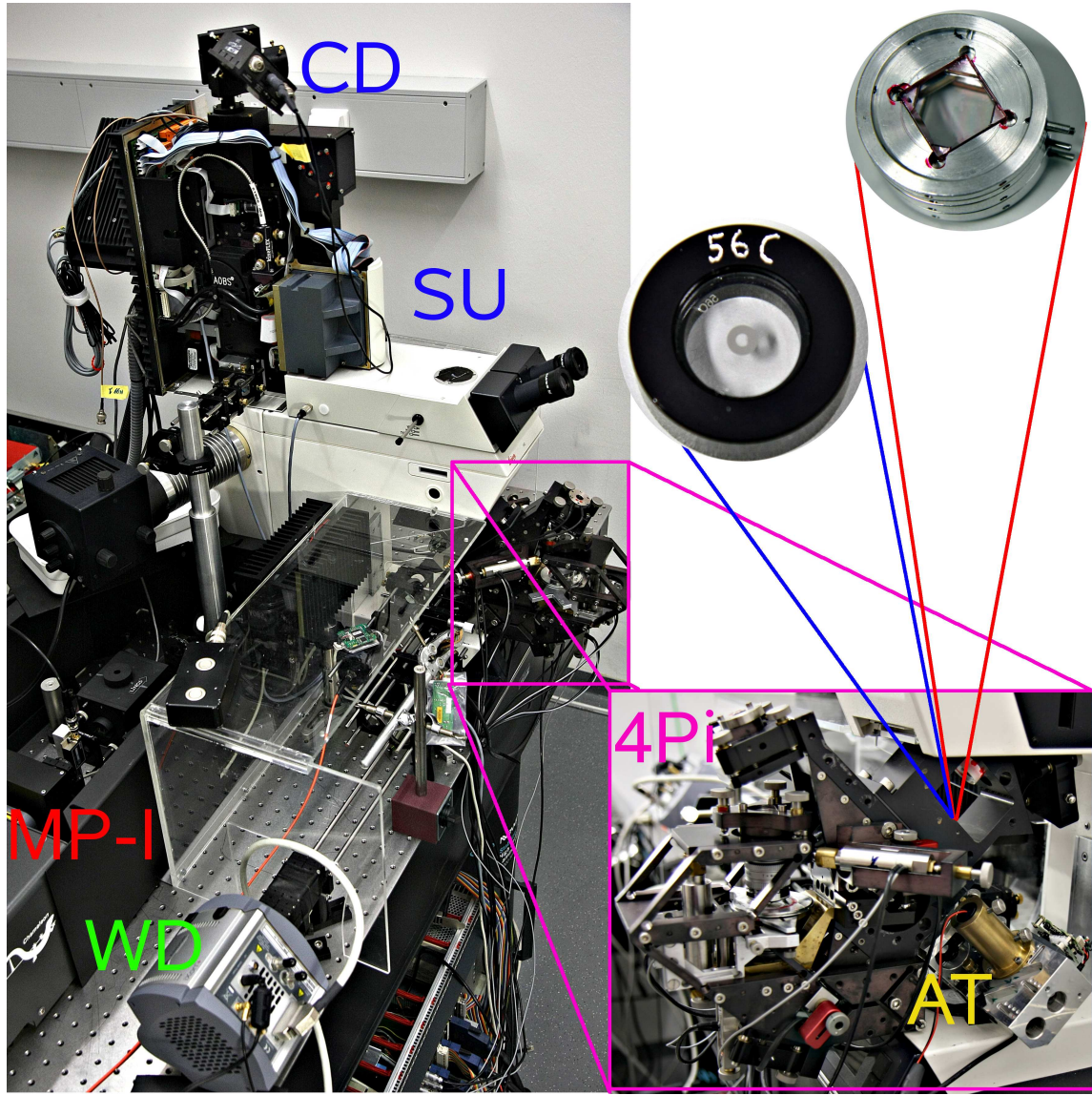


Figure 2.5.: Photography of the experimental setup. The prisms (red zoom-in) or the dark ring filters (blue zoom-in) are mounted in the free accessible pupil space of the 4Pi head (pink zoom-in). The letters refer to the conceptual subunits as shown in Fig. 2.3.

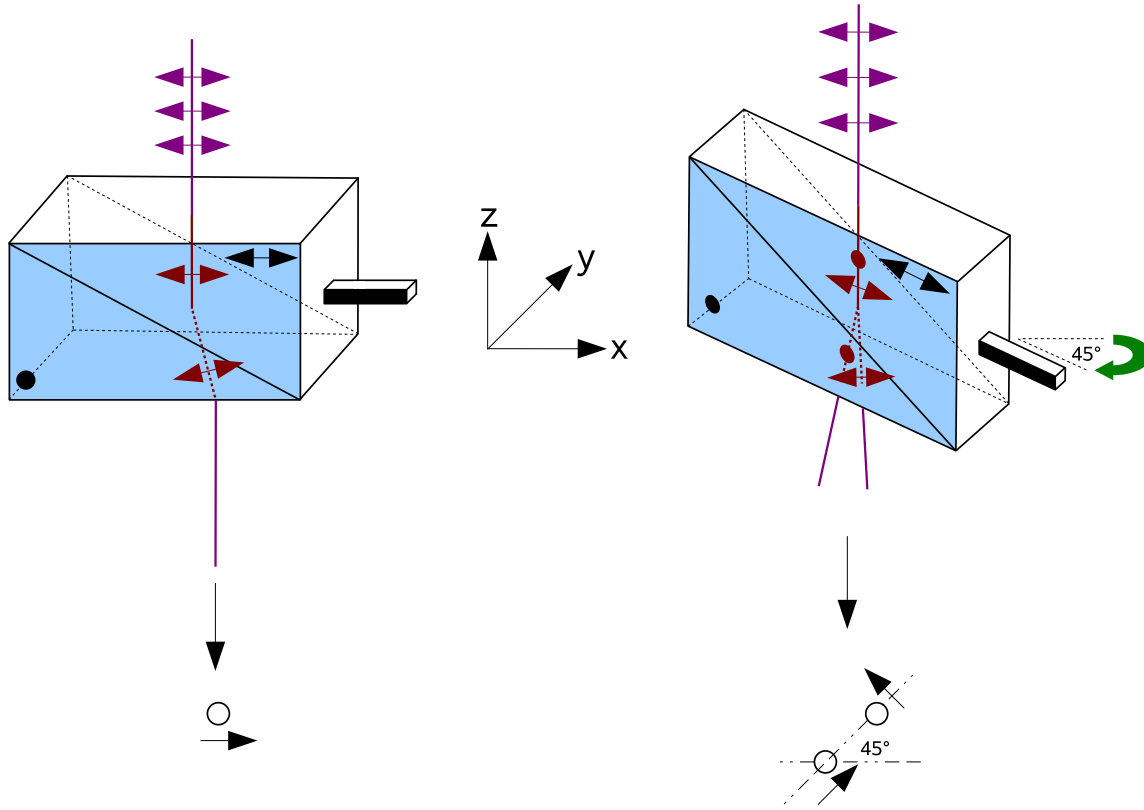


Figure 2.6.: Spot multiplication in a Wollaston prim. An incident light beam, linearly polarized in the x -direction and propagating along z , enters a Wollaston prism. The optical axis of the prism's upper wedge is also oriented in the x -direction, the one of the bottom wedge along y . The incident light does not possess polarization components in the yz -plane, thus it is not splitted entering the second wedge. Rotating the prism by 45° along y changes the optical axes' position with respect to the polarization direction of the incident light in that way that the polarization components perpendicular to the second wedge's optical axis and that in the plane of the optical axis and the beam propagation equal each other: two equally bright beamlets are created, relocated by 45° with respect to each other.

2. Spot multiplication in MMM

incident intensity profile perfect uniformity of the single beamlets' intensities is - in principle - possible. In contrast to microlenses the quartz prisms are produced with standard methods at a high optical quality.

The optical quality of this MMM system therefore is limited only by the optical quality of the incident laser beam profile and that of the 4Pi objectives in contrast to a lens-array system's optical quality which is further deteriorated by lenses-induced wavefront aberrations. The transmission of the prism stack - over 98% for each Wollaston prism - is significantly higher than that of the lens-array and is further enhanced immersing the single prisms of the stack in standard microscopy immersion-oil to minimize reflexion losses. The high transmission poses an additional advantage of this new method of spot multiplication.

2.4. Experimental results

In the following section the power of the new MMM 4Pi setup is clearly demonstrated. Therefore fusion and fission events in living yeast as well as slight movement of promyelocytic leukemia nuclear bodies were recorded.

2.4.1. Monitoring life processes in the mitochondrial network of *Saccharomyces cerevisiae*

Mitochondria are rod-shaped organelles of eukaryotic cells. Predominantly they function as the cell's powerplants converting fatty acids (stemming from fat) and Pyruvate (coming from glucose and other sugars) into the kind of energy needed by the cell to maintain its metabolism, the universal energy carrier adenosine triphosphate (ATP).

Regarding their essential role it is not astonishing that anomalies in structure and function of mitochondria are key factors for several diseases, among others [21], [104], [81] diabetes mellitus [103], [107].

The mitochondrial tubules' outer diameter is ≈ 300 nm and Mitochondria are therefore an object of special interest for 4Pi microscopy allowing for deeper insights compared to conventional confocal microscopy owing to its superior axial resolution. The smooth outer membrane of the individual tubules of the organelle is internally connected via certain contact sites both to the many times folded inner membrane forming an inner boundary membrane and to the so-called cristae [1] separating the interior of the tubules in several reaction rooms.

In yeast, mitochondria are organized in a dynamic contiguous branched network [1]. For this thesis fusion and fission events of this network have been monitored by the MMM-4Pi setup presented. Therefore yeasts of a culture of *S. cerevisiae* stably expressing mitochondrial matrix-targeted eGFP and prepared as described in detail in [71] were kindly provided by Stefan Jakobs of the MPIBPC in Göttingen. The yeasts were embedded in a mixture of 3% mowiol dissolved in yeast culture medium and

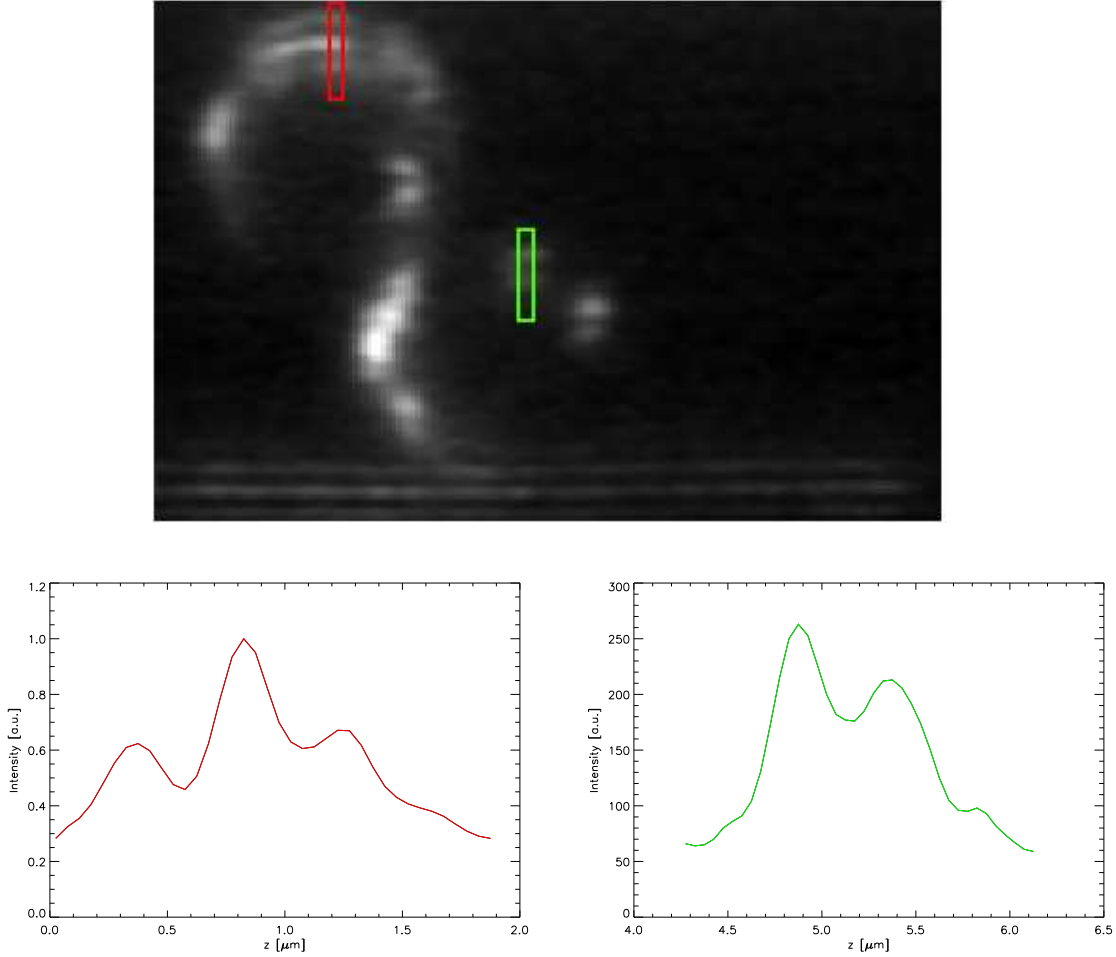


Figure 2.7.: *Top*: xz -slice of yeast before sidelobe removal. The image was obtained by successively xy -scanning the sample along z . The shown slice was smoothed $3\times$ in every direction and 5% of the image's intensity were subtracted in order to remove the background noise. The yeast shows on top the typical 4Pi Type C wide-field structure of constructively interfering excitation and detection light: a dominant main maximum and less pronounced first order sidelobes. In the middle of the image the phase has shifted considerably. *Bottom*: z -profiles of the regions of interest marked in the left xz -slice. Obviously the excitation light changes from constructive to destructive interference. The profiles exhibit a decreased modulation depth mirroring the fact that mitochondria are bulky extended objects and their diameters exceed the 4Pi's axial resolution by a factor of 2.

2. Spot multiplication in MMM

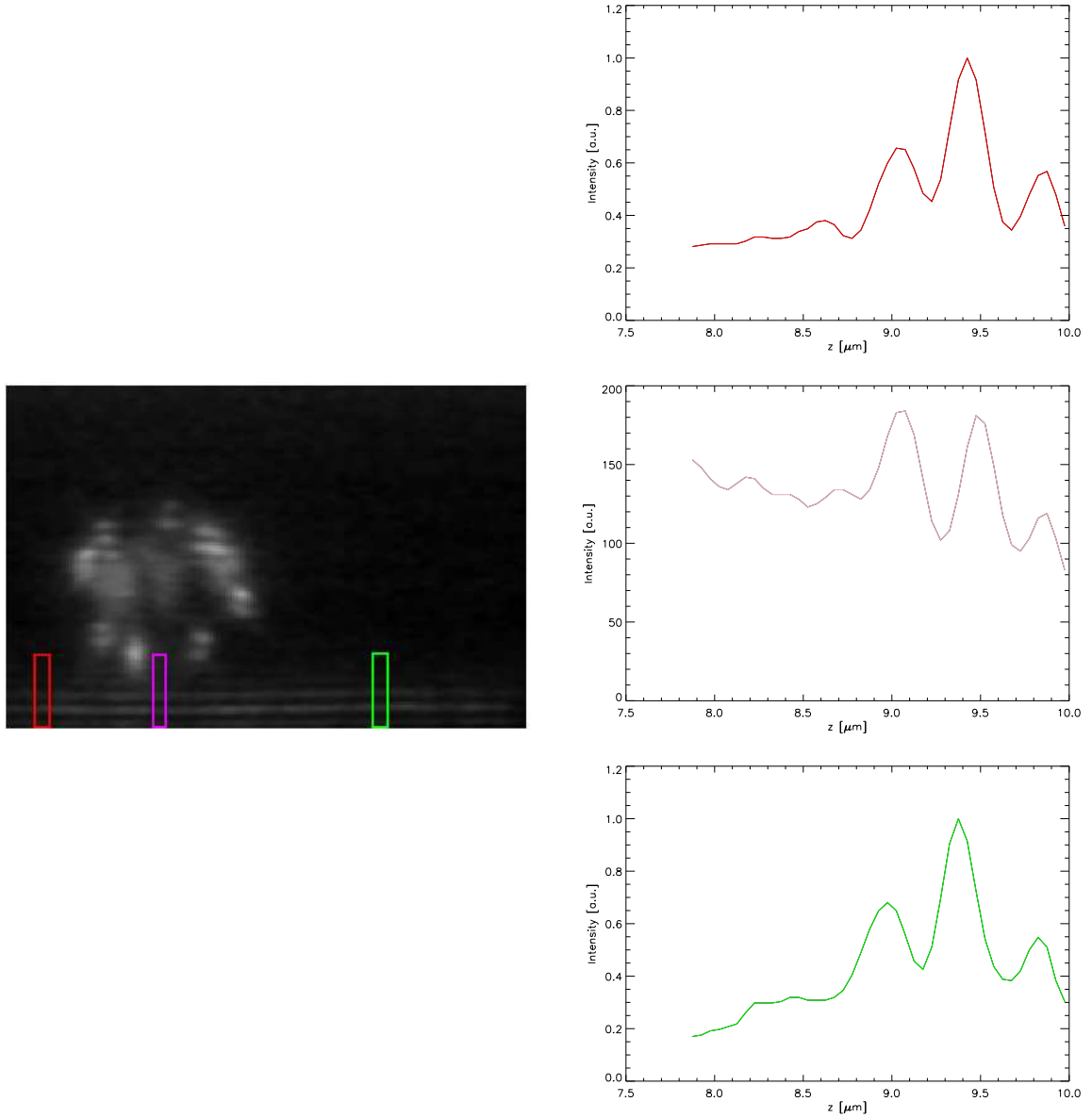


Figure 2.8.: xz -slice (*left*) of a yeast on top of a dense layer of fluorescent beads. The z -profiles (*right*) of the regions of interest as marked in the left image exhibit constant phase throughout the image apart from the region beneath the yeast. The phase of the wavefront is obviously shifted upon passing the dense biological tissue. A proper deconvolution has to compensate for such a phase shift.

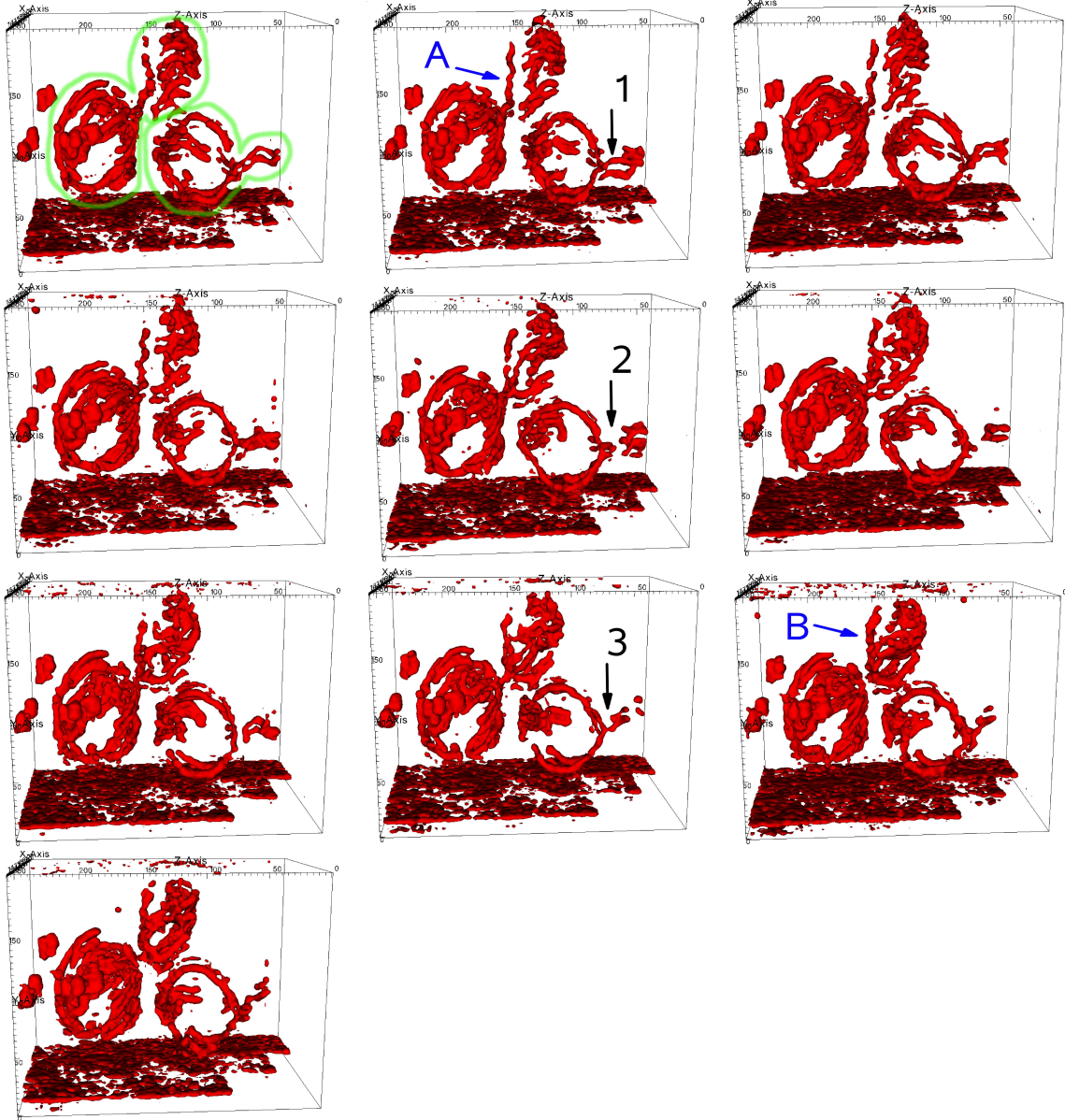


Figure 2.9.: Time-series of living yeast. The single 3D data stacks were recorded *xy*-scanning the sample along *z*, the recording of one stack took 42 seconds and the stacks were recorded successively (line by line from left to right) without interruption. Shown are two yeast cells, one of them still involved in budding as indicated green in the first stack. It is clearly seen that mother and daughter still share parts of the mitochondrial network, indicated by a blue arrow. While arrow A indicates a single rod-like mitochondrion still belonging to the mother, the very same mitochondrion has been clearly incorporated by the daughter some minutes later, indicated by arrow B. The single cell exhibits successively fusion and fission processes at its boundaries as indicated by the arrows 1, 2 and 3.

2. Spot multiplication in MMM

mounted between two coverslips. The mowiol was added to stiffen the yeast culture medium in order to slow down spatial movements of the yeasts. Adding successively more and more mowiol will result in avoiding spatial movement at all although to the price of a significantly raised refractive index (up to 1.4) while the raise in refractive index is still moderate (1.33 without to 1.35 with mowiol) for a 3% contribution of mowiol and indeed even improves image quality by ameliorating spherical aberrations due to refractive index mismatch of water - based embedding yeast-culture medium and biological tissue. Once mounted, the mitochondria throughout a sample exhibited activity for at least 5 – 7 days without obvious changes in structure or integrity of the network, irrespective of the quantity of recordings. The addition of little amounts of mowiol thus did not result in signs of cellular distress.

In Fig. 2.7 a typical raw data xz -image is seen obtained by repeated xy -scanning of the sample which is moved along z . The excitation wavelength was set to 880 nm. The mitochondrion at the top of the image displays the typical 4Pi Type C wide-field structure of a sharp main maximum and less pronounced sidelobes of around 40%. The elevated minima or in general decreased modulation depth of the intensity interference pattern displayed in the right images of Fig. 2.7 reflect the fact that mitochondria are extended rod-like structures exhibiting diameters exceeding the system's axial resolution limit of ≈ 120 nm by a factor of ≈ 2 .

In the MMM 4Pi presented in the course of this thesis no active phase compensation [16] was used to account for residual refractive index mismatches between immersion medium and yeast as well as immersion and embedding medium. A linear phase shift proportional to the penetration depth into the tissue is clearly seen throughout the image and has to be accounted for afterwards by algorithmic post-processing of the acquired data (see appendix, section C). This works reliable though and ambiguities in image interpretation due to phase artifacts can therefore be ruled out. Reliable removal of the sidelobes is seen best regarding the layer of fluorescent beads which was attached directly to the bottom coverslip before mounting the yeasts, see Fig. 2.8. In adequate distance to the mitochondria, the raw data of the fluorescent layer exhibits almost constructive interference for both excitation and emission throughout the image. Just beneath the aberration inducing sample the interference pattern changes to destructive excitation and constructive emission interference or vice versa. Nevertheless deconvolution yields an even unruptured line of fluorescence as seen in Figs. 2.9 and 2.10.

Thus the final resolution is about $200\text{ nm} \times 120\text{ nm}$ in xy and xz respectively. This is not sufficient to have a look on single cristae yet it allows to measure the diameters of single rods with high precision. These appear to have a mean diameter of roughly 350 nm.

The acquisition of a single xy frame of $28\text{ }\mu\text{m} \times 36\text{ }\mu\text{m}$ took 113 milliseconds resulting in an overall imaging time including read-out of the camera and laser-flyback of 42 s for a stack of 350 frames covering an axial distance of $14\text{ }\mu\text{m}$ in steps of 40 nm. The corresponding single beam setup takes for imaging the same region 1.5 seconds per

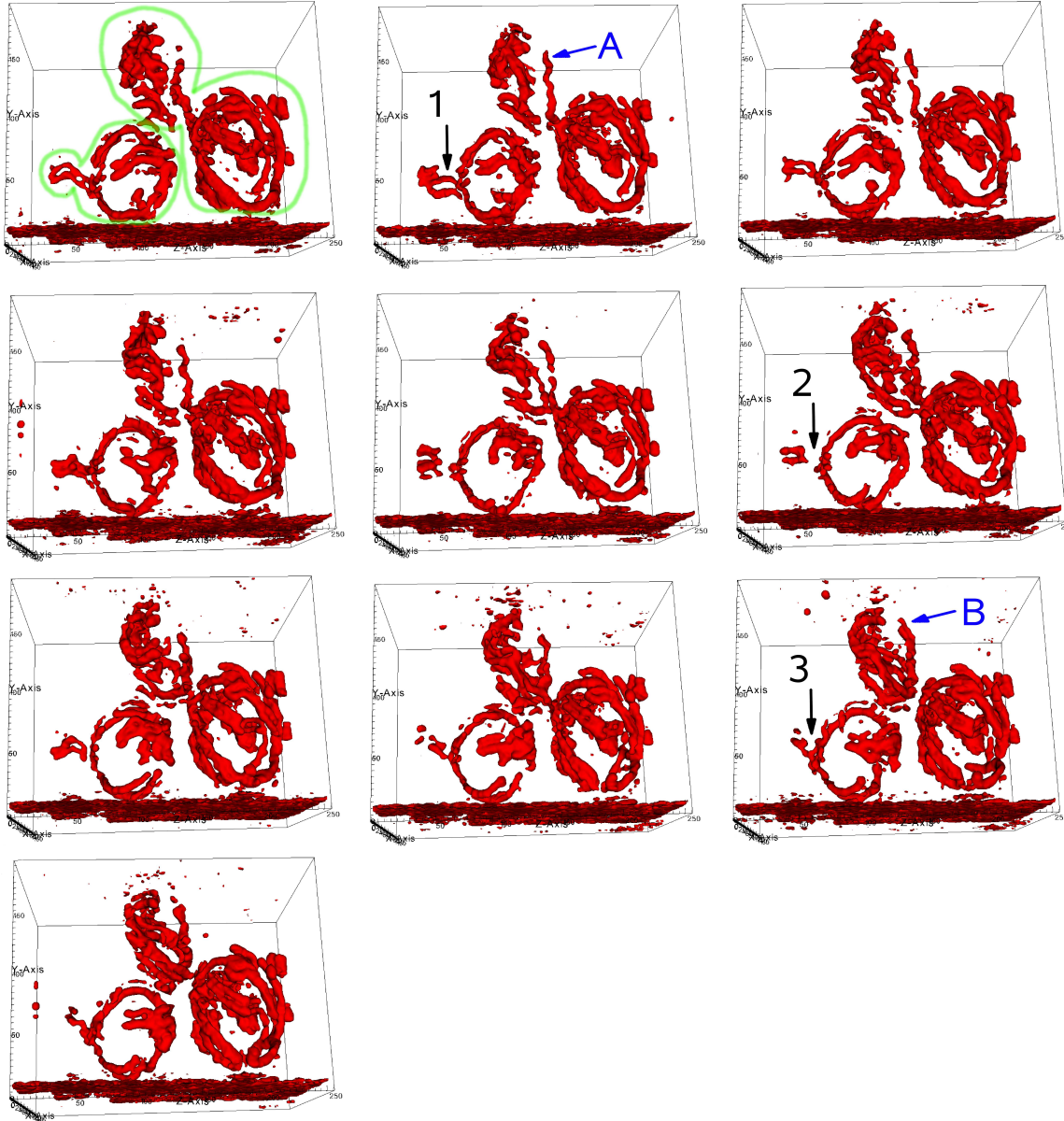


Figure 2.10.: Time-series of the same living yeast from another point of view. New details of the cells' movement can be observed. In general the mitochondrial network changes its shape rapidly. Note: The layer of fluorescent beads is contiguous and artifact-free after simple axial sidelobe removal.

2. Spot multiplication in MMM

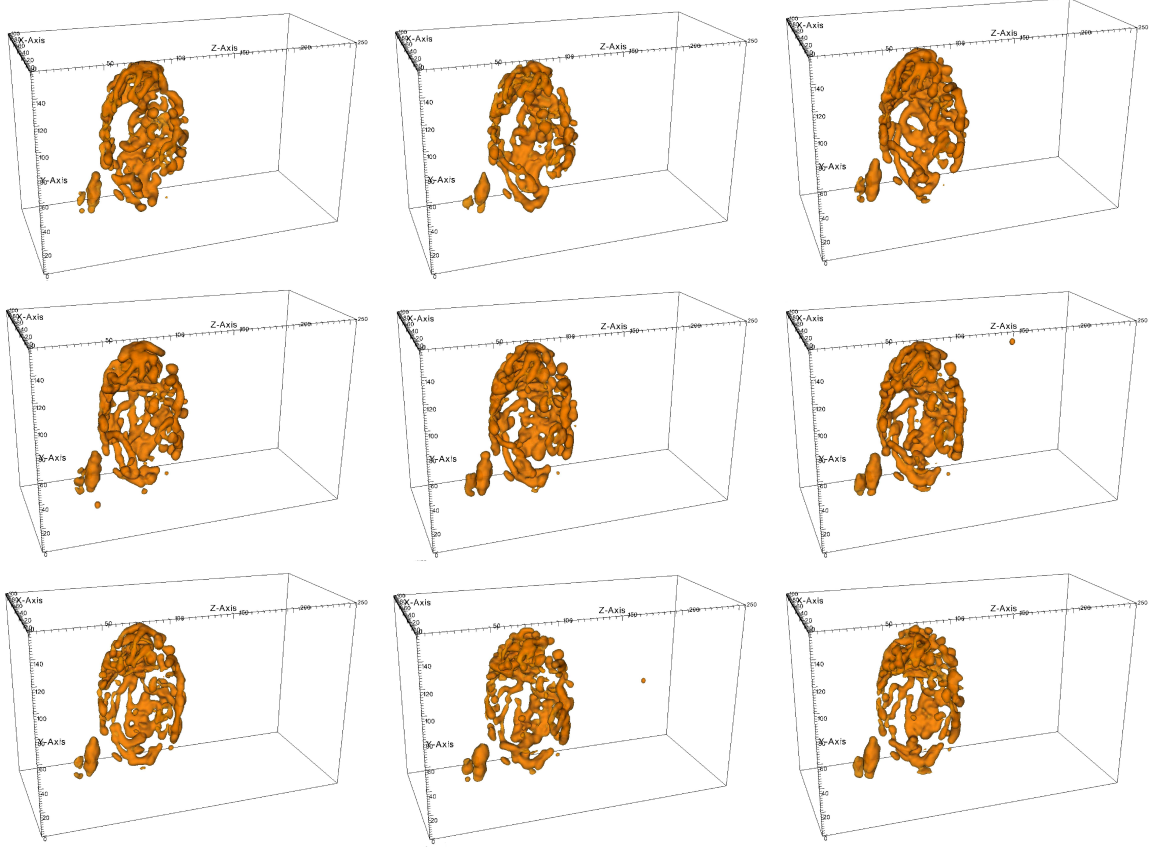


Figure 2.11.: Time-series of a second living yeast. The single 3D data stacks were recorded xy -scanning the sample along z , the recording of one stack took 37 seconds and the stacks were recorded successively (line by line from left to right) without interruption. Shown is a single yeast exhibiting a dense mitochondrial network. The single mitochondria are nevertheless resolved with high precision. The yeast exhibits rapid structural changes of its mitochondrial network.

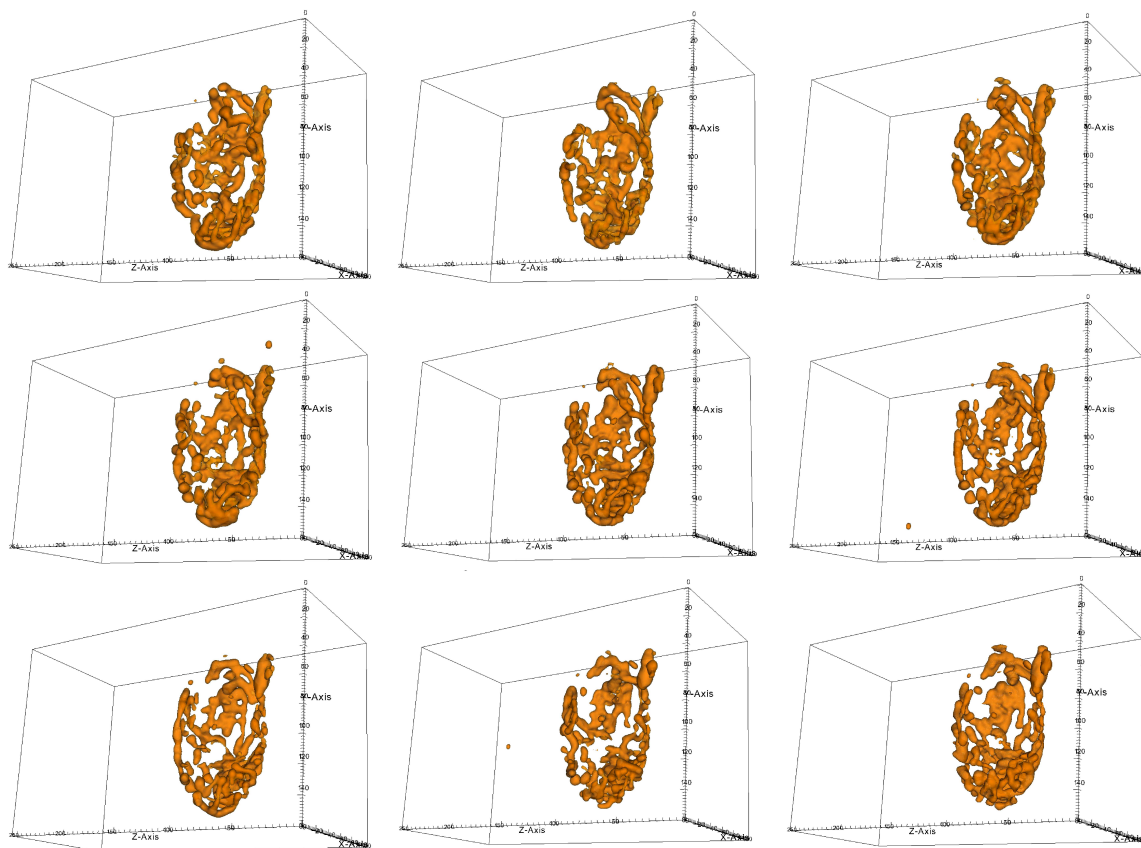


Figure 2.12.: Time-series of the second living yeast seen from another perspective. New details in the rapid change of the mitochondrial network can be observed.

frame or 9.3 minutes per stack. Thus the MMM 4Pi exhibits a 13-fold increase in imaging speed compared to its corresponding single-beam setup.

10 stacks of each yeast were recorded successively without interruption. Two time series of living yeasts are displayed from different points of view in Figs. 2.12, 2.10, 2.11 and 2.9.

Bleaching obviously did not play a role. This was expected since the time - averaged power per beamlet never exceeded 10 mW during recording time.

The images in Figs. 2.9 to 2.12 were smoothed $3\times$ along all directions before the axial sidelobes were removed utilizing the algorithm described in detail in appendix, section C. 15% of background noise was removed before the images were 3D rendered with the free license software VisIt. All stacks were regarded for using the same set of parameters for sidelobe removal as well as for 3D rendering.

Figs. 2.9 and 2.10 show different views on two living yeasts, one of them still attached to its daughter. Mother and daughter are still connected, this can be seen clearly as they still exchange parts of their mitochondrial network. Most obviously

one rod-like mitochondrion, marked by an arrow (A, B) in Figs. 2.9 and 2.10, in the first frame still attached to the mother yeast and pointing prominently upwards, is incorporated by the daughter as time propagates. The single yeast (the right one in Fig. 2.9) displays vivid fusion and fission processes on its right boundary, indicated by arrows (1, 2 and 3). The extension to the right, clearly connected to the rest of the network in the first stack, undergoes fission (stacks 5–7) before fusing again with the yeast’s residual mitochondria.

Figs. 2.11 and 2.12 show another living yeast from different points of view displaying an exceptionally dense network of mitochondria. The network’s structure alters rapidly. Nevertheless single mitochondria and details of the yeast’s structural changes are perceived undoubtedly and with high precision from the images.

2.4.2. Recording moving PML-NBs in the human osteosarcoma cell line U2OS

Promyelocytic leukemia nuclear bodies (PML-NBs) are mobile macromolecular nuclear structures. These organelles are thought to be involved in the regulation of a diversity of cellular functions, among others DNA replication and repair, transcription, apoptosis and tumor suppression [72], [5]. A certain class of PML-NBs forming specific complexes with telomeres are known to be essential for the alternative lengthening of telomeres (ALT) to happen in the absence of telomerase in tumor cells like the osteosarcoma cell line U2OS [95], an alternative to telomerase for maintaining telomere lengths upon replication thus avoiding apoptosis [128].

Recent 4Pi studies on these ALT-associated PML bodies (APBs) revealed unprecedented insights in the APB’s structure, namely that PML bodies are hollow spheres [85] with mean diameters reaching from 200 nm (minimum diameter for resolving unambiguously the hollow interior) to several μm rather than bulky aggregates of proteins. A model proposed to explain this fact [85] is based on the assumption that the APBs are formed around telomeric ends like (spherical) caps. Though such a formation has not yet been unambiguously recorded so far.

Confocal microscopy with its greater throughput abilities compared to 4Pi microscopy is well suited for mobility studies on the PML-NBs [48], [72] but the confocal resolution is not sufficient to image the PML-NBs’ hollow-sphere structure and thus at maximum a colocalization of stained telomeres and aggregates of additionally stained proteins known to be involved in the PML-NB formation can be seen in dual color experiments.

4Pi on the other hand is a suitable vehicle for resolving the nature of telomere-PML-NB aggregates. Yet these recent studies have been performed using TDE [119] embedded fixed samples and oil immersion objectives of the for the time being highest available NA of 1.46. These objectives provide a superior resolution in comparison with NA 1.2 water immersion objectives (see chapter 4) yet they are not suited for

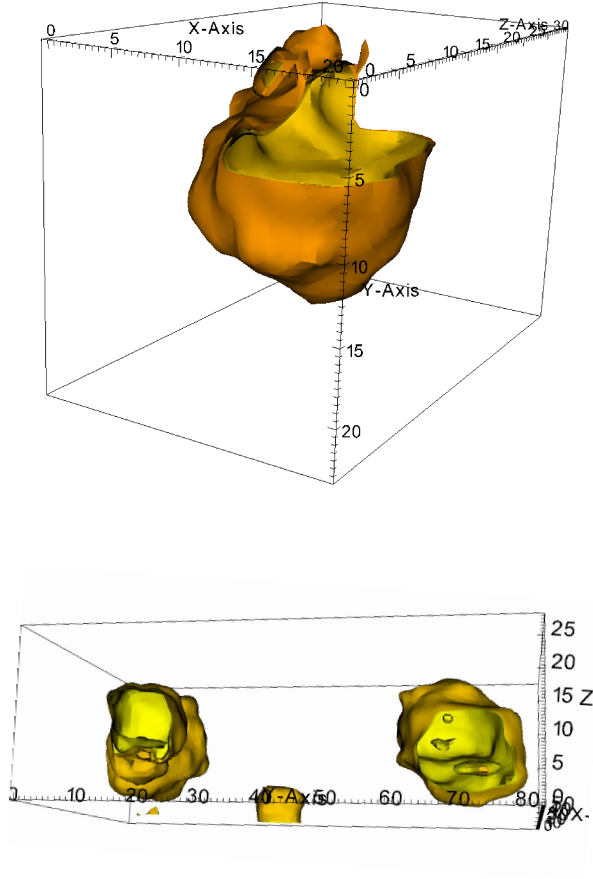


Figure 2.13.: Single Promyelocytic leukemia nuclear bodies (PML NBs). The two images show regions of interest, arbitrarily picked out of stacks 1 (*up*) and 13 (*bottom*) of Fig. 2.14, in magnification. Parts of the images are cut out revealing the PML-NB's hollow-sphere structure clearly. Although the PML-NBs were recorded alive with NA 1.2 water immersion objectives these images successfully confirm recent revelations obtained from fixed samples. Thus a first important step toward the recording of telomeric-end capping was accomplished.

2. Spot multiplication in MMM

recording processes in living specimen.

This is therefore a task for the MMM-4Pi. In preliminary studies it was ensured that the structure of hollow spheres could be resolved even with NA 1.2 water immersion objectives. Single PMLs picked out arbitrarily from stack 1 as well as stack 13 of the recorded time-series displayed in Fig. 2.14 are shown in magnification and partly sectioned in Fig. 2.13. These images demonstrate clearly the MMM-4Pi's ability to resolve the hollow-spheres – structure even for moving, living PML bodies and utilizing NA 1.2 water immersion objectives.

Samples of osteosarcoma cells U2OS containing APBs being transiently transfected with peGFP-PMLIII as described in more detail in [72] were kindly provided by Sarah Osterwald (group of Karsten Rippe, German Cancer Research Center, Heidelberg).

The cells were grown on thin ($\approx 145\text{ }\mu\text{m}$) glass coverslips and have been recorded $\approx 18\text{h}$ after transfection. The observation was conducted using an adequately matched pair of one convenient (excitation/detection through the coverslip) and one dipping NA 1.2 water immersion objective allowing the sample to be embedded in a sufficient reservoir of nutrient culture medium. Additionally the system was upgraded by a home-built environmental chamber maintaining a temperature of 37° but without means of supplying the sample with CO_2 . Therefore the cells were buffered with 10 mM Hepes solution and even after 3h of recording the cells did not show structural changes or other signs of cellular distress apart from increased PML-NB movement. The dependency of the mobility of nuclear particles on the observation period though reportedly is an effect triggered by the multi-scale organization of chromatin [49] rather than of cellular distress.

Fig. 2.14 shows a series of 20 3D data stacks of a PML-NB containing nuclear region. The stacks were recorded xy -scanning the sample along z . Each series consists of 73 xy -scanned frames of $28\text{ }\mu\text{m} \times 36\text{ }\mu\text{m}$ in steps of $\Delta z = 80\text{ nm}$ thus covering a total axial distance of $5.8\text{ }\mu\text{m}$. Each stack was recorded in less than 10 seconds and a stack was imaged every 30 seconds. The images in Figs. 2.13 and 2.14 were smoothed $3\times$ along all directions before the axial sidelobes were removed utilizing the algorithm described in detail in chapter 4. 20% of background noise was removed before the images were 3D rendered with the free license software VisIt.

The formation of PML bodies could not yet be observed. A fraction of the PML-NBs though can be viewed moving slightly in Fig. 2.14. Observing the image's far left boundary for example a single PML NB, marked by an arrow, moves successively in and almost out of the field of view. Also the position of single PMLs with respect to each other changes slightly as time progresses as it is seen for a group of three PML-NBs positioned in the middle of the 3D stacks (circled in Fig. 2.14).

The real success yet must be seen in the ability to resolve the PMLs' hollow sphere-structure even in the case of living specimen and recording with water immersion objectives. This is shown convincingly in Fig. 2.13.

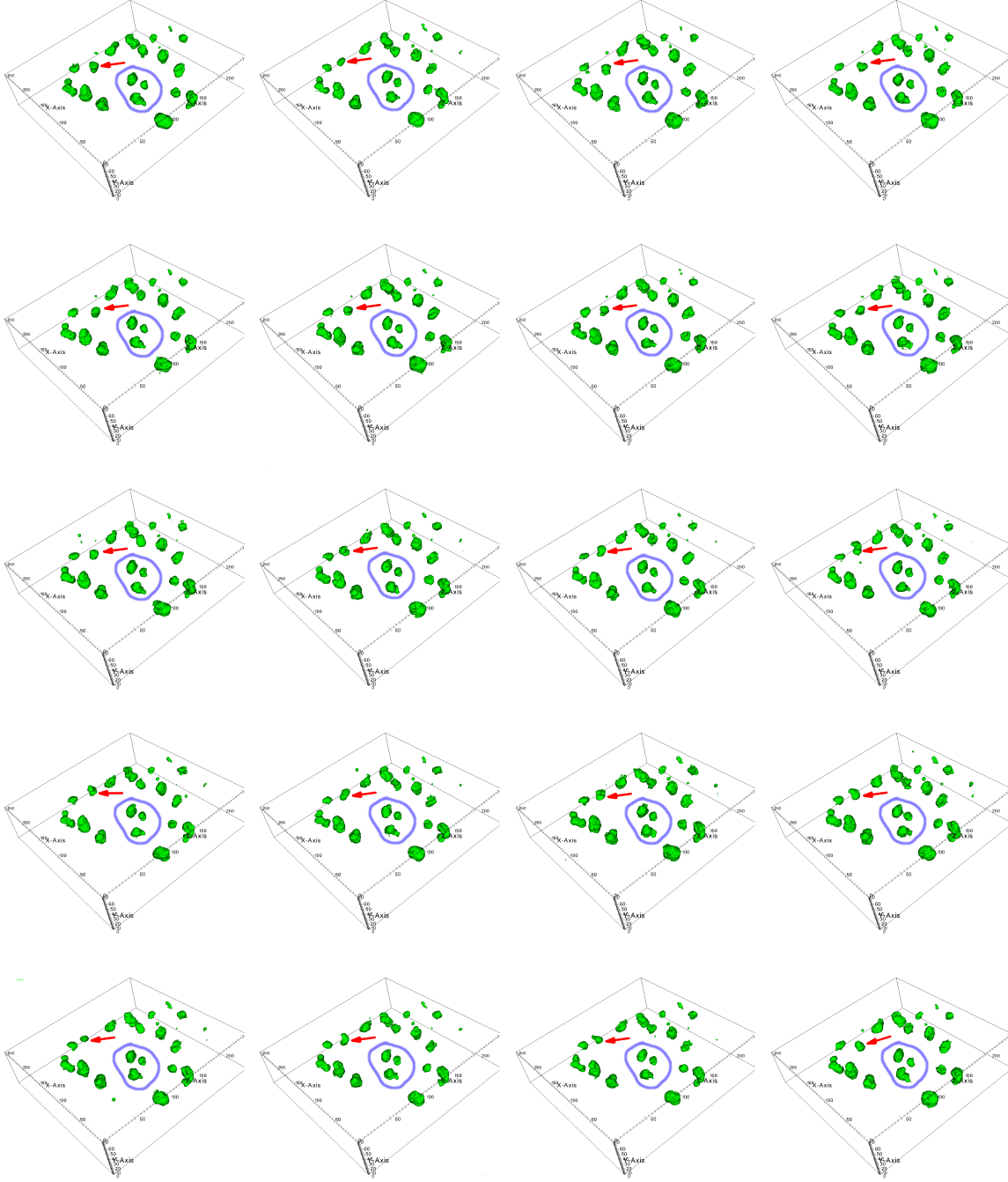


Figure 2.14.: Time-series of PML NBs. The 3D stacks of a nuclear region containing PML NBs were recorded xy -scanning the sample along z , the recording time for one stack was 9 seconds. A stack was recorded every 30 seconds (line by line from left to right). Slight movements of a fraction of PML NBs can be observed, for example at the marked positions.

2.4.3. Pushing the limits of MMM-4Pi

2.4.4. Summary

The MMM-4Pi presented in the last chapter utilizing 4 Wollaston prisms to generate 16 parallel foci has proven its ability to image complex 3-dimensional structures within living samples with high spatial as well as temporal resolution. Partly dense mitochondrial networks of the living yeast *S. cerevisiae* were observed in less than a minute per 3D stack, which is a 13-fold increase in imaging speed compared to the corresponding single-beam setup. The system's axial resolution was about 120 nm throughout the imaged stack, displaying the 4Pi's axial superresolution even in a widefield detection scheme. The recording of a nuclear region containing PML-NBs was even conducted in less than 10 seconds per 3D data stack. Slight movements of the PML-NBs could thus be observed and the high axial resolution of the 4Pi optics allowed to resolve the hollow-sphere structure of single PML bodies, which can not be resolved by conventional confocal microscopy.

The stacking of birefringent crystals, in this case Wollaston prisms, mounted in a conjugated pupil of the microscope, was proposed and for the first time successfully implemented as a conceptually new way of multiple foci generation in multiphoton multifocal microscopy (MMM). Employing birefringent crystals had several advantages:

- First the crystals are cheap and easy to implement.
- The crystals are fabricated with standard methods at a high optical quality and thus the optical quality of the generated beamlets only depends on the optical quality of the incident laser beam profile and the micro-objectives used for imaging.
- The crystals are easy to adjust for perfectly uniform beamlets and each Wollaston prism displays a transmission of over 98%.
- Stacking as many of the Wollaston prisms as needed provides any number of beamlets required.

The stacking of birefringent crystals thus allows for cheap, reliable, convenient and infinite generation of multiple beamlets of high optical quality and is therefore sure to be implemented in future MMM setups.

2.4.5. Further enhancements

The MMM-4Pi has proven its versatility and reliability for fast 3D live cell imaging. But there is still room for improvement.

The design of the MMM 4Pi setup relies on multiphoton excitation. Besides the manifold advantages of multiphoton excitation compared to single-photon excitation, such as the decreased bleaching, less scattering or decreased sensitivity for other specimen-induced aberrations due to the fluorescence’s quadratic dependence on the excitation intensity, the most prominent one was the inherent axial sectioning ability. This facilitated efficient widefield detection without the need for a confocal pinhole (array). Without the confocal pinhole though, this mode of excitation becomes mandatory for superresolved 3-dimensional images.

On the other hand multiphoton excitation is almost exclusively done with high-priced mode-locked pico- or femtosecond lasers providing for the necessary high pulse intensities. It is not to be expected that more than one of these lasers is enrolled in a live-cell setup. Aiming for dual - color multiphoton images - a standard in imaging biological samples and necessary for example for recording unambiguously PML-NB forming proteins (first color) capping a telomere (second color) - it is a practical problem to find two dyes exhibiting adequate properties: These dyes have to feature both sufficient multiphoton cross sections for reliable signal generation and overlapping excitation spectra as well as - at the same time - emission spectra far enough apart from each other to be spectrally selectable by means of band pass filters.

The choice of dyes displaying these properties is to date quite limited. Indeed for selectively labeling certain proteins or organelles in living samples most biologists would prefer the technique of expressing fluorescent proteins within these structures. Despite the colored variety of fluorescent proteins being available these days there is to my knowledge only one combination of two fluorescent proteins reportedly fulfilling the conditions specified above [75]. Regarding this ‘choice’ in suitable fluorescent dyes, looking for alternative contrast mechanisms, which will open a broader field of possible applications, seems a worthwhile endeavor. This is addressed in the next chapter examining in detail the coherent label-free contrast mechanism of second harmonics generation for its applicability in 4Pi microscopy.

Furthermore, the necessity to embed and image living samples in water-based media or buffer solutions poses a twofold obstacle towards the goal of perfect 4Pi imaging: on the one hand side water immersion objectives cannot - due to their lower NAs - provide the information (resolution) gained by high NA oil immersion objectives. Secondly the refractive index of biological tissue always mismatches that of pure water. Without the constraint of a live-supporting (water - based) environment the refractive index of the embedding and immersion media can be matched exactly with the tissue’s one [119] thus avoiding aberrations leading to increased sidelobes and axial phase variations (among many more) from the beginning. Yet there are techniques to alleviate or even erase these issues for imaging with water immersion objectives too. Such options will be addressed in more detail in chapter 4.

3. Second harmonic generation (SHG)

Among the highly effective and specific incoherent, fluorescence methods like confocal laser scanning microscopy [94], [93], STED [66], [76] and Fluorescence resonant energy transfer (FRET) [42], [116] available nowadays, multiphoton microscopy was the best choice to be implemented in the MMM 4Pi setup presented in the preceding chapter. This was due to the many advantages of multiphoton microscopy. The most prominent thereunder is its ability to confine the signal generation to the focal region since the probability of quantum events involving the simultaneous occurrence of multiple photons is highest there. The advantages of multiphoton microscopy are also inherent to another class of multiple photon processes which rely on scattering rather than absorbing the multiple photons. Processes of this class, relevant for microscopy, are second- and third harmonic generation (SHG, THG) [68], [46], [47], [99], [3], [129] as well as anti-Stokes Raman scattering (CARS) [33], [130], [98].

SHG has been shown to be an effective contrast generating mechanism in biomedical microscopy [51], [25], [26], [17], [120], [121], [109], [110] and even a SHG-based modified MMM microlens setup has already been used to image the contraction of rat cardiac myocytes [77].

In SHG microscopy excitation light from the near infrared spectral region is converted in the sample to blue light which is spectrally selected and detected. Structures known to be sources of nonlinear scattering and thus are producing strong intrinsic SHG-signals are highly ordered. The obvious advantage of using intrinsic generated signals is the possibility to gain information about the sample without the need for staining. Thus extrinsic labels do not alter the cellular structure or metabolism nor are they cause for increased phototoxicity or photodamage. The obvious disadvantage of SHG is the need for highly ordered cellular structures exhibiting SHG cross-sections which allow for sufficiently strong signal generation. Yet in biology commonly found highly ordered intracellular structural protein complexes like actomyosin as well as extracellular ones like collagen - playing an important role in muscular diseases and even cancer [18], [124], [23] - exhibit adequate SHG cross - sections. In combination with the high focal intensities of $\approx 200 \text{ GW/cm}^2$ provided by a fs-pulsed Ti:Sa laser focused by high-NA lenses, strong SHG signals are generated.

In this chapter the non-linear effect of second harmonic generation is examined theoretically as well as experimentally in detail for its applicability in high-resolution

3. Second harmonic generation (SHG)

4Pi microscopy which is a premise for the implementation in the MMM 4Pi setup in the long run.

Second harmonic generation is a nonlinear optical process. The theory of nonlinear optics describes phenomena resulting from interactions of light and optical media like gases, crystals as well as biological tissue. Its adequate mathematical description is given by the Maxwell and constitutional equations of macroscopic electrodynamics.

In classical electrodynamics, an optical medium consists of atoms with nuclei, supposed to be stationary, and electrons, assumed to be point-like objects, moving in a classical potential around the nuclei. The electrical field of the incident light exerts a force on the electrons and excites them to oscillate. Each oscillating electron is a Hertzian dipole and, acting like an antenna itself, emits light in all directions. The emitted fields are material dependent and superimpose in a specific manner thus generating new wave vectors of distinct frequencies and directions.

3.1. Nonlinear dielectric susceptibilities

The first step is to identify the individual dipole moments or - averaged over the whole medium - the polarization induced by the incident electromagnetic field. Without further knowledge of the optical medium's microscopic structure only a functional dependence $\vec{P}[\vec{E}]$ may be stated without loss of generality: the electric field \vec{E} acting locally on all locations $\vec{r}' = (x', y', z')$ throughout the medium induces a polarization \vec{P} at the coordinate $\vec{r} = (x, y, z)$. Expanding this relation in powers of the electric field results in the equation

$$\vec{P}[\vec{E}] = \vec{P}_0 + \vec{P}_1[\vec{E}] + \vec{P}_2[\vec{E}\vec{E}] + \vec{P}_3[\mathcal{O}(\vec{E}\vec{E}\vec{E})], \quad (3.1)$$

the $\frac{1}{n!}$ term being included in the respective polarization contribution already. The first expression \vec{P}_0 therein describes the medium's intrinsic polarization contribution without an external exciting electric field. The materials examined in the course of this work though do not display such a contribution. The second expression $\vec{P}_1[\vec{E}]$ is a linear functional written in full generality (non-local in space and time):

$$P_{1,i}(r, t) = \sum_j \int d^3\vec{r}' dt' \chi_{ij}(\vec{r}, \vec{r}', t, t') E_j(\vec{r}', t'), \quad (3.2)$$

χ_{ij} being a tensor of rank two. Assuming homogeneity of time and material this tensor will depend on $t - t'$ and $\vec{r} - \vec{r}'$ solely. Furthermore the coordinates \vec{r} and \vec{r}' relate to the distances of the medium's constituents, single molecules and atoms, and are therefore some thousand to ten thousand times smaller than the wavelengths of the incident (visible to near infrared) light and thus the effect of spatial non-locality can be neglected. Then equation 3.2 turns out to be the simple convolution integral

$$P_{1,i}(\vec{r}, t) = \int dt' \sum_j \chi_{ij}(t - t') E_j(\vec{r}, t')$$

or in Fourier space and for diagonal χ in isotropic media

$$\vec{P}_1(\vec{r}, \omega) = \sqrt{2\pi} \cdot \tilde{\chi}(\omega) \vec{E}(\vec{r}, \omega),$$

$\chi(\omega)$ being the so-called linear dielectric susceptibility. In complete analogy to the description of the linear polarization the quadratic expression in equation 3.1 can be formulated as:

$$P_{2,i}(\vec{r}, \omega) = 2\pi \cdot \sum_{jk} \tilde{\chi}_{ijk}(\omega, \omega', \omega'') E_j(\vec{r}, \omega') E_k(\vec{r}, \omega''). \quad (3.3)$$

The tensor of rank three χ_{ijk} is called the first order nonlinear macroscopic susceptibility. The approach for higher order terms in the expansion equation 3.1 is accordingly. It depends strongly on the system's symmetry how many of these higher order terms are to be accounted for.

For centrosymmetric materials - meaning the properties of these materials do not change under inversion of space - χ_{ijk} vanishes identically. Remembering that both the polarization and the electric field are polar vectors and will therefore change sign under inversion of space this can be seen at once:

$$\begin{aligned} -\vec{P}_{2,i}(\vec{r}) &= \vec{P}_{2,i}(-\vec{r}) \\ &= \sum_{jk} \chi_{ijk} E_j(-\vec{r}) E_k(-\vec{r}) \\ &= \sum_{jk} \chi_{ijk} (-E_j(\vec{r})) (-E_k(\vec{r})) \\ &= \vec{P}_{2,i}(\vec{r}). \end{aligned}$$

This can only hold true for $\chi_{ijk} \equiv 0$ in centrosymmetric materials. Second harmonic generation will only take place in anisotropic materials like quartz crystals or collagen [126].

Thus, a strong monochromatic wave being linearly polarized along x and propagating along z in an anisotropic material will generate at a given place inside the material an electric field oscillating with time $E_x(t) = E_0 \sin(\omega t)$ which in turn will cause according to equation 3.3 the second order polarization $P_i(t) = 2\pi \cdot \tilde{\chi}_{ijk} E_0^2 \sin^2(\omega t) = \pi \cdot \tilde{\chi}_{ijk} E_0^2 - 2\pi \cdot \tilde{\chi}_{ijk} E_0^2 \cos(2\omega t)$. This polarization is the driving force for a static electric field (first term) and another electric field of double the incident field's frequency. This coherent up-conversion process therefore is called second harmonic generation. The emitted second harmonic field has a specific phase arrangement defined by the incident electric field. The efficiency of second harmonic generation is maximal for constructive interference of all emitted waves. This so-called phase-matching condition is met for $\vec{k}_{2\omega} = \vec{k}_\omega + \vec{k}_\omega$ (in general $\vec{k}_{2\omega} = \frac{2\pi n(\omega)}{\lambda/2} \cdot \hat{k}_{2\omega} \neq \frac{2\pi n(\omega)}{\lambda} \cdot \hat{k}_\omega = \vec{k}_\omega$ for arbitrary materials).

3.2. Generalized theory: 4Pi type C illumination driven SHG

In 4Pi microscopy two opposing high-NA objective lenses tightly focus a laser beam splitted by a beam-splitter to a common focal spot where the wavefronts add up coherently. Additionally, the detection light interferes *per se* coherently at the detector since SHG is a coherent process. Thus 4Pi illumination driven SHG is 4Pi microscopy of type C. The corresponding illumination/detection field reads:

$$\vec{E}_{\text{ill/det}}^{4\text{PiC}} = \vec{E}_{\text{ill/det}}(\vec{r}) + \underline{\underline{M}} \cdot \vec{E}_{\text{ill/det}}(\underline{\underline{M}} \cdot \vec{r}).$$

Hereby, the matrix $\underline{\underline{M}}$ accounts for both the transformation of the electric field of one of the objectives to the coordinate system of the other one and the phase shift acquired by the electric field whenever reflected (at a mirror or the beamsplitter). For the 4Pi setup used for SHG imaging, see Fig. 3.4, (with an uneven number of reflections), see Fig. A.1,

$$\underline{\underline{M}} = \begin{pmatrix} 1 & 0 & 0 \\ 0 & 1 & 0 \\ 0 & 0 & -1 \end{pmatrix}.$$

The amplitude PSF $\vec{E}_{\text{ill/det}}$, that is the electric field in and in close proximity to the focus, is calculated according to the well-known equations by Richards and Wolf [108] for high numerical aperture lenses.

In contrast to fluorescence emission, second harmonic generation is a coherent process. Mathematically, this implies that the intensity distribution in the focus cannot be calculated by simply multiplying the intensity point spread functions for illumination and detection which are computed separately, like in fluorescence microscopy, but working instead with the respective amplitude PSFs. Therefore, this coherent intensity distribution will depend not only on the quantity of scatterers involved but to a high degree on their spatial distribution and the orientation of their respective optical axes.

The detectable second harmonic generated intensity distribution $I^{2\omega}(\vec{r})$ driven by a 4Pi Type C electric illumination field $\vec{E}_{\text{ill}}^{4\text{PiC}}(\vec{r})$ is calculated by projecting the polarization field $\vec{P}^{2\omega}(\vec{r})$ onto the 4Pi Type C electric detection field $\vec{E}_{\text{det}}^{4\text{PiC}}(\vec{r})$ and for scatterer concentration distributions other than point-like objects placed in the focal center the resulting field is convolved with the respective object function (to a first approximation the hyperpolarizability of the scattering molecules within an object was assumed to be on average independent of their spatial positions, so the object function simply is 1 for all coordinates within the object's boundaries). Then the intensity distribution is the squared absolute value of the resulting field:

$$I^{2\omega}(\vec{r}) = \|(\vec{P}^{2\omega}(\vec{r}) \cdot \vec{E}_{\text{det}}^{4\text{PiC}}(\vec{r})) \otimes \mathcal{O}(\vec{r})\|^2 \quad (3.4)$$

The \cdot operation herein indicates a pointwise multiplication of the respective fields. Calculating with complex electric fields to account for the fields' phase this operation yields a complex number as result and thus the convolution operation has to be done separately for the result's real and imaginary part.

The polarization field $\vec{P}^{2\omega}(\vec{r})$ was calculated according to equation 3.3 for a 4Pi illumination field propagating in z -direction and being linearly polarized in the x -direction. First simulations were done inserting the first-order hyperpolarizability matrix $\underline{\underline{\beta}}$ [28] - this is the molecular-level equivalent to the first order macroscopic susceptibility χ_{ijk} (the ensemble average of local molecular arrangements per unit volume) - for fibrillar collagen as given in [126] for Kleinman and cylindrical symmetries. This matrix is dominated by its y -component reflecting the fact that fibrillar collagen is uniaxial and in this case its optical axis (assumed to be parallel to the fibril's orientation) is aligned along y .

Note further: the following calculations were done for an ideal point-like pinhole since equation 3.4 does not account for a confocal pinhole, neither was noise considered. The results therefore are kind of 'the best case' to be expected.

3.3. Simulations of SHG Intensity PSFs

3.3.1. Ambiguity of image interpretation

The principal limit of an optical system's resolution is described by its PSF, which is the system's image of a point-like object. First simulations were therefore done for a point-like scatterer in the focus, the origin of the region the PSFs were calculated for. The results were twofold: on the one hand the sidelobes shown are promisingly low, the intensity's z profile $I_z(z) = \int dx dy I^{2\omega}(\vec{r})$ for a point scatterer, its optical axis being oriented along the x -direction, displays sidelobes not exceeding 10% of the main maximum, see Fig. 3.1 upper left for example. On the other hand the degree of the well-known signal's dependency on the incident light's polarization direction (with respect to the material's optical axis) [19] turned out to be high such that unambiguous PSF interpretation was hard or even critical:

The second harmonic intensity distributions vary strongly as the direction of the optical axis is changed or vice versa when the polarization direction of the incident light is changed for fixed positions of the optical axes. This is shown clearly in Fig. 3.1: The point spread function of a point scatterer, the optical axis y -aligned, somewhat resembles that of a single fluorescent bead placed in the origin (with remarkably low sidelobes). The point spread function for a point scatterer with a x -aligned optical axis is on the other hand completely different: the intensity distribution in the plane $z = 0$ indeed conveys the impression of four scatterers located symmetrically around the origin contributing to the image. In fact it is even possible to construct a PSF, see Fig. 3.2, originating from four scatterers being aligned symmetrically

3. Second harmonic generation (SHG)

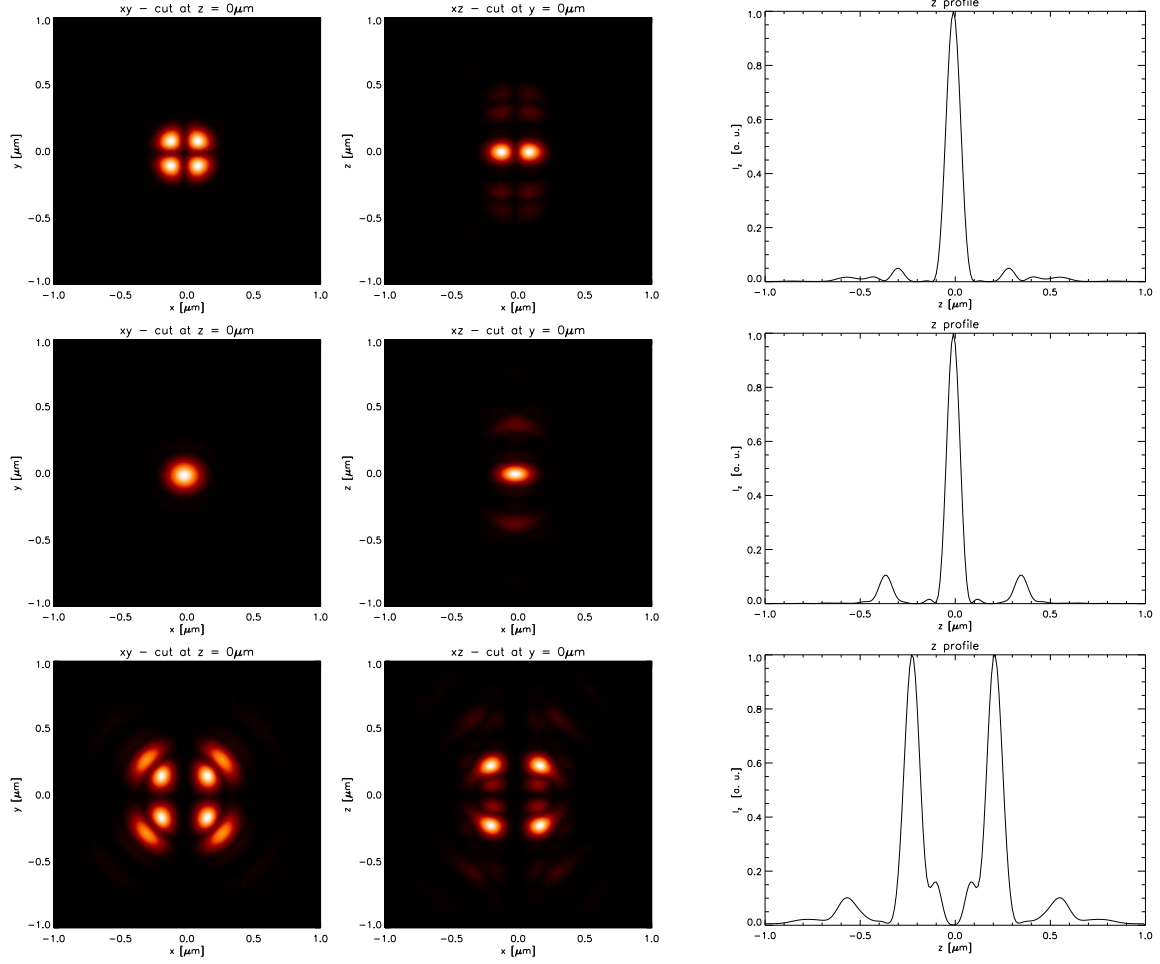


Figure 3.1.: Simulations of a single collagen point scatterer in the origin. The scatterer's optic axis is oriented along x (upper row), y (middle row) and z (bottom row) respectively. The left column shows xy -slices at $z = 0$, the middle one xz -slices at $y = 0$. In the right column the respective intensity z -profiles are displayed.

around the origin in the plane $z = 0$ with their optical axes being aligned along y , that resembles intriguingly that one of a single scatterer in the origin with its optical axis being aligned along x as seen in Fig. 3.1. Obviously the coherent point spread function is not a fixed object - specific intensity distribution but varies strongly with the object's position and especially the direction of the object's optical axis in relation to the polarization direction of the incident light.

It should be noted that the simulations hold for ideal conditions (no noise) and objects of upmost simplicity (point-like scatterers). When - even for ideal conditions - there is no obvious one-to-one correlation between an object and the object's point spread function, reliable deconvolution of second harmonic intensity distributions is not possible. This is even more true for substances of unknown properties (unknown hyperpolarizability matrix, unknown structure, etc.).

3.3.2. SHG signal decreases with the fourth to fifth power of the object's radius

SHG is a coherent process and the signal strength is basically proportional to the square of the number of scatterers per unit volume, $I^{2\omega} \propto n^2$.

Simulations done for a myosin bulk scatterer in the origin indicate essentially, the total signal depends with r^4 to r^5 on the object's radius r , see Fig. 3.3. This dependence can be understood knowing that for scattering volumes bigger than the focal volume the surfaces' SHG signal is enhanced considerably [20], at least for surfaces perpendicular to the material's optical axis. The scatterer's density on the surface is an areal density and hence a decrease of the object's radius is expected to entail a total signal decrease $\propto r^{-4}$.

In standard confocal microscopy, detecting via a single micro-objective, it is well known that the signal of an axially extended object is mainly scattered in the forward direction, that is the direction of incident light propagation [96], [92]. In contrast, the phase matching condition for backward scattering is only fulfilled for scatterers axially distributed at a spatial frequency of $2/\lambda_{2\omega}$ [126]. Thus not only the backscattered signal is strongly dependent on the imaged object's dimensions but also the total of back- and forward scattered signal, even though the oscillations are less pronounced in the latter case. Measurements that allow for the direct, quantitative determination of the object's extent are therefore not possible.

Additionally the shape of the intensity profile varies strongly with the object's dimension.

4Pi microscopy ameliorates these problems detecting the coherent superposition of both back- and forward scattered signal at the same time via two micro-objectives. However, the problems remain in principle unsolved: The oscillations depending on the object's radius are indeed less pronounced, see Fig. 3.3, but still inherent and thus quantitative measurements allowing for conclusions on the object's extent still

3. Second harmonic generation (SHG)

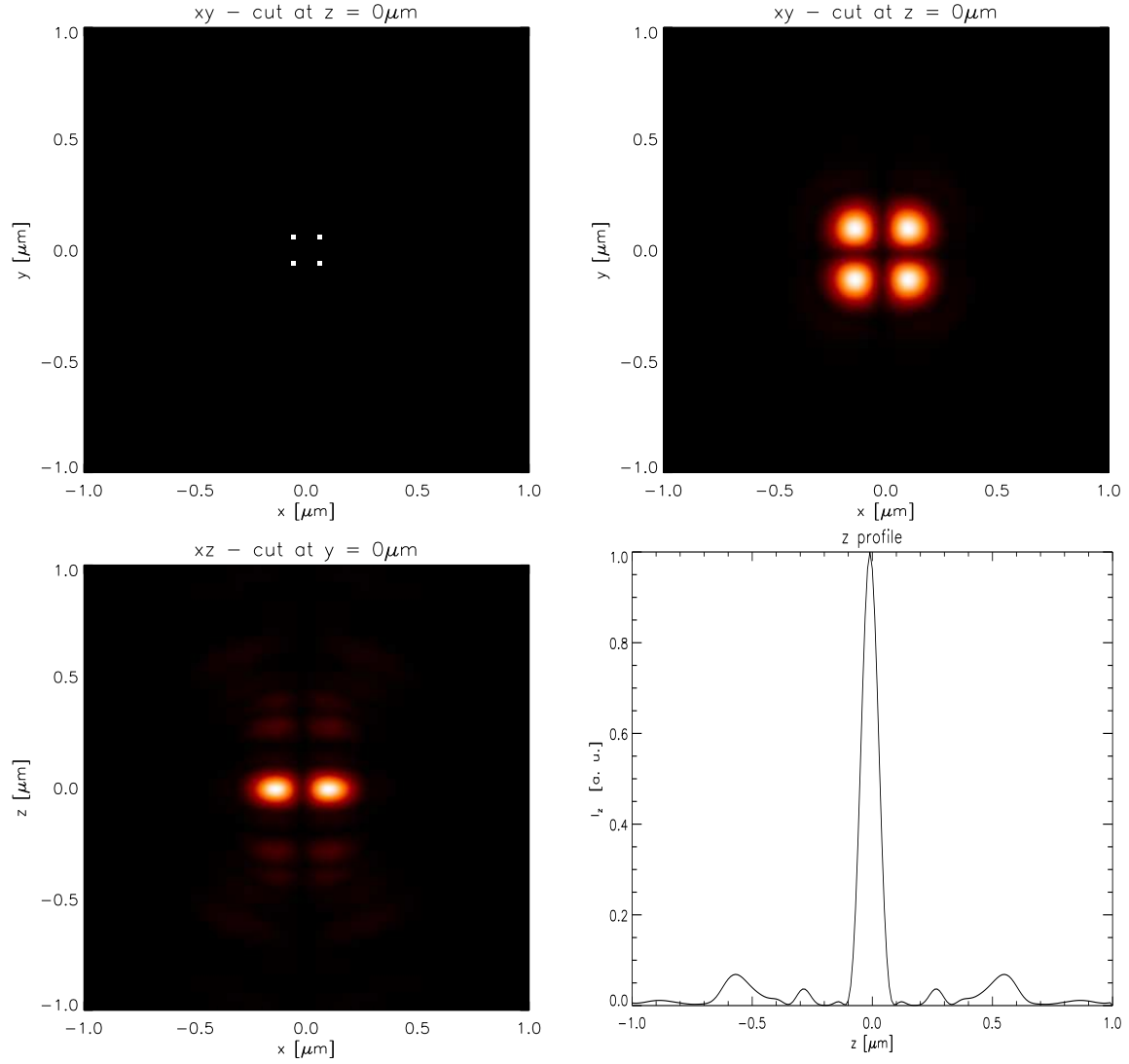


Figure 3.2.: Simulation of four collagen point scatterers. The scatterers' optical axes are aligned along y and the scatterers are positioned symmetrically around the origin in the xy -plane at $z = 0$ (*upper left*). Shown are furthermore a xy -slice at $z = 0$ (*upper right*) and a xz -slice at $y = 0$ (*bottom left*) of the signal's intensity distribution as well as the respective intensity z -profile (*bottom right*).

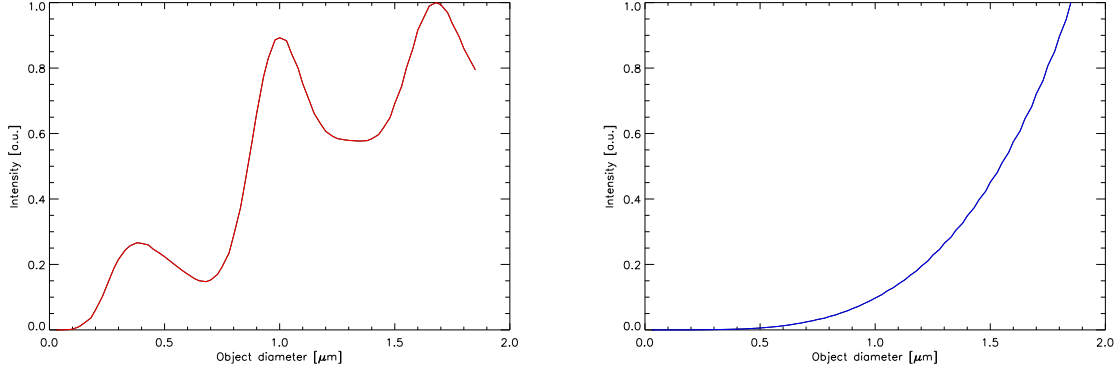


Figure 3.3.: Linear plots of total SHG signal intensity (*right*) versus scatterer's size and SHG signal detected in the scatterer's center versus object's size (*left*) for an arbitrarily small pinhole size. The total SHG signal intensity emitted depends on the scatterer's size with the 4th to 5th power. The SHG intensity detected in the scatterer's center still oscillates with the object's size.

are not reliable.

It is not until confocalization is abandoned at all and the total signal is summed up that the signal becomes completely independent on the object's extent. Thus 4Pi non-confocally detected SHG intensity distributions yield for the first time signal intensities directly relying on the object's dimension. Intensity distributions resulting from integration of the total non-confocally detected signal though do not provide for high resolution any longer. The same resolution is yielded by simply detecting the forward and backwards scattered signal each with a non-descanned detection unit in a conventional confocal setup. The coherent superposition of the emitted light due to the 4Pi's interferometric arms does not pose an additional advantage. Only the 8-fold increased signal due to the interference of the excitation light in the focal spot suggests 4Pi driven second harmonic generation to yield some advantage over its confocal counterpart.

Thin samples are needed for standardization as well as for high resolution in general. In fluorescence microscopy such a standard sample is for example an ultrathin fluorescent layer. The results elaborated above suggest the search for a coherent standard sample, in size smaller than or equal to the system's resolution limit and thus $\approx \lambda_{2\omega}/4$, to be not successful though: such a small specimen will emit only a faint signal due to the signal's r^4 to r^5 dependency on the scatterer's extent, see Fig. 3.3. In consequence the signal won't eventually exceed noise level.

In conclusion one must expect that the signal becomes quickly faint for smaller objects. Strong SHG signals were indeed experimentally only found for larger structures despite the fact that 4Pi focusing produces an 8-fold signal in the focal spot. Yet diffraction limited imaging of cellular myosin structures was successfully conducted

3. Second harmonic generation (SHG)

as described in more detail below.

3.4. Imaging of muscular actomyosin

3.4.1. Experimental setup

The 4Pi head described above - consisting of a beamsplitter and two opposing high NA objectives (two PL APO $63\times/1.20$ W CORR, Leica/ two PL APO $100\times/1.40$ CORR, Leica) - is mounted on a standard confocal microscope's turret (Leica TCS SP2). The light of a fs-pulsed Ti:Sa laser (Chameleon, Coherent), tunable over a broad band of frequencies, is coupled into the system via the IR-port of the microscope, splits up in two identical beams at the beamsplitter and is focused in the sample between the two objectives. The second harmonic generated signal is collected via the same objectives, merged at the beamsplitter, and is descanned and detected by a photomultiplier tube (PMT). Depending on the excitation wavelength a bandpass filter (447 nm, FWHM 60 nm, 514 nm, 30 nm FWHM) was inserted in the detection path. An additional 700 nm shortpass filter ensures blocking of the IR excitation light. The muscle fiber - specimen (images described below) were kindly provided by Sebastian Schürmann (group of Professor Rainer H.A. Fink, University of Heidelberg). The preparation of single muscle cells and isolated myofibrils from mouse muscle is described in detail in [18].

3.4.2. Experiments confirm simulations' results

The simulations' results were backed by thorough experimental research.

Bright images of muscular myosin were successfully obtained, see Figs. 3.5 and 3.7. Yet unambiguous and sufficient amounts of SHG signal of smaller samples could not be recorded. The experimental search for small SHG producing samples fit for standardization included technical probes like thin glass slides vapor coated with crystalline quartz as well as vesicles stained with Di-8-ANEPPQ potential-sensitive dye [97] as well as biological tissue like commercial collagen beads (Invitrogen). In the rare cases of detectable signal amount though, verification measurements like fluorescence counter-measurements or exciting second harmonic generation beyond the spectrally limited range of detection and not losing the signal, confirmed the signal's source to be multiphoton fluorescence (autofluorescence or fluorescence of reactive species generated in the course of phototoxic processes due to high excitation intensities) rather than second harmonic generation.

For muscular myosin though unambiguous SHG signal was obtained. Fig. 3.5 shows different isolated cells from mouse muscle. The cells were xy -scanned at $\lambda_{exc} = 880$ nm.

A muscle cell consists of longitudinal units, the so-called myofibrils, displaying

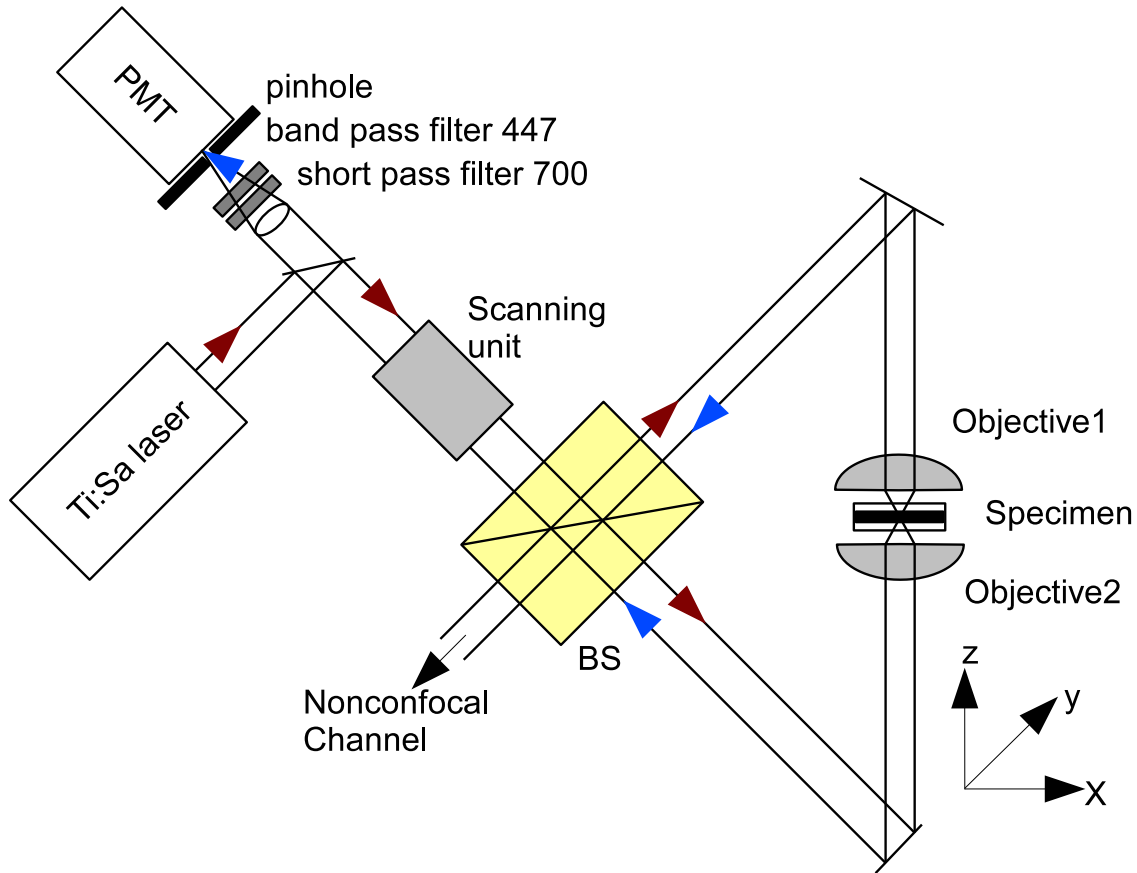


Figure 3.4.: Sketch of the principle beam path of the 4Pi microscope. The illumination light ($\lambda = 880 \text{ nm}$) of a fs-pulsed Ti:Sa laser is coupled in a confocal scanning microscope, split by a beamsplitter (BS) in two halves, focused by two opposing high-NA objectives and added up coherently in the focal spot in the specimen. The SHG signal is collected by the objectives, merged at the BS, spectrally selected by a 447 bandpass filter and detected confocally by a photomultiplier tube (PMT). A shortpass filter in the detection path ensures the incident light is blocked out from detection.

3. Second harmonic generation (SHG)

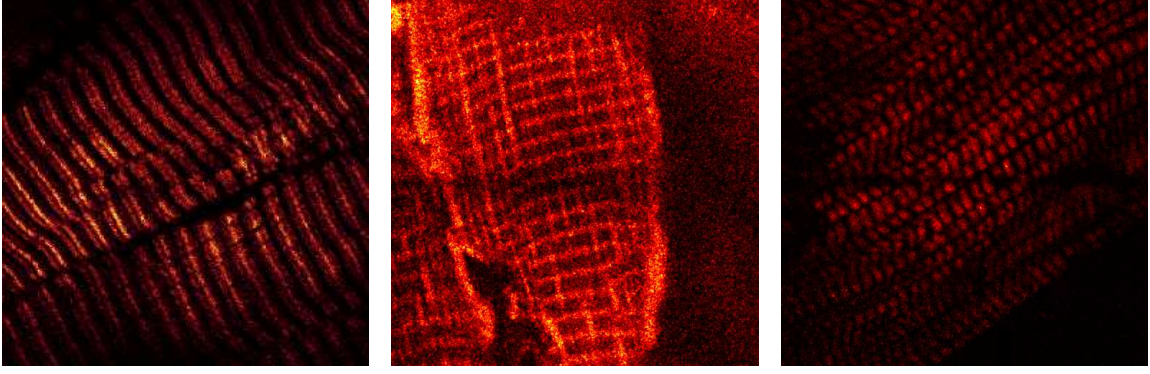


Figure 3.5.: xy -images of fibrillar myosin: the imaged areas are $35\text{ }\mu\text{m} \times 35\text{ }\mu\text{m}$ each. The images vary strong with the tissue's orientation with respect to the incident light's (fixed) polarization. *Left*: The signal follows the striation pattern in between the Z-lines. At some positions (left upper side) the SHG signal seems to form double strands, at other points (bottom right) the SHG signal appears single-stranded. *Middle*: Details of the striation pattern are lost, SHG signal bands are single-stranded throughout the cell and SHG bands perpendicular to the striation pattern appear. *Right*: A chain of point-like structures is seen completely unlike the striation pattern in the other two pictures.

a mean diameter of roughly $1\text{ }\mu\text{m}$. The myofibrils are made up of sarcomeres, $\approx 2\text{ }\mu\text{m}$ -wise repeating subunits, separated by z -planes, and consisting of an organized arrangement of myosin and actin filaments which make the cell appear cross-striated. The second harmonic generation ability of a muscle cell arises from this orderly arrangement of myofilaments within the myofibrils.

In the left image of Fig. 3.5 the SHG-signal is arranged in bands. At some points the bands seem to be double-stranded, at other positions they appear single-stranded. In the middle image double-stranded structures are not visible, instead bands perpendicular to the striation pattern appear. The right image in contrast shows a structure which does not resemble the striation pattern at all but is a point-like structure arranged in chains.

The detailed hyperpolarizability matrix for myosin was evaluated by Chu [29]. Simulations for point scatterers in the origin taking into account the myosin hyperpolarization matrix yielded the results shown in Fig. 3.6.

On the basis of these results some details in Fig. 3.5 possibly are mere polarization effects:

Regarding the xz -slice in Fig. 3.6 *upper middle* for a point scatterer, this detail could be explained by polarization alone: the single-stranded signal bands could stem from scatterers positioned in the plane $z = 0$ while scatterers generating a double-banded signal are positioned in planes above or below. This is, if the regarded detail in fact displays a mere polarization effect.

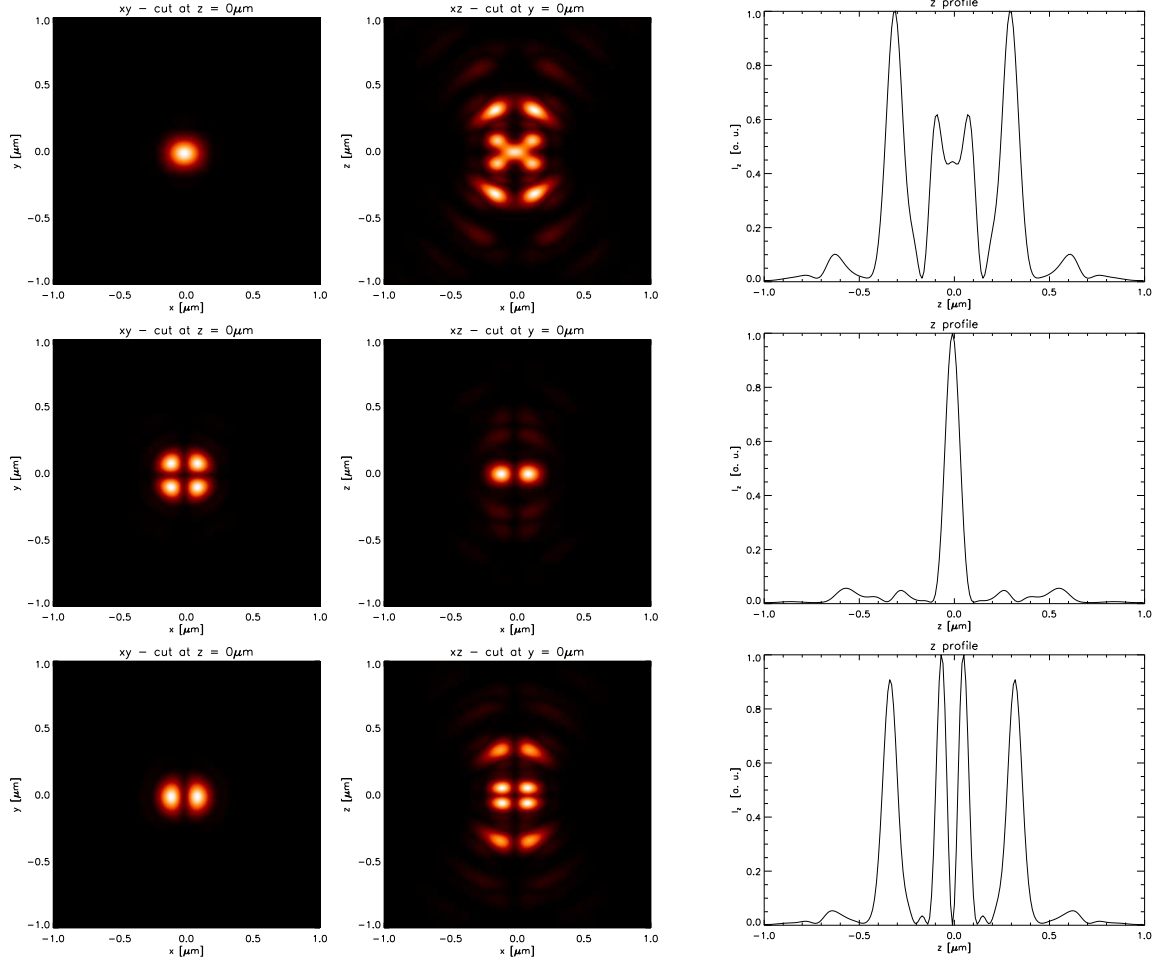


Figure 3.6.: Simulations of a single myosin point scatterer in the origin. The scatterer's optic axis is oriented along x (upper row), y (middle row) and z (bottom row) respectively. The left column shows xy -slices at $z = 0$, the middle one xz -slices at $y = 0$. In the right column the respective intensity z -profiles are displayed.

3. Second harmonic generation (SHG)

If, for example, the difference to the other two images, displayed in the right picture in Fig. 3.5, is a product of genuine physical nature, like a cell detached from the cover slip and (partly) crimped, a mere polarization effect, or a combination of both, is hard to tell since there is no bijective correlation between the SHG signal and the generating object.

The same holds true for xz -scanned SHG images as displayed in Fig. 3.7. The images show slices through 3 to 5 rows of single myofibrils lying on top of each other (the myofibrillar axes are pointing out of the image plane). The single myofibrils' signals mostly show the fourfold-stranded polarization pattern as it is generated by a myosin point scatterer in the origin, its optical axis aligned along the z direction as seen in Fig. 3.6 *bottom left*. Yet also 'ladder-like' and double-stranded structures as they are generated by a point scatterer with its optical axis along x and y (see Fig. 3.7) or like they are possibly generated by coherent superposition of the second harmonic fields of diverse (oriented) point-like scatterers are seen. Therefore with a certain probability the observed details (double, fourfold and ladderlike structures) in Fig. 3.7 are mere polarization artifacts for myosin and might in the best case allow more detailed insight in the material's properties [19].

3.5. Summary

Coherent Contrast mechanisms have never been applied to 4Pi microscopy before. These imaging techniques do not require dyes but use intrinsic generated signals thus ensuring the cellular morphology and metabolism remain unaltered. On a first view, 4Pi microscopy features several advantages over conventional confocal microscopy concerning these coherent contrast mechanisms:

- the interference of both opposing excitation and emission wavefronts are expected to provide for a 8-fold signal in the focus.
- due to the nonlinear nature of these coherent contrast mechanisms the 4Pi sidelobes are expected to be lowered significantly.
- since in 4Pi microscopy forward and backward scattered SHG signals interfere intensity variations depending on the imaged object's extent are expected to be diminished and thus it is expected that the total signal allows for the quantitative reconstruction of the imaged object's extent.

The fundamental properties of the coherent contrast mechanism of second harmonic generation (SHG) in 4Pi microscopy was thoroughly examined in experiment as well as in theory. Essentially it can be stated that

- SHG is accomplished by a confined group of non-centrosymmetric materials exhibiting highly ordered structures.

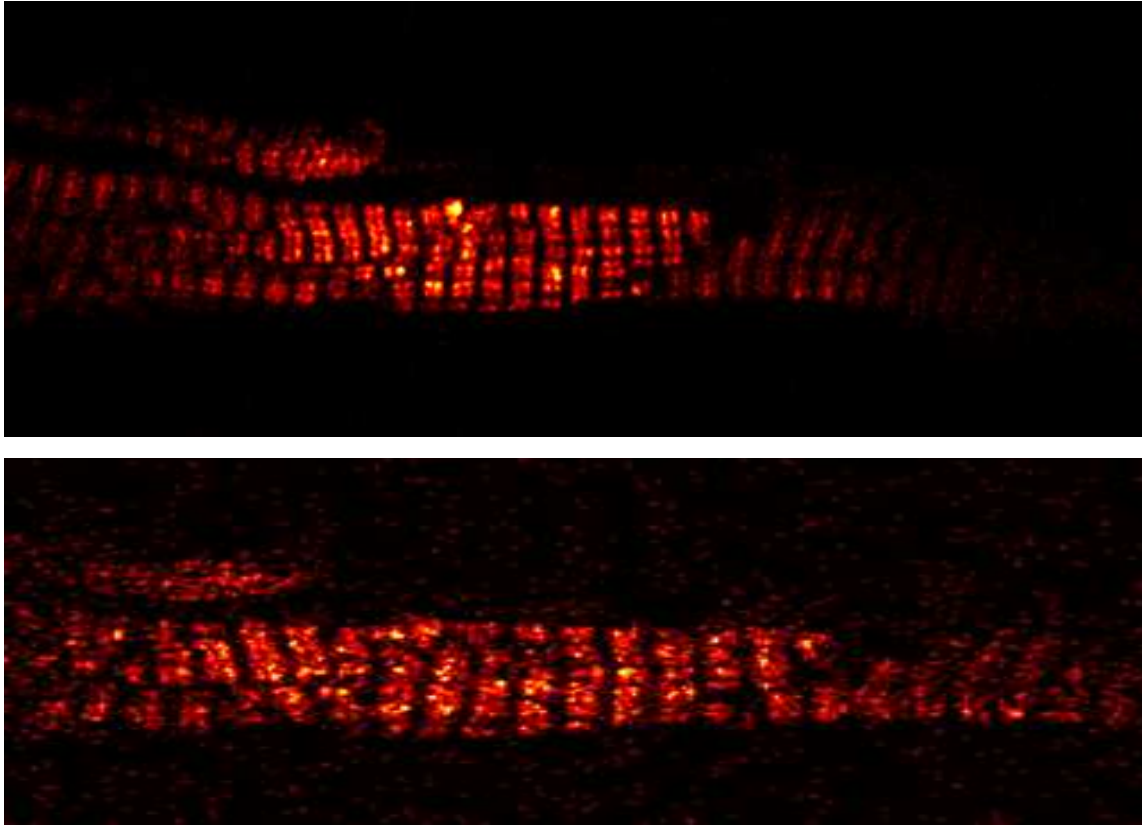


Figure 3.7.: xz -images of fibrillar myosin. The imaged areas are $68\,\mu\text{m} \times 11\,\mu\text{m}$ (*up*) and $48\,\mu\text{m} \times 15\,\mu\text{m}$ (*bottom*).

3. Second harmonic generation (SHG)

- the signal quickly fades for smaller objects despite the fact that 4Pi focusing produces an 8-fold signal in the focal spot.
- SHG signal was nevertheless obtained for objects extended over distances on the cellular scale.
- it is in general very difficult to suggest an object's physical structure from its SHG image without further detailed knowledge about its properties, among others especially its hyperpolarizability matrix and the scatterers' molecular orientation. These difficulties arise from the genuine coherent nature of the second harmonic generation process.

In summary: SHG was found to be no worthwhile alternative contrast mechanism to fluorescence for broadband applications. However, to reveal deeper insights into already well-known material properties or to render second harmonics generating objects label-free accessible for microscopy at all, SHG is a suitable, interesting, but niched vehicle.

4. Challenges in live cell microscopy

4.1. Imaging with water immersion objectives

One of the greatest challenges in live cell microscopy is to keep cells viable. Sounding trivial it is a stringent condition though. The most obvious criterion to be met to this aim is to keep and embed living cells in aqueous medium. A mandatory consequence of this insight is the utilization of water immersion objectives – at least as soon as imaging thick biological tissue (quite probable in live cell imaging) rather than an ultrathin fluorescent layer attached to the coverslip is concerned: differing refractive indices of embedding (water/buffer) and immersion (air, oil) medium and its respective micro-objectives would cause severe spherical aberrations thus leading to a decrease in signal intensity and axial resolution as well as a focal shift with increasing penetration depth implicating the imaged object appears elongated in axial direction [63], [35].

Today's available water objectives have a significant lower NA compared to oil immersion objectives. As a result the fluorescence collection efficiency as well as the resolution that can be gained are significantly lower. The axial resolution of a 4Pi microscope is mainly determined by the interference of the counter-propagating waves, and thus the wavelength of the fluorescence light though. Since the confocal z -profile is the envelope of the axial 4Pi profile, a deteriorated resolution in confocal microscopy reads as a distinct increase in axial sidelobe height in 4Pi microscopy. A height of less than 50% of the first-order sidelobes in 4Pi microscopy in turn is a crucial condition for succeeding in reliable removal of the sidelobes [12], [83].

The successful deconvolution of single photon 4Pi Type C images and almost artifact-free confocal imaging in 2photon 4Pi Type C mode are recent breakthroughs in 4Pi microscopy [83], [82]. These accomplishments were achieved with oil immersion objectives of the highest NA available these days and samples of perfectly matched refractive index [119]. Employing means of reducing the first-order sidelobes in aqueous live cell imaging enhances the imaging system's resolution the same way the utilization of higher-NA objectives does [89]. Thus these achievements are expected to work in live cell imaging too.

The concept of pupil function filtering [123], [88] is such an instrument. The successful implementation of a binary amplitude filter into a standard confocal 4Pi setup, see chapter 3, as well as in the MMM 4Pi setup, see chapter 2 of this thesis, is described in detail in the following paragraph.

4.1.1. Pupil function filtering in 4Pi microscopy

Binary pupil or Toraldo filters consist of absorbing (amplitude filter) or phase delaying (phase filter) concentric rings placed in the entrance aperture of the microscope's objective, see Fig. 4.1. Each ring creates an individual, radius-dependent diffraction pattern in the focal plane. Combining two rings in a way that for a certain spatial region in the focal plane the n th order diffraction maximum created by one of the rings overlaps with the $n + (2m + 1)^{\text{st}}$ order diffraction maximum created by the other one, so their amplitudes oppose each other, one can extinct the electromagnetic field emitted from that region given equal amplitude heights or equivalently equal ring areas. This works for the axial dimension also, which is the important one in 4Pi microscopy.

For an arbitrary region it is in this way theoretically possible to successively suppress the electromagnetic field around a very sharp center completely. Experimental applications are limited though: The Toraldo-filter-induced optimization simply is a redistribution process of the electromagnetic field in the focal plane, the field contributions suppressed in the considered region are shifted to and more pronounced at regions outside this area. Luckily, in confocal microscopy these regions are suppressed by the confocal pinhole though [56], [113], [117]. On the other hand, not only are the surroundings of the central peak but also the peak intensity itself diminished by applying the filter.

In 4Pi microscopy dark-ring filters are implemented for reducing the strong first interference side maxima or equivalently lifting the OTF around the critical frequency k_c [50]. This endeavor is more promising than a distinct axial resolution enhancement in confocal microscopy since it is already achieved optimizing small areas and thus keeping the filter's disadvantageous effects moderate [14], [15].

Experimental realization

Based on the results of the theoretically predicted effectiveness of sidelobe reduction for filters featuring different parameters [12] an amplitude filter was chosen consisting of a single dark ring separating the wave fronts passing the two opposing lenses into an inner part, $r \leq r_i = 0.34$, and an outer ring, $0.84 = r_e \leq r \leq r_{\text{max}} = 1$, each generating a standing wave. These add up coherently in the focus. The inner and outer radii of the dark ring define angles α_1 and α_2 ; α_{ap} is the aperture angle of the water immersion objectives implemented, two PL APO 63 \times /1.20 W CORR, Leica. The filter itself was fabricated by mounting an aluminium ring on an optical-grade quartz flat.

The field of the two lenses is calculated according to equation 2, the integrals $I_{0,1,2}$ being computed for the pupil amplitude function

$$F(\theta) = \begin{cases} 1 & \theta \leq \alpha_1 \vee \alpha_2 \leq \theta \leq \alpha_{\text{ap}} \\ 0 & \alpha_1 \leq \theta \leq \alpha_2 \end{cases} . \quad (4.1)$$

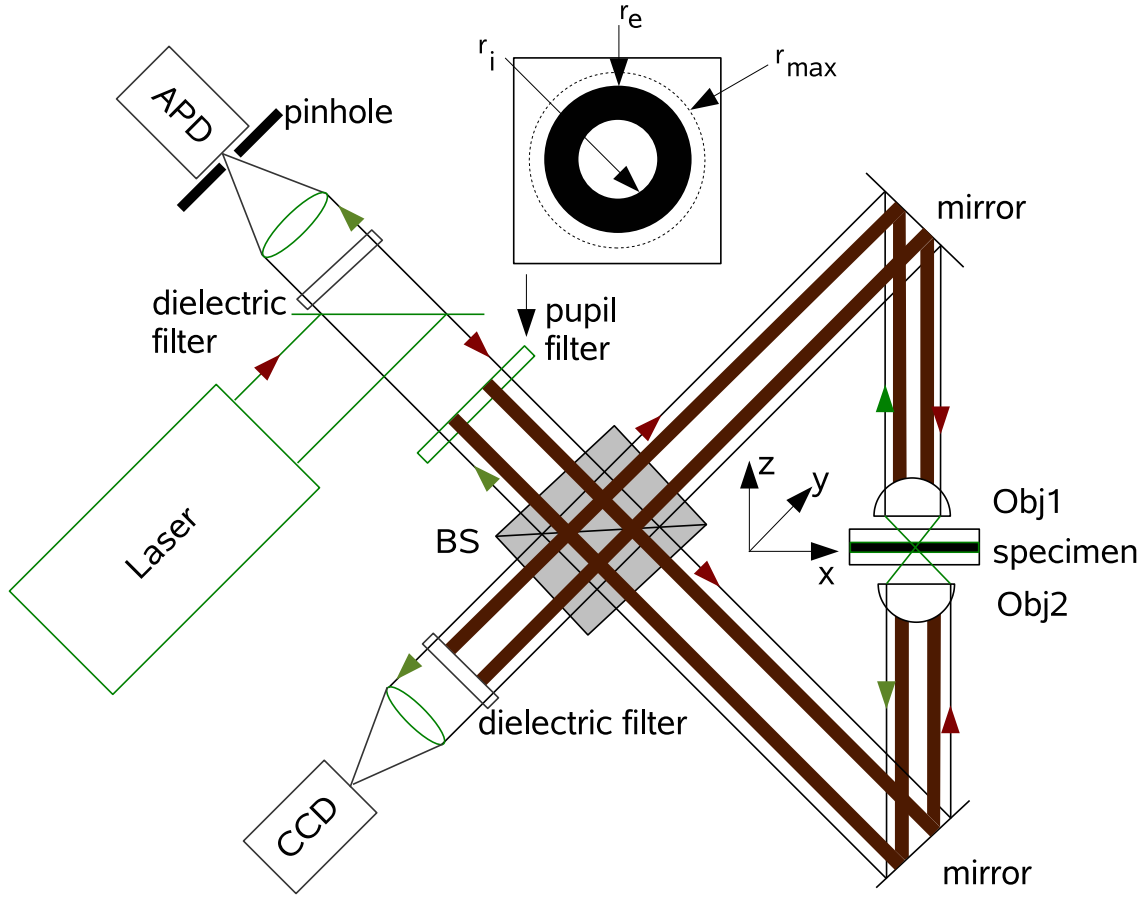


Figure 4.1.: Sketch of pupil function filtering in a 4Pi microscope. The amplitude filter is implemented in a pupil plane of the 4Pi microscope. The light of a laser passes the filter and is split by a beamsplitter (BS) in two halves, focused by two opposing high-NA objectives and added coherently in the focal spot in the sample. The fluorescence signal is collected by the objectives and merged at the BS. The part of the fluorescence leaving the BS's nonconfocal output is spectrally selected before it is detected by a CCD camera. The part leaving the confocal output passes the amplitude filter again, is descanned and spectrally selected before detected by an APD.

4. Challenges in live cell microscopy

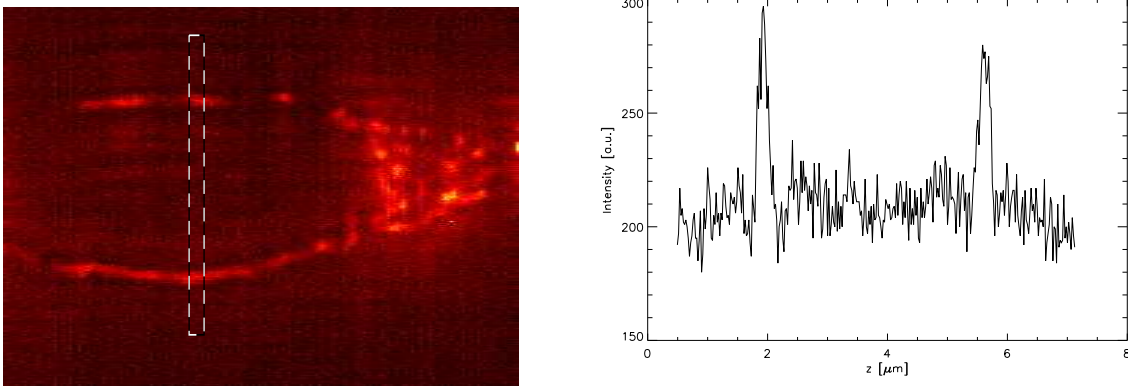


Figure 4.2.: *Left:* xz -slice of a two-photon dark-ring filtered raw image of Alexa488-stained microtubules wrapping around the nucleus in a primary human fibroblast. The imaged area is $14\text{ }\mu\text{m} \times 8\text{ }\mu\text{m}$. *Right:* The axial profile displays marginal sidelobes seldom exceeding the noise level.

If the opposing wavefronts without Toraldo filter are adjusted to constructive interference, the two standing-wave fields interfere constructively in the focal spot while the fields at the axial side lobes do not any longer due to the differing peak-to-peak distances of the standing waves. Thus they cancel each other partially. The energy once inherent in the first side lobes is shifted to higher - order parts and is suppressed there by either multiphoton excitation or confocalization.

In Fig. 4.2 a xz -slice as well as the axial profile of the microtubular network of a primary human fibroblast is shown. The cells were kindly provided by Jasmin Zahn (group of Professor Dr. J. Spatz, University of Heidelberg).

The primary cells were derived from a 54 years old human donor in the clinical center of the University of Ulm and cultivated at cell culture conditions of 37° and 5% CO_2 in DMEM enriched with 10% FBS and 1% P/S for 36 hours before they were seeded on thin glass coverslips.

For fixation a 4.5% paraformaldehyde (PFA) solution was used. The cells were incubated for 15 minutes. After a rinsing step in $1 \times \text{PBS}$ the cells were permeabilized in Triton. For immunostaining the cells were stained in a two step process. First $1\text{ }\mu\text{l}$ of primary antibody (mouse anti-tubulin, Invitrogen) per coverslip was used (for one hour). Next the coverslips were rinsed and incubated with $1\text{ }\mu\text{l}$ of the second antibody (Alexa488 anti-mouse, Invitrogen) per coverslip for another hour.

The pupil filter described above was inserted in the free accessible pupil space of the MMM 4Pi setup, see Figs. 2.3, 2.5. Fluorescence was excited in two-photon mode at $\lambda_{\text{exc}} = 780\text{ nm}$ and was non-confocally detected in a widefield scheme by a CCD camera (pco sensicam). A 514 nm (FWHM 40 nm) bandpass filter in the detection path blocked the excitation light. Dispersion was adjusted for (c/c)-interference in the nonconfocal channel.

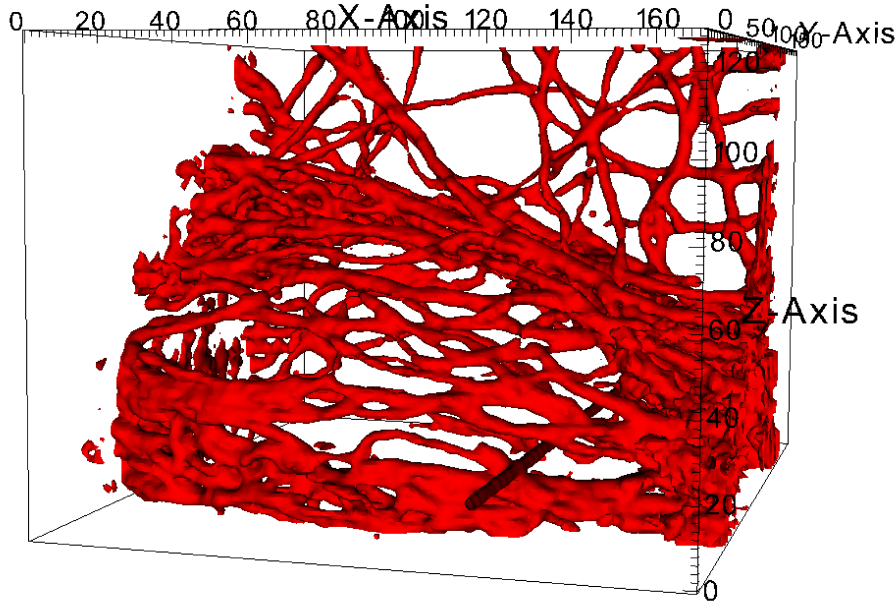


Figure 4.3.: Two-photon dark-ring image of microtubuli in a human fibroblast stained with Alexa488. Shown is a 3D rendered $14\text{ mm} \times 8\text{ }\mu\text{m} \times 10\text{ }\mu\text{m}$ - section of the cell's nuclear region.

Note that the data shown is raw data without any digital post-processing. The sidelobes are readily suppressed by the amplitude filter, thus the microtubular network is unambiguously retrieved from the image. Single microtubuli wrapping around the nucleus are exhibiting sidelobes hardly exceeding the noise level and thus are received practically sidelobe-free. Denser parts of the network in the periphery of the nucleus exhibit a noticeable off-set and the minima in the z -profile are filled to a certain degree yet the physical structure still is unambiguously perceptible by eye in the raw data image and artifact-free rendered in 3D by the free license visualization software VisIt, see Fig. 4.3.

This is a noteworthy result: Implementing a simple binary pupil filter into a conventional 4Pi setup results not only in as good as artifact-free two-photon images and thus renders deconvolution optional. But this is true and works reliably even without a confocal pinhole in a widefield detection mode which is a mandatory condition for reasonably implementing the filter in the MMM 4Pi setup.

It should be emphasized that complementing multiphoton excitation by a simple optical component, and thus physically engineering the resulting PSF, the microscope's performance is improved to the point of rendering mathematical image post processing superfluous while retaining axial superresolution. Thus the interpretation of raw data here is straight forward and efficient.

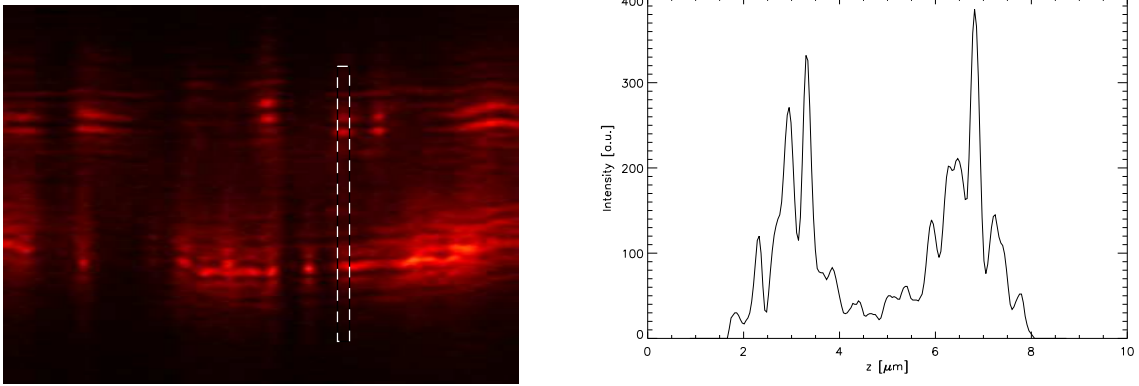


Figure 4.4.: Single-photon dark-ring image of microtubules wrapping around the nucleus in a human fibroblast stained with Alexa488. *Left:* Microtubules are wrapping around the nucleus in a human fibroblast cell. The $15\,\mu\text{m} \times 10\,\mu\text{m}$ – xz -slice displays strong sidelobes and a noticeable background in the denser regions of the nuclear periphery. *Right:* The axial profile exhibits increased minima, sidelobes of $\approx 45\%$ and a noticeable offset.

The ability to image practically sidelobe-free is a real advantage in live cell microscopy: xy -scanning a sample along z , thus z being the slowest axis in the process of scanning, will result in sidelobes shifted significantly with respect to the main maximum if the specimen moves faster than it takes to record a whole axial profile. Since the degree of distortion depends on the unpredictable and highly non-constant dynamics of the living specimen this cannot be compensated by data post-processing in general. Deconvolution of such data may no longer be possible. Without the need for deconvolution due to negligible sidelobes by a binary pupil filter, recording a sample with fast dynamics does not pose a problem.

Additionally, pupil function filtering entails further advantages obtained otherwise only by implementation of the higher-NA oil objectives and matching embedding medium: single photon 4Pi Type C data acquired via the confocal detection channel and using a binary amplitude filter exhibit sidelobes less than 50% and thus sidelobe removal in these images is possible. This is demonstrated in Fig. 4.4, exhibiting the same cell as seen imaged in multiphoton mode in Fig. 4.2.

The excitation wavelength was set to 488 nm and the pinhole diameter was set to 0.5 Airy. A $514\,\text{nm} \pm 40\,\text{nm}$ bandpass filter ensured the excitation light was cut out. The image was smoothed 3 times and 15% of the background noise was removed.

Comparing Figs. 4.2 and 4.4 it is obvious that while for multiphoton excitation the fluorescence’s quadratic dependence counteracts the effects of sample-induced aberrations, these effects have a distinct impact concerning single photon excitation. For example, the profiles of single microtubuli wrapping around the nucleus in Fig. 4.4 exhibit already a noticeable offset as well as a prominent decrease in modulation

depth and pronounced sidelobes. Also a distinct shift of the PSF's relative phase is clearly visible where light transmits the cells' nucleus: it is no longer possible to adjust phase for (c/c)-interference throughout the whole confocal image. While the PSF of the microtubules at the nuclear bottom periphery exhibit (c/c)-interference the wavefront's phase is shifted upon passing the dense nucleus resulting in a (d/c)-interference pattern at the top nuclear periphery. Thus aberrations caused by a mismatch in refractive index of the optically denser nucleus and the aqueous buffer embedding medium, are clearly obvious for single photon excitation.

A drawback already inherent in single photon excitation mode [27], [30] is the increased overall bleaching of the sample. This overall bleaching is additionally reinforced by the way the pupil filter is implemented, see Fig. 4.1: in the case here not only the excitation light passes the amplitude filter but also the fluorescence which results in a suboptimal efficiency in fluorescence light detection which in turn has to be compensated by an increase in excitation intensity leading to increased bleaching. So it was hardly possible to image the same stack successively more than about 5 times, depending on the excitation wavelength, the fluorophore involved and the sample preparation. This drawback could be ameliorated implementing the filter in a way it is only blocking out the excitation light partially while the fluorescence is not affected, like it is for example in a setup accomplishing detection via another channel than excitation takes place.

Thus pupil function filtering complementing single photon excitation might not be the cure-all yet it succeeds for the first time in rendering images of aqueous biological samples accessible for 4Pi microscopy. Without aperture filter sidelobes exceeding 60% – 70% of the main maximum's height in biological tissue inhibit reliable deconvolution.

Additionally an appropriate deconvolution has to compensate for the shift of the phase along the penetration depth z and the system's PSF has to be computed taking into account the pupil amplitude function 4.1. The algorithm used throughout this thesis to remove the sidelobes, taking into account axial phase variations, was developed at the German Cancer Research Center in Heidelberg (group of Stefan Hell, Johann Engelhardt), see appendix C. The algorithm reduces the 3D PSF deconvolution to the just one-dimensional axial profile deconvolution in order to simplify sidelobe removal. This simplistic approach allows for almost real-time (< 1 s per frame) interactive data processing including an axial phase variation. Thus (optimizing) side-lobe removal becomes unprecedentedly efficient. This efficiency is all the more important for work with large amounts of data like 3D time - series.

The single-photon images of microtubuli wrapping around the nucleus were axially deconvolved applying this algorithm which was modified to account for the aperture filter. The results shown in Fig. 4.5 demonstrate its ability to unambiguously remove the axial sidelobes. Thus 3D rendering is possible and demonstrated spectacularly in Fig. 4.6.

4. Challenges in live cell microscopy

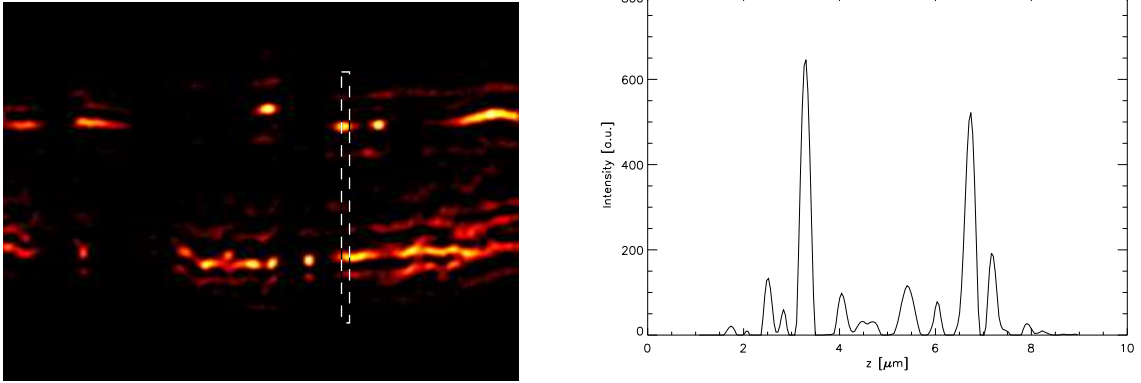


Figure 4.5.: Single-photon dark-ring image of microtubules wrapping around the nucleus in a human fibroblast cell after removal of the axial sidelobes. *Left:* xz -slice of microtubules wrapping around the nucleus of a human fibroblast cell with almost non-perceivable sidelobes. This convincing sidelobe removal was accomplished although the phase shifted notably in axial direction. *Right:* The axial profile exhibits remaining artifacts mostly not exceeding 15% of the main maximum's height.

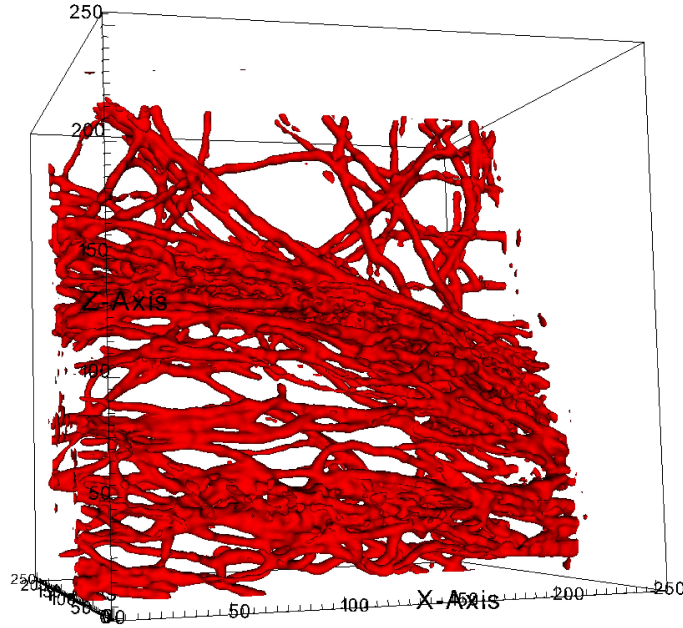


Figure 4.6.: 3D single-photon dark-ring image of microtubules wrapping around the nucleus in a human fibroblast. The pictured area is $15 \mu\text{m} \times 10 \mu\text{m} \times 15 \mu\text{m}$. Artifacts are removed convincingly.

4.1.2. **Imaging thick scattering tissue**

In the last paragraph it was shown, at least for a single layer of cells directly attached to the coverslip, that pupil function filtering is capable of providing imaging biological tissue with water immersion objectives with the advantages otherwise only achievable by the implementation of higher-NA oil objectives entailing embeddings utterly unfit for the survival of the cells.

Yet for thick scattering biological tissue, up to $10\ \mu\text{m}$ and more, specimen-induced aberrations are expected to gain importance rapidly for single photon as well as for multiphoton excitation. The effects of sample-induced aberrations are already noticable for a single layer of cells. In combination with a worse penetration depth of single photon compared to multiphoton excitation single photon microscopy is not the preferred method in general.

In multiphoton excitation microscopy sample-induced aberrations will also become clearly visible with increasing sample thickness though. In critical cases aberrations will even inhibit the implementation of pupil filters: Since multiphoton cross-sections are $\approx 10\times$ smaller compared to their single photon counterparts anyway, the limits for tolerance concerning inefficiencies in excitation as well as detection are quite tight. Imaging thick samples, at least one of the two interfering 4Pi wavefronts has to pass dense tissue over a distance of several wavelengths and thus a lot of light will be scattered and is lost for multiphoton excitation. In consequence the fluorescence signal will decrease. Additionally implementing a binary amplitude filter will block a further significant part of the excitation light: adding a filter in excitation only will result in a 16-fold decreased main maximum in the system's PSF [12]. Thus fluorescence will drastically decrease. Hence, for thick scattering samples stained with dyes exhibiting small two-photon cross-sections, the weak fluorescence will forbid the additional implementation of a dark ring filter.

Furthermore even near-infrared excitation light will become visibly phase shifted upon passing an adequate distance through optically dense tissue. Thus phase is adjusted for strict (c/c)-interference only for single planes throughout the sample. While decreasing the first order side maxima in these planes filtering will not do so for planes of (d/c)-interference or mixed cases (not wholly destructive/constructive) since the sidelobe-main maximum – distance varies for the different interference patterns. In contrast, draining energy out of a certain region thus enhancing the surroundings generates sidelobes of its own and in this way filter-induced sidelobes overlaying the regular 4Pi PSF's ones will complicate image interpretation not insignificantly.

Thus the implementation of a binary amplitude filter for imaging thick scattering and optically dense tissue inducing a phase variance along z will result in problems prevailing over the filter's advantages. For samples less extended, exhibiting a constant PSF throughout the imaged area (no phase shifts), though, the application of pupil filters results in noteworthy advantages, similar to these gained by the implementation of oil immersion objectives.

4. Challenges in live cell microscopy

In the cases of imaging live yeast and PML nuclear bodies as described in Chapter 2, dark ring filtering was not implemented: The PMLs were imaged in the nucleus, the optically densest region within a cell exhibiting a refractive index ($n_{\text{nu}} \approx 1.4$) differing strongly from the embedding medium's one ($n_{\text{buf}} \approx 1.33$). When dark ring filtering is not reasonable the image quality might instead be enhanced by matching the refractive index of the embedding medium further to that of the optically dense sample. This increase is accomplished adding large amounts of, for example, long-chained sugars like dextrane, but also mowiol or agar to the embedding medium. Thus it is possible to adjust the refractive index of buffer embedding to a value between $n_{\text{buf}} = 1.33$ and almost $n_{\text{buf}} = 1.40$ continuously. Better matching refractive indices of embedding medium and sample will limit the specimen-induced aberrations described above. The price for the reduction of sample-induced aberrations is an increase in aberrations induced by refractive index mismatch of embedding and immersion medium though. The question, to which degree the cells' metabolism, morphology and dynamics are altered by the addition of non-cellular substances, is also to be addressed seriously. Yet it might be advantageous to trade refractive index mismatch of embedding medium and sample for that of embedding and immersion medium. The first is prone to induce unpredictable and non-linear since specimen-specific aberrations, for example a strong variation of phase only in the cell's perinuclear region. Then again, the latter has been shown to induce phase shifts which are linear over a large distance [35] and thus can be corrected actively. Active compensation is achieved for example by altering the length of one of the 4Pi's arms linearly in accordance with the sample's change in z -position during the scanning process [7]. Matching the refractive indices of sample and embedding medium is no strict guideline for imaging thick tissue, however, but has to be decided individually depending on the properties of the specimen of concern, the imaging period and the advantages and disadvantages entailing this action. Another set-screw of both image quality and customization of live cell 4Pi microscopy is the development of enhanced algorithms enabling automatic 3D - deconvolution of 4Pi microscopy data with arbitrary phase. A maximum a posteriori based method aiming in this direction is, at the time being, developed at the MPIBPC in Göttingen (Giuseppe Vicidomini). This approach is expected to enhance both throughput and range of applicability of 4Pi live cell microscopy by rendering data, otherwise critical for one-dimensional deconvolution, accessible for 4Pi microscopy for the first time.

4.2. Summary

Live cell microscopy demands viable cells. In consequence both aqueous embedding and imaging with water immersion objectives become mandatory.

In this chapter the challenges arising from the utilization of aqueous embedding medium and water immersion objectives were treated:

- Water immersion objectives feature a lower numerical aperture (NA) compared to oil immersion objectives and therefore an imaging system relying on water immersion objectives displays a decreased resolution. It could be demonstrated experimentally, that pupil function filtering is able to enhance the resolution of an imaging system relying on NA 1.2 water immersion objectives the same way the utilization of NA 1.46 oil immersion objectives does: Two-photon, pupil-filtered images of aqueous embedded biological tissue display negligible sidelobes. This fact holds even true without the confocal pinhole in widefield detection mode. Deconvolution of this data is no longer necessary. Even single photon, pupil-filtered images are rendered accessible for the first time for 4Pi relying on water immersion objectives.
- Refractive index (RI) mismatch of specimen and embedding medium can no longer be matched perfectly. In consequence specimen-induced aberrations become a limiting factor in image quality. In former setups specimen-induced phase shifts were compensated actively during recording. Both adjustment of the imaging system and data acquisition were thus complicated. In the presented setup existent specimen-induced phase-shifts were recorded and accounted for afterwards in data post-processing. An algorithm reliably regarding for axial phase shifts is described and successfully implemented.

A physical option to improve the RI mismatch problem is proposed also: Enriching the embedding medium with large amounts of agar, mowiol or similar substances unaffected the cells' morphology and metabolism better matches the specimen's RI to that of the embedding medium. Although this way specimen-induced aberrations are traded for aberrations originating from RI mismatch of embedding and immersion medium this procedure can improve the imaging system's overall image quality.

5. Conclusion and Outlook

4Pi microscopy was adapted for the first time to live cell imaging by Bewersdorf et al. and Egner et. al. [10], [38], [37].

In order to push the limits of 4Pi live cell imaging further, a new method of multispot-generation via the stacking of birefringent crystals in multifocal multiphoton microscopy was developed and is presented in this thesis. The stacking of birefringent crystals, specifically a stack of Wollaston prisms, are not only convenient for the implementation and adjustment of beamlets of perfectly uniform intensity but the beamlets generated are also of high optical quality.

The reliability and applicability of a MMM-4Pi setup incorporating 4 Wollaston prisms was convincingly demonstrated for imaging fusion and fission events of living yeast *S. cerevisiae* as well as the movement of PML nuclear bodies in human osteosarcoma cells U2OS.

The recording of an average-sized 3D data stack utilizing 16 parallel foci was accomplished in less than 10 seconds which is a 13-fold increase compared to a corresponding single-beam setup.

The 4Pi system's axial superresolution of ≈ 120 nm in widefield detection mode was reliably provided throughout the imaging process: The PML bodies' hollow-sphere structure - inaccessible for conventional confocal microscopy - as well as details in the dense mitochondrial network of living yeasts were resolved with high precision throughout.

Simultaneously, the viability of living cells was enhanced: the sample is normally sandwiched between two glass coverslips. The utilization of a dipping water immersion objective compensates for one of the glass coverslips and permits a bigger reservoir of nutrient culture medium. Moreover, an environmental chamber was designed maintaining a temperature of 37° .

In order to extend the applicability of 4Pi live cell imaging to un-labelled specimen second harmonic generation (SHG) was thoroughly examined as an alternative coherent contrast mechanism for the first time in 4Pi microscopy.

Second harmonic generation is confined to non-centrosymmetric materials exhibiting highly ordered structures.

Although the 4Pi optic allows for an 8-fold enhanced signal due to both interference of the excitation light and interference of forward and backward scattered SHG light the total signal is proportional to the 5th power of the object's radius and therefore the SHG signal rapidly decreases for smaller objects. Nevertheless coherent imaging of fibrillar myosin at the cellular level was successfully conducted. Due to

5. Conclusion and Outlook

the coherent nature of this imaging technique there is no bijective correlation between the image and the imaged object, i. e., the SHG-image of an object does not allow unambiguous reconstruction of structural information about the object without further information. Second harmonic generation turns out to be an interesting but niched method revealing further insights into known structures rather than a broad spectrum of new insights leading to wide applicability of the method.

However, other methods were identified enhancing the applicability of 4Pi microscopy.

The use of dark ring filters make aqueous tissues accessible for 4Pi single-photon microscopy for the first time. Even more noticable, aqueous biological samples are imaged practically sidelobe-free in two-photon 4Pi microscopy and this fact holds true even in a widefield detection scheme. Refractive index mismatches in the specimen inevitably result in an axial phase shift in the recorded data. While in former setups active compensation of these phase shifts complicated data acquisition and adjustment of the system, a simple and reliable algorithm was shown in this thesis to compensate for the axial phase shift in data post processing. 4Pi microscopy of aqueous tissue has therefore become convenient and broadly applicable.

With the advent of enhanced algorithms for data post processing and improved refractive index matching the imaging of thick biological tissue might in the future only be limited by the objectives' working distance of $\approx 200\ \mu\text{m}$.

These improvements are not confined to 4Pi microscopy.

Although high resolution imaging techniques of both STED and PALM type overcome the diffraction limited resolution of the 4Pi, incorporating 4Pi optics is still the best starting point to extend these microscopy methods to three dimensional analysis [114].

Experiences in 4Pi live cell imaging are therefore valuable sources of information for 4Pi augmented STED or 4Pi augmented PALM setups. Especially the method of generating optically perfect multispots via the stacking of birefringent crystals will gain in relevance: In order to improve the live cell imaging abilities of 4Pi augmented systems it is applicable to any MMM-4PiSTED or MMM-4PiPALM setup without significant limitations.

This thesis presents a significant step forward to fast 3-dimensional live-cell microscopy of sub-diffraction spatial resolution.

A. Advantages of the xz -scan option for wide-field detection

The xz display is especially helpful for adjusting the 4Pi microscope of type C to the preferred case of constructive interference of the excitation and at the same time the fluorescence light, the so-called (c/c)-interference, in the non-confocal channel. Only in this case the (wide-field) resulting PSF's 0th order maximum dominates while its neighbouring side lobes are lowest due to different sidelobe distances of the illumination and detection PSF stemming from the disparity of the excitation and detection wavelength. Thus imaged data is rendered both more versatile for digital post processing and interpretation. Sure enough this visual aid is already given by the confocal image of the z -scan directly detected by an APD (Perkin&Elmer) using the beamsplitter's confocal output after the Wollaston prisms have been taken out of the pupil space. Having successfully managed the alignment the prisms can be put back and the image acquisition can be started.

Yet the phases of the emission light leaving the beamsplitter's two outputs are complementary. This can be derived from energy conservation considerations, see Fig A.1. The fluorescence collected by the opposing objectives is merged at the beamsplitter leaving it in two directions. For an ideal, non-absorbing beamsplitter, energy conservation of the system's fluorescence energy demands $\|E_r\|^2 + \|E_t\|^2 + \|E_r\|^2 + \|E_t\|^2 = \|E\|^2 + \|E\|^2 = \|E_r + E_t\|^2 + \|E_r + E_t\|^2 = 2 \cdot \|E_r\|^2 + 2 \cdot \|E_t\|^2 + 2 \cdot (E_r^* \cdot E_t + E_t^* \cdot E_r) \Leftrightarrow E_r^* \cdot E_t + E_t^* \cdot E_r = 0$. For the phases of the reflected and transmitted fields this is equivalent to $e^{i(\phi_r - \phi_t)} = -e^{i(\phi_t - \phi_r)} = e^{i\pi} e^{i(\phi_t - \phi_r)}$. This is only true for $\phi_r - \phi_t = \pi/2$. Changing the path length in one of the 4Pi's interferometric arms accordingly by $-\pi/2$ to obtain constructive interference $\Delta\phi = 0$, will inevitably result in a phase of $-\pi$ at the other interferometric arm. Generally the two interferometric arms display a phase difference of π .

Thus whenever one of the two emerging beams displays constructive phase the other's phase is necessarily destructive. Vice versa trying to adjust for destructive phase in the confocal image so to obtain constructive interference in the non-confocal image is not promising since the destructive case is not unambiguously recognized, so using the confocal image as visualization aid is not a realistic alternative.

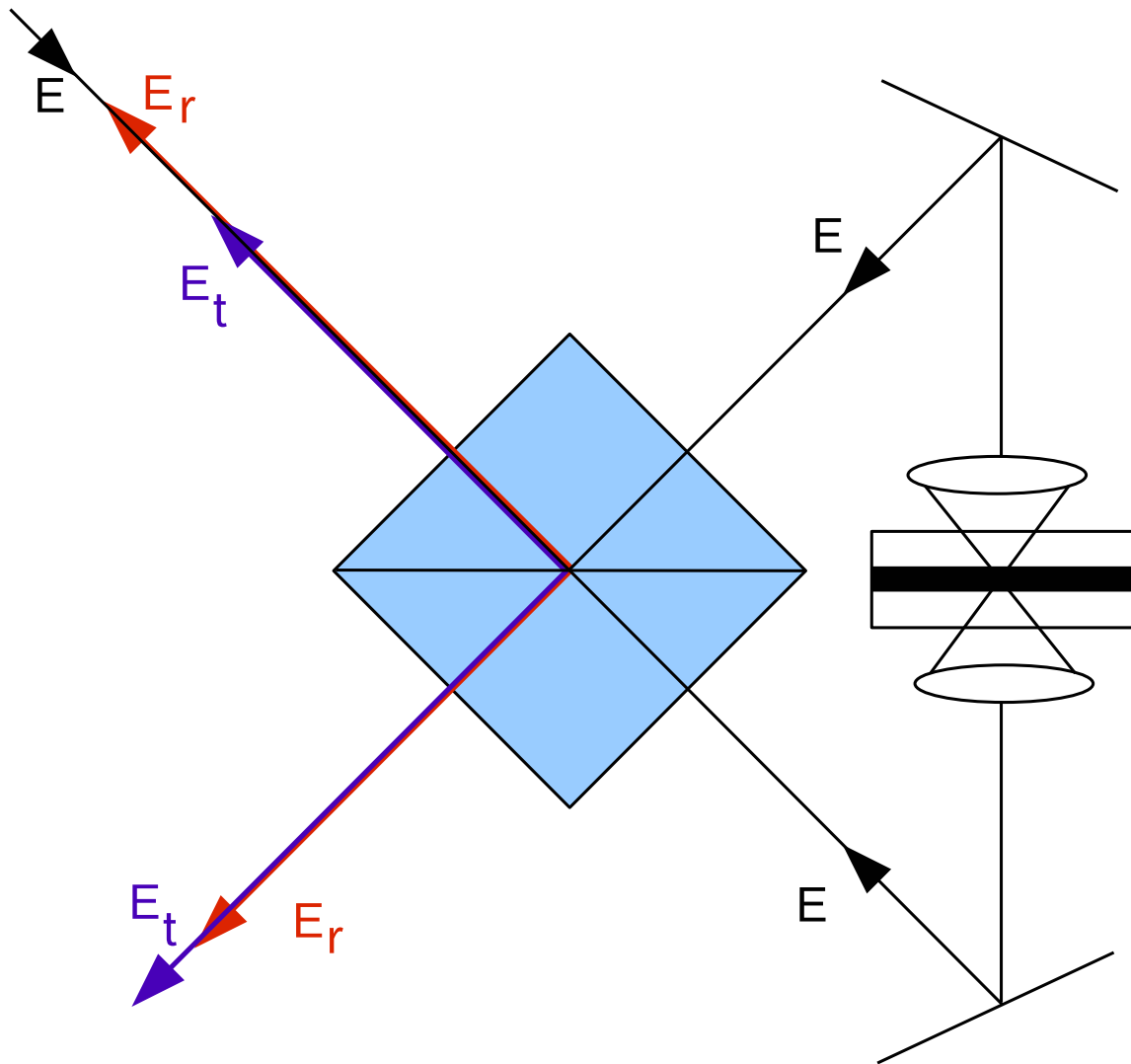


Figure A.1.: The fluorescence collected by the opposing objectives is merged at the beamsplitter leaving it in two directions. For an ideal, non-absorbing beamsplitter, energy conservation of the system's fluorescence energy demands that the two interferometric arms display a phase difference of π .

B. Mode of scanning and respective field of view

For imaging live specimen 4 prisms were used to obtain 16 uniform beamlets arranged in a rhombus-shaped 4×4 array, see Fig 2.1. There are principally two ways to implement such an array of multiple beamlets:

The first way I will refer to as the tiled scan. In tiled scan mode the field of view is separated in 16 adjacent compartments, each scanned by a single beamlet, see Fig 2.1. The advantage of this mode of deployment obviously is the direct gain in imaging time by a factor of 16. This is the way to go when dealing with bright and quick moving samples. A disadvantage of this mode of deployment is the marginal remaining overlap of areas scanned by adjacent beams due to the generation-inherited fact that the spot-to-spot distance along x may differ slightly from that along y and thus, to avoid spaces left unscanned, the scanned areas of adjacent beams will overlap along one direction. This can be seen by imaging an ultra-thin layer of qdots, see Fig. 2.1. Yet this kind of grid-structure is only apparent in uniform samples while for biological specimen an effect of the minimal overlap is not observed. Since the free accessible pupil space in the set-up presented in this thesis limited the number of prisms to 4, there was no need for spot-to-spot distances to fall below the critical barrier for crosstalk to have an impact. Thus 4 prisms with a minimal spot-to-spot-distance of $4.8 \mu\text{m}$ create in this mode of scanning a field of view ranging from $21 \mu\text{m} \times 28 \mu\text{m}$ (field of view completely raster-scanned) to $21 \mu\text{m} \times 36 \mu\text{m}$ (maximal field of view with edges left unscanned due to the tiled arrangement's rhombus-shape).

The second way, see Fig B.2, I will refer to as the interleaved scan. In interleaved scan mode the overlap of all beamlets just coincides with the field of view. An excitation intensity leading to increased bleaching in a single-beam set-up is split up 16 times. Thus the single beamlets possess only $\frac{1}{16}$ of the incident beam's intensity and bleaching is avoided. Only in the overlapping region of the single non-bleaching beamlets the whole energy (modulo losses at the prisms) is added again in the specimen. Since different beamlets reach a sample point in the overlapping scan-region at different times though, the fluorophores excited by one beamlet have time for relaxation before being scanned by another beamlet and thus bleaching is alleviated. Interleaved scanning is thus the way to go for dark samples or samples exhibiting increased bleaching rather than for fast scanning. In this way a field of view of $\approx 36 \mu\text{m} \times 36 \mu\text{m}$ is created.

Just to give a complete review on the abilities of this MMM - 4Pi set-up the option

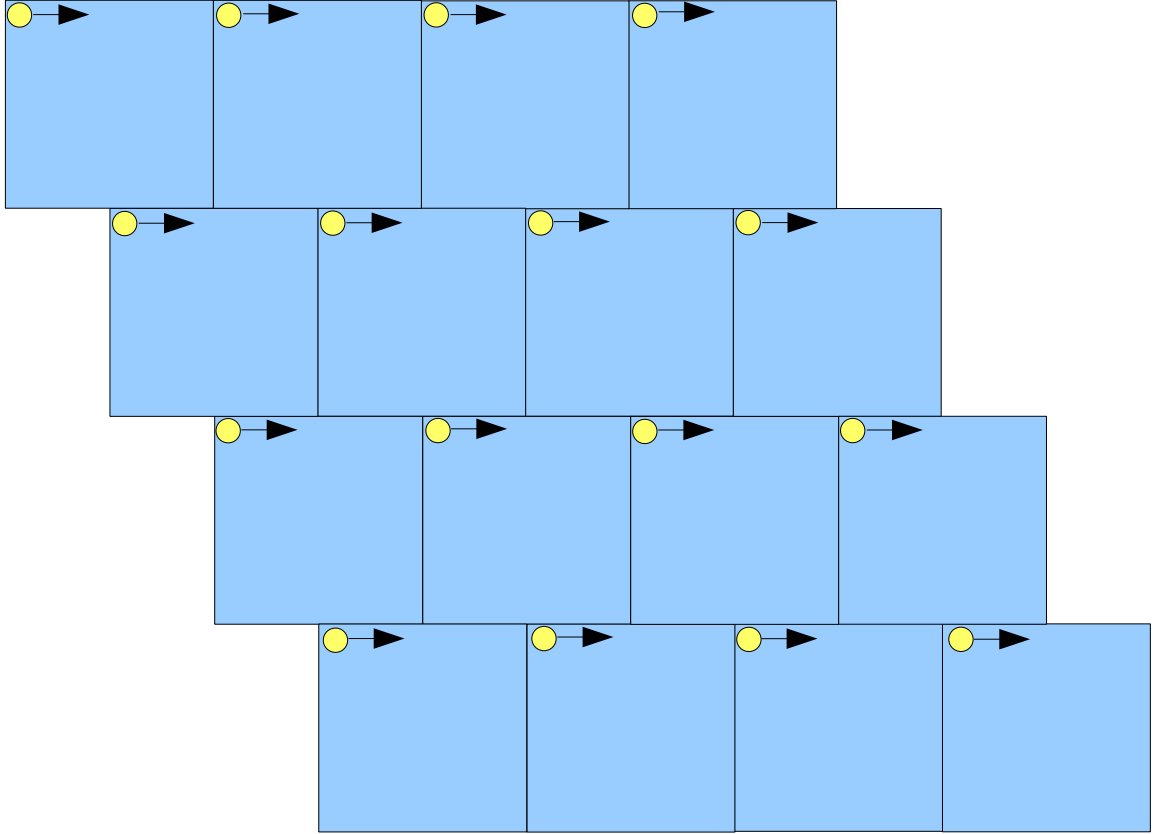


Figure B.1.: Sketch of focal spots in tiled scan arrangement. The focal spots (yellow) are aligned along 4 straight rows, which are relocated with respect to each other such that the resulting field of view (blue) is rhombus-shaped. Every focal spot scans a sub-area of the complete field of view.

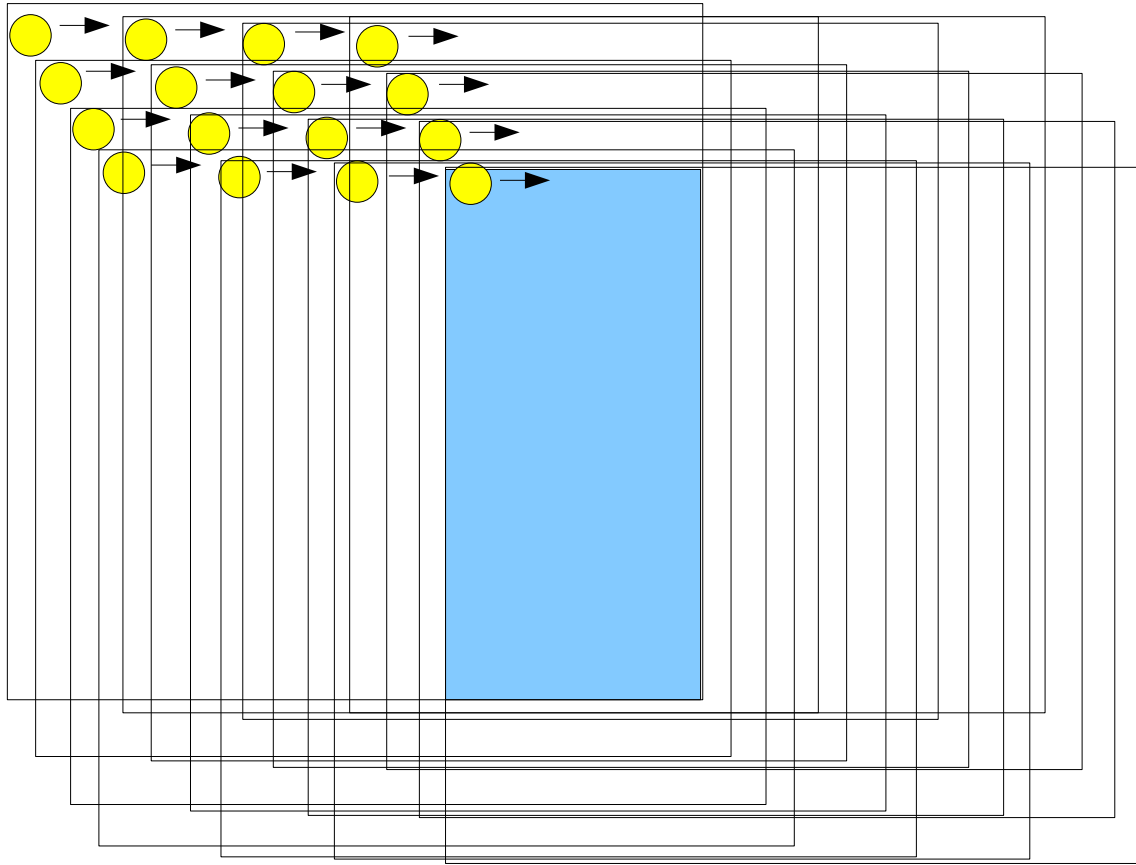


Figure B.2.: Sketch of the focal spots in interleaved scan mode. The lines, scanned by the 16 focal spots (yellow), are relocated with respect to each other and thus one scan addresses 16 different lines at the same time. The overlap of all 16 scanned areas coincides with the field of view (blue).

B. Mode of scanning and respective field of view

of xz - scanning, owing to the galvanometric mirror in the detection path, should be mentioned. This mode of scanning I will refer to as line xz -scanning. xz -scanning is limited to 4 single beamlets arranged along a row. This configuration results from turning the polarization of the two beamlets generated at the first prism by 45° by means of a $\lambda/4$ - waveplate upon entering the next prism. For beamlets not arranged in a horizontal line, fluorescence emitted upon excitation by foci addressing different positions along y would be projected onto the single xz -plane, in other words, in the way these xz -‘scans’ are done (projecting axial (z) information onto the y -axis), lateral (y) and axial information are merged in one 2D image. Without further means of distinguishing lateral (y) and onto the y -axis projected axial (z) information within a 2D image the only way left for acquiring unambiguous data is to ensure excitation to take place in a single plane $y = y_0$.

This may be an option for fast processes where 3-dimensional acquisition is no longer possible. Here still axial scanning could be done at 4-fold speed compared to scanning with a single spot.

3D data acquisition with the slow axis along y is of course also possible yet shifting the plane of xz -scanning along y will shift the image along y , additional to the shift due to the scanning along z , respectively. This movement can be compensated afterwards by an adequate algorithm and therefore imaging 3D data stacks by means of xz -scans is a bit more elaborate than simply doing xy -scans while moving the sample along z . Still it is a possibility of this set-up and might come in handy for samples moving too fast to attain reliable information along the slowest axis in the scanning process (which is z for xy -scans along z). This could be the case for processes happening due to sedimentation like fluorescent beads being dispersed in the embedding medium and sinking due to the gravitational force. Imaging a specimen like that doing xy -scans along z will result in an axially elongated bead in the image since the bead’s moving faster along z than the acquisition of a whole 3D data stack around it will take.

So especially for 4Pi imaging (the interesting axis being the axial one) the option of performing xz -scans is a clear advantage.

All three scanning modes, tiled, interleaved and line xz -scanning as described above, have been practiced in experiments. Yet for the fast recording of bright and extended samples as presented in section 2.4, tiled scanning was preferred. This mode allows to use laser powers, which would have been wasted in a single beam set-up, for rather increasing imaging speed than extending the region of excitation as it is done in interleaved scan-mode. Neither needs the recorded data to be digitally reconsidered to compensate for the additional movement along y as it is necessary in the line xz -scan mode.

C. Algorithm for interactive removal of the axial sidelobes

The axial 4Pi profile is approximated by a cosine squared function with a gaussian envelope:

$$\left[(1 - b) \cdot \cos^2 \left(\frac{\pi}{d} \cdot z + \phi(z_0) \right) + b \right] \cdot \exp \left(- \left[\frac{\sqrt{-\ln(h)}}{d} \cdot z \right]^2 \right).$$

Herein the parameters b , d , h and ϕ are describing the height of the profile's minima, the main maximum - sidelobe distance, the sidelobes' height (in the range of $[0, 1]$) and the phase respectively.

To account for amplitude filters three of these profiles are arranged along z , the middle one exhibiting a phase shifted by π compared to the outer ones.

The axial intensity pattern produced by the 4Pi optics is the convolution of the object with the 4Pi PSF. For a simplified sidelobe removal just the axial profile is modelled. For a discrete intensity profile the convolution operation becomes a simple matrix multiplication.

Thus for each column of a xz -image it is

$$\vec{I}(z) = \underline{\underline{PSF}}(z) \cdot \vec{O}(z).$$

Each row of the matrix $\underline{\underline{PSF}}(z)$ consists of the system's PSF for a certain z -position, $I(z)$ describes the recorded image and $O(z)$ the object. For deconvolution the inverse of every row H of the matrix $\underline{\underline{PSF}}(z)$ is generated according to conventional Wiener filters,

$$H^{-1} = \frac{H^*}{H^*H + \gamma}.$$

Thus the actual object is retrieved from the image by

$$\vec{O}(z) = \underline{\underline{INV}}(\underline{\underline{PSF}}(z)) \cdot \vec{I}(z),$$

whereas the rows of $\underline{\underline{INV}}(\underline{\underline{PSF}})$ contain H^{-1} .

Bibliography

- [1] Alberts, B., Johnson, A., Lewis, J., Raff, M., Roberts, K., and Walter, P. *Molecular biology of the cell*. Garland Science, New York 767-830 (2002)
- [2] Bailey, B., Farkas, D. L., Taylor, D. L., and Lanni, F. *Enhancement of axial resolution in fluorescence microscopy by standing-wave excitation*. Nature 366, 44-48 (1993)
- [3] Barad, Y., Eisenberg, H., Horowitz, M., and Silberberg, Y. *Nonlinear scanning laser microscopy by third harmonic generation*. Appl. Phys. Lett. 70, 922-924 (1997)
- [4] Bergmann, L., Schaefer, C., Niedrig, H. *Lehrbuch der Experimentalphysik*. Band III, Optik. Wellen- und Teilchenoptik. De Gruyter Press, Berlin (2004)
- [5] Bernardi, R., and Pandolfi, P. P. *Structure, dynamics and functions of promyelocytic leukaemia nuclear bodies*. Nat. Rev. Mol. Cell. Biol. 8(12) 1006-1016 (2007)
- [6] Betzig, E., Patterson, G., Sougrat, R., Lindwasser, O., Olenych, S., Bonifacino, J., Davidson, M., Lippincott-Schwartz, J., and Hess, H. *Imaging intracellular fluorescent proteins at nanometer resolution*. Science 313(5793), 1642-1645 (2006)
- [7] Bewersdorf, J., Egner, A., and Hell, S. W. *4Pi microscopy*. In Handbook of biological confocal microscopy. Pawley, J. editor Springer Press, New York 561-570 (2006)
- [8] Bewersdorf, J., Egner, A., and Hell, S. W. *Multifocal multi-photon microscopy*. In Handbook of biological confocal microscopy. Pawley, J. editor Springer Press, New York 550-560 (2006)
- [9] Bewersdorf, J., and Hell, S. W. *Picosecond pulsed two-photon imaging with repetition rates of 200 and 400 MHz*. J. Microsc. (Oxford) 191, 28-38 (1998)
- [10] Bewersdorf, J., Bennett, B. T., and Knight, K. L. *H2AX chromatin structures and their response to DNA damage revealed by 4Pi microscopy*. PNAS 103(48), 18137-18142 (2006)

- [11] Bewersdorf, J., Schmidt, R., Hell, S. W. *Comparison of I5M and 4Pi-microscopy*. J. Microsc. 222, 105-117 (2006)
- [12] Bewersdorf, J. *4Pi-konfokale Fluoreszenzmikroskopie mit 1-Photonen-Anregung*. Phd thesis, Ruprecht-Karls-University, (2002)
- [13] Bewersdorf, J., Pick, R., and Hell, S. W. *Multifocal multiphoton microscopy*. Opt. Lett. 23, 655-657 (1998)
- [14] Blanca, C. M., Bewersdorf, J., Hell, S. W. *Single sharp spot in fluorescence microscopy of two opposing lenses*. Appl. Phys. Lett. 79(15), 2321-2323 (2001)
- [15] Blanca, C. M., and Hell, S. W. *Sharp spherical focal spot by dark ring 4pi confocal microscopy*. Single Mol. 2(3), 207-210 (2001)
- [16] Booth, M. J., Neil, M. A. A., Juskaitis, R., and Wilson, T. *Adaptive aberration correction in a confocal microscope*. Proc. Natl. Acad. Sci. USA 99, 5788-5792 (2002)
- [17] Both, M., Kirsch, W. G., Uttenweiler, D., and Fink, R. H. A. *An intrinsic SHG-signal in adult amphibian skeletal muscle fibers*. Pflügers Arch. 443 (2002)
- [18] Both, M., Vogel, M., Fink, R.H.A., and Uttenweiler, D. *Second harmonic generation imaging in muscle fibers*. In confocal, multiphoton, and nonlinear microscopic imaging, Wilson, T., editor, volume 5139, Proc. SPIE (2003)
- [19] Both, M., Vogel, M., Friedrich, O., von Wegner, F., Künsting, T., Fink, R. H., and Uttenweiler, D. *Second harmonic imaging of intrinsic signals in muscle fibers in situ*. J. Biomed. Opt. 9(5), 882-892 (2004)
- [20] Boyd, R. W. *Nonlinear Optics*, Academic Press, Boston, MA (1992)
- [21] Brandon, M., Baldi, P., and Wallace, D.C. *Mitochondrial mutations in cancer*. Oncogene. 25(34), 4647-4662 (2006)
- [22] Bretschneider, S., Eggeling, C., and Hell, S.W. *Breaking the diffraction barrier in fluorescence microscopy by optical shelving*. Phys. Rev. Lett. 98, 218103 (2007)
- [23] Brown, E., McKee, T., DiTomaso, E., Pluen, A., Seed, B., Boucher, Y., and Jain, R. K. *Dynamic imaging of collagen and its modulation in tumors in vivo using second-harmonic generation*. Nat. Med. 9, 796-800 (2003)
- [24] Buist, A. H., Müller, M., Squier, J., and Brakenhoff, G. J. *Realtime two-photon absorption microscopy using multipoint excitation*. J. Microsc. 192, 217-226 (1998)

- [25] Campagnola, P. J., Millard, A. C., Terasaki, M., Hoppe, P. E., Malone, C. J., and Mohler, W. A. *Three-dimensional high-resolution second-harmonic generation imaging of endogenous structural proteins in biological tissues*. Biophys. J. 81, 493-508 (2002)
- [26] Campagnola, P. J., Wei, M., Lewis, A., Loew, L. M. *High-resolution nonlinear optical imaging of live cells by second harmonic generation*. Biophys. J. 77, 3341-3349 (1999)
- [27] Centonze, V. E., and Pawley, J. B. *Tutorial on practical confocal microscopy and use of the confocal test specimen*. Handbook of biological confocal microscopy, Pawley, J. B., editor. 549-570, Plenum Press, New York, NY (1995)
- [28] Chemla, D. S., and Zyss, J. *Nonlinear optical properties of organic molecules and crystals*. Academic Press, New York, NY (1984)
- [29] Chu, S.-W., Chen, S.-Y., Chern, G.-W., Tsai, T.-H., Chen, Y.-C., Lin, B.-L., Sun, C.-K. *Studies of $\chi^{(2)}/\chi^{(3)}$ tensors in submicron-scaled bio-tissues by polarization harmonics optical microscopy*. Biophys. J. 86(6), 3914-3922 (2004)
- [30] Conchello, J. A., and Lichtman, J. W. *Optical sectioning microscopy*. Nat. Meth. 2, 920-931 (2005)
- [31] Denk, W., Strickler, J. H., and Webb, W. W. *2-photon laser scanning fluorescence microscopy*. Science 248, 73-76 (1990)
- [32] Diaspro, A., Chirico, G., Usai, C., Ramoino, P., and Dobrucki, J. *Photobleaching*. Handbook of biological confocal microscopy, Pawley, J. B., editor. 690-702, Plenum Press, New York, NY (2006)
- [33] Duncan, M. D., Reintjes, J., and Manuccia, T. J. *Scanning coherent anti-Stokes Raman microscope*. Optics Lett. 7, 350-352 (1982)
- [34] Dyba, M. and Hell, S. *Focal spots of size $\lambda/23$ open up far-field fluorescence microscopy at 33 nm axial resolution*. Phys. Rev. Lett. 88, 163901 (2002)
- [35] Egner, A., Schrader, M., and Hell, S. W. *Refractive index mismatch induced intensity and phase variations in fluorescence confocal, multiphoton and 4Pi-microscopy*. Opt. Commun. 153, 211-217 (1998)
- [36] Egner, A., Hell, S. W. *Time multiplexing and parallelization in multifocal multiphoton microscopy*. J. Opt. Soc. Am. A Opt. Image Sci. Vis. 17(7), 1192-1201 (2000)

- [37] Egner, A., Jakobs, S., Hell, S. W. *Fast 100 nm resolution three-dimensional microscope reveals structural plasticity of mitochondria in live yeast.* Proc. Natl. Acad. Sci. USA 99(6), 3370-3375 (2002)
- [38] Egner, A., Verrier, S. Goroshkov, A., Söling, H.-D., and Hell, S. W. *4Pi microscopy of the Golgi apparatus in live mammalian cells.* J. Struct. Biol. 147, 70-76 (2004)
- [39] Egner, A., Geisler, C., von Middendorff, C., Bock, H., Wenzel, D., Medda, R., Andresen, M., Stiel, A., Jakobs, S., Eggeling, C., Schönle, A., and Hell, S.W. *Fluorescence nanoscopy in whole cells by asynchronous localization of photoswitching emitters.* Biophys. J. 93, 3285-3290 (2007)
- [40] Fittinghoff, D. N., Wiseman, P. W., and Squier, J. A. *Widefield multiphoton and temporally decorrelated multifocal multi-photon microscopy.* Opt. Exp. 7, 273-279 (2000)
- [41] Fölling, J., Belov, V., Kunetsky, R., Medda, R., Schönle, A., Egner, A., Eggeling, C., Bossi, M., and Hell, S.W. *Photochromic rhodamines provide nanoscopy with optical sectioning.* Angew. Chem. Int. Ed. 46, 6266-6270 (2007)
- [42] Förster, T. *Zwischenmolekulare Energiewanderung und Fluoreszenz.* Annalen der Physik 2, 55-57 (1948)
- [43] Fricke, M., and Nielsen, T. *Two-dimensional imaging without scanning by multifocal multiphoton microscopy.* Appl Opt. 45(15), 2984-2988 (2005)
- [44] Fujita, K., Nakamura, O., Kaneko, T., Kawata, S., Oyamada, M., and Takamatsu, T. *Real-time imaging of two-photon-induced fluorescence with a microlens-array scanner and a regenerative amplifier.* J. Microsc. 194, 528-531 (1999)
- [45] Fujita, K., Nakamura, O., Kaneko, T., Oyamada, M., Takamatsu, T., and Kawata, S. *Confocal multipoint multi-photon excitation microscope with microlens and pinhole arrays.* Opt. Commun. 174, 7-12 (2000)
- [46] Gannaway, J. N. *Second-harmonic imaging in the scanning optical microscope.* Opt. Quant. Electr. 10, 435-439 (1978)
- [47] Gauderon, R. Lukins, P. B., and Sheppard, C. J. R. *Three-dimensional second-harmonic generation imaging with femtosecond laser pulses.* Opt. Kett, 23, 1209-1211 (1998)
- [48] Görisch, S. M., Lichter, P., Rippe, K. *Mobility of multi-subunit complexes in the nucleus: accessibility and dynamics of chromatin subcompartments.* Histochem. Cell. Biol. 123, 217-228 (2005)

- [49] Görisch, S. M., Wachsmuth, M., Ittrich, C., Bacher, C. P., Rippe, K., and Lichter, P. *Nuclear body movement is determined by chromatin accessibility and dynamics*. Proc. Natl. Acad. Sci. USA 101(36), 13221-13226 (2004)
- [50] Gugel, H., Bewersdorf, J., Jakobs, S., Engelhardt, J., Storz, R., and Hell, S. *Cooperative 4π excitation and detection yields 7-fold sharper optical sections in live cell microscopy*. Biophys. J. 87, 4146-4152 (2004)
- [51] Guo, Y., Ho, P. P., Savage, H., Harris, D., Sacks, P., Schantz, S., Liu, F., Zhadin, N., and Alfano, R. R. *Second-harmonic tomography of tissues*. Opt. Lett. 22, 1323-1325 (1997)
- [52] Gustafsson, M. G., Agard, D. A., and Sedat, J. W. *3D widefield microscopy with two objective lenses: experimental verification of improved axial resolution*. In Three-Dimensional Microscopy: Image Acquisition and Processing III, Cogswell, C., Kino, G., and Wilson, T., editors, volume 2655, 62-66, Proc. SPIE, (1996)
- [53] Gustafsson, M.G.L., Agard, D.A., and Sedat, J.W. *Sevenfold improvement of axial resolution in 3D widefield microscopy using two objective lenses*. Proc. SPIE 2412, 147-156 (1995)
- [54] Gustafsson, M., Agard, D., and Sedat, J. I⁵M: *3D widefield light microscopy with better than 100 nm axial resolution*. J. Microsc. 195, 10-16 (1999)
- [55] Hänninen, P.E., Hell, S.W., Salo, J., Soini, E., and Cremer, C. *Two-photon excitation 4π confocal microscope: Enhanced axial resolution microscope for biological research*. Appl. Phys. Lett. 66, 1698-1700 (1995)
- [56] Hegedus, Z. S., and Sarafis, V. *Superresolving filters in confocally scanned imaging systems*. J. Opt. Soc. Am. A, 3(11), 1892-1896 (1986)
- [57] Hein, B., Willig, K. I., and Hell, S. W. *Stimulated emission depletion (STED) nanoscopy of a fluorescent protein-labeled organelle inside a living cell*. PNAS 105(38), 14271-14276 (2008).
- [58] Hell, S. W., Booth, M., Wilms, S., Schmetter, J. C. M., Kirsch, A. K., Arndt-Jovin, D. J., and Jovin, T. M. *Two-photon near- and far-field fluorescence microscopy with continuous-wave excitation*. Opt. Lett. 23, 1238-1240 (1998)
- [59] Hell, S.W. and Stelzer, E.H.K. *Fundamental improvement of resolution with a 4π -confocal fluorescence microscope using two-photon excitation*. Opt. Commun. 93, 277-282 (1992)
- [60] Hell, S.W. *Double confocal microscope*, (1992). EU Patent, No. 0491289

- [61] Hell, S.W. and Kroug, M. *Ground-state depletion fluorescence microscopy, a concept for breaking the diffraction resolution limit*. Appl. Phys. B 60, 495-497 (1995)
- [62] Hell, S.W. *Increasing the resolution of far-field fluorescence light microscopy by point-spread-function engineering*. Topics in Fluorescence Spectroscopy, Lakowicz, J., editor, volume 5, 361-422. Plenum Press, New York, NY (1997)
- [63] Hell, S. W., Reiner, G., Cremer, C., and Stelzer, E. H. K. *Aberrations in confocal fluorescence microscopy induced by mismatches in refractive index*. J. Microsc. 169(Pt3), 391-405 (1993)
- [64] Hell, S., Jakobs, S., and Kastrup, L. *Imaging and writing at the nanoscale with focused visible light through saturable optical transitions*. Appl. Phys. A 77, 859-860 (2003)
- [65] Hell, S. W., and Stelzer, E. H. K., *Fundamental improvement of resolution with a 4Pi-confocal fluorescence microscope using two-photon excitation*. Opt. Commun. 93, 277-282 (1992)
- [66] Hell, S.W. and Wichmann, J. *Breaking the diffraction resolution limit by stimulated emission: STED*. Opt.Lett. 19(11), 780-782(1994)
- [67] Hell, S. W., Schrader, M., Hänninen, P.E., and Soini, E. *Resolving fluorescence beads at 100-200 nm distance with a two-photon 4Pi-microscope working in the near infrared*. Opt. Commun. 117, 20-24 (1995)
- [68] Hellwarth, R., and Christensen, P. *Nonlinear optical microscopic examination of structures in polycrystalline ZnSe*. Opt. Commun. 12, 318-322 (1974)
- [69] Hess, S.T., Girirajan, T.P.K., and Mason, M.D. *Ultra-high resolution imaging by fluorescence photoactivation localization microscopy*. Biophys. J. 91(11), 4258-4272 (2006)
- [70] Huang, B., Wang, W., Bates, M., and Zhuang, X. *Three-dimensional super-resolution imaging by stochastic optical reconstruction microscopy*. Science Express 319, 810-813 (2008)
- [71] Jakobs, S., Martini, N., Schauss, A. C., Egner, A., Westermann, B., and Hell, S. W. *Spatial and temporal dynamics of budding yeast mitochondria lacking the division component Fis1p*. J. Cell. Sci. 116(Pt 10), 2005-2014 (2003)
- [72] Jegou, T., Chung, I., Heuvelman, G., Wachsmuth, M., Görisch, S. M., Greulich-Bode, K., Boukamp, P., Lichter, P., and Rippe, K. *Dynamics of telomeres and PML nuclear bodies in a telomerase negative human cell line*. Mol. Biol. Cell. 20(7), 2070-2082 (2009)

- [73] Jureller, J. E., Kim, H. Y., and Scherer, N. F. *Stochastic scanning multiphoton multifocal microscopy*. Opt. Exp. 14(8), 3406-3414 (2006)
- [74] Kano, H., Jakobs, S., Nagorni, M., and Hell, S. W. *Dual-color 4Pi-confocal microscopy with 3D-resolution in the 100 nm range*. Ultramicroscopy 90, 207-213 (2002)
- [75] Kawano, H., Kogure, T., Abe, Y., Mizuno, H., and Miyawaki, A. *Two-photon dual-color imaging using fluorescent proteins*. Nat. Meth. 5, 373-374 (2008)
- [76] Klar, T.A., Jakobs, S., Dyba, M., Egner, A., and Hell, S.W. *Fluorescence microscopy with diffraction resolution limit broken by stimulated emission*. Proc. Natl.Acad. Sci. USA 97, 8206-8210 (2000)
- [77] Kobayashi, M., Fujita, K., Kaneko, T., Takamatsu, T., Nakamura, O., and Kawata, S. *Second-harmonic-generation microscope with a microlens array scanner*. Opt. Lett. 27, 1324 (2002)
- [78] König, K., Becker, W., Fischer, P., Reimann, I., and Halbhüser, K.-J. *Pulse-length dependence of cellular response to intense near-infrared laser pulses in multiphoton microscopes*. Opt. Lett. 24, 113-115 (1999)
- [79] König, K. *Cell damage during multi-photon microscopy*. In Handbook of biological confocal microscopy, Pawley, J. B., editor. 680-690, Plenum Press, New York, NY (2006)
- [80] König, K. *Multiphoton microscopy in life sciences*. J. Microsc. (Oxford) 200, 83-104 (2000)
- [81] Kwong, J.Q., Beal, M.F., and Manfredi, G. *The role of mitochondria in inherited neurodegenerative diseases*. J. Neurochem. 97, 1659-1675 (2006)
- [82] Lang, M.C., Staudt, T., Engelhardt, J., and Hell, S.W. *4Pi microscopy with negligible sidelobes*. New J. Phys. 10, 1-13 (2008)
- [83] Lang, M., Müller, T., Engelhardt, J., and Hell, S.W. *4Pi microscopy of type A with 1-photon excitation in biological fluorescence imaging*. Optics Express 15(5), 2459-2467 (2007)
- [84] Lang, M. C. *4Pi-Mikroskopie mit ultra-hohen Aperturwinkeln*. PhD-Thesis, <http://www.ub.uni-heidelberg.de/archiv/7454> (2007)
- [85] Lang, M., Jegou, T., Chung, I., Richter, K., Münch, S., Udvarhelyi, A., Cremer, C., Hemmerich, P., Engelhardt, J., Hell, S. W., and Rippe, K. *The ultrastructure of PML nuclear bodies*. submitted

- [86] Lanni, F., Bailey, B., Farkas, D. L., and Taylor, D. L. *Excitation field synthesis as a means for obtaining enhanced axial resolution in fluorescence microscopy*. Bioimaging 1, 187-192 (1994)
- [87] Lvque-Fort, S., Fontaine-Aupart, M.P., Roger, G., and Georges, P. *Fluorescence-lifetime imaging with a multifocal two-photon microscope*. Opt. lett. 29(24), 2884-2886 (2004)
- [88] Martnez-Corral, M. *Sidelobe decline in single-photon 4π microscopy by Toraldo rings*. Micron 34, 319-325 (2003)
- [89] Martnez-Corral, M., Ibnez-Lpez, C., Caballero, M. T., Munoz-Escriv, L., and Saavedra, G. *Three-ring filters increase the effective NA up to 1.46 in optical sectioning fluorescence microscopy*. J. Phys. D: Appl. Phys. 36, 1669-1674 (2003)
- [90] McCabe, E. M., Fewer, D. T., Ottewill, A. C., Hewlett, S. J., and Hegarty, J. *Direct-view microscopy: optical sectioning strength for finite-sized, multiple-phinhole arrays*. J. Microsc. (Oxford) 184, 95-105 (1996)
- [91] Medda, R., Jakobs, S., Hell, S. W., and Bewersdorf, J. *4π microscopy of quantum dot-labeled cellular structures*. J. Struct. Biol. 156, 517-523 (2006)
- [92] Mertz, J., Moreaux, L. *Second-harmonic generation by focused excitation of inhomogeneously distributed scatterers*. Opt. Commun. 196, 325-330 (2001)
- [93] Minsky, M. *Memoir on inventing the confocal scanning microscope*. Scanning 10, 128-138 (1988)
- [94] Minsky, M. *Microscopy apparatus*, (1957). U.S. Patent, No. 3013467
- [95] Molenaar, C., Wiesmeijer, K., Verwoerd, N. P., Khazen, S., Eils, R., Tanke, H. J., and Dirks, R. W. *Visualizing telomere dynamics in living mammalian cells using PNA probes*. Embo. J. 22, 6631-6641 (2003)
- [96] Moreaux, L., Sandre, O., Charpak, S., Blanchard-Desce, M., and Mertz, J. *Coherent scattering in multi-harmonic light microscopy*. Biophys. J. 80(3), 1568-1574 (2001)
- [97] Moreaux, L., Sandre, O., Mertz, J. *Membrane imaging by second-harmonic generation microscopy*. J. Opt. Soc. Am. B 17, 1685-1694 (2000)
- [98] Müller, M., and Schins, J. M. *Imaging the thermodynamic state of lipid membranes with multiplex CARS microscopy*. J. Phys. Chem. B 106, 3715-3723 (2002)

- [99] Müller, M., Squier, J., Wilson, K. R., and Brakenhoff, G. J. *3D microscopy of transparent objects using third-harmonic generation*. J. Microsc. 191, 266-274 (1998)
- [100] Nagorni, M., and Hell, S. W. *Coherent use of opposing lenses for axial resolution increase in fluorescence microscopy. I. Comparative study of concepts*. J. Opt. Soc. Am. A 18(1), 36-48 (2001)
- [101] Nagorni, M., and Hell, S. W. *Coherent use of opposing lenses for axial resolution increase in fluorescence microscopy. II. Power and limitations of nonlinear image restoration*. J. Opt. Soc. Am. A 18(1), 49-54 (2001)
- [102] Nielsen, T., Fricke, M., Hellweg, D., and Andresen, P. *High efficiency beam splitter for multifocal multiphoton microscopy*. J. Microsc. 201, 368-376 (2001)
- [103] Nishikawa, T. and Araki, E. *Impact of mitochondrial ROS production in the pathogenesis of diabetes mellitus and its complications*. Antioxid. Redox Signal. 9, 343-353 (2007)
- [104] Nishino, I., Kobayashi, O., Goto, Y.-I., Kurihara, M., Kumagai, K., Fujita, T., Hashimoto, K., Horai, S., and Nonaka, I. *A new congenital muscular dystrophy with mitochondrial structural abnormalities*. Muscle. Nerv. 21, 40-47 (1998)
- [105] Patterson, G. H., and Piston, D. W. *Photobleaching in two-photon excitation microscopy*. Biophys. J. 78, 2159-2162 (2000)
- [106] Pawley, J. *Handbook of biological confocal microscopy* Plenum Press, New York (1995)
- [107] Plecit-Hlavat, L., Lessard, M., Santorov, J., Bewersdorf, J., Jezek, P. *Mitochondrial oxidative phosphorylation and energetic status are reflected by morphology of mitochondrial network in INS-1E and HEP-G2 cells viewed by 4Pi microscopy*. Biochim. Biophys. Acta. 1777(7-8), 834-846 (2008)
- [108] Richards, B. and Wolf, E. *Electromagnetic diffraction in optical systems II. Structure of the image field in an aplanatic system*. Proc. R. Soc. Lond. A 253, 358-379 (1959)
- [109] Roth, S., and Freund, I. *Optical second-harmonic scattering in rat tail tendon*. Biopolymers 20, 1271-1290 (1981)
- [110] Roth, S., and Freund, I. *Second-harmonic generation in collagen*. J. Chem. Phys. 70, 1637-1643 (1979)

- [111] Rust, M.J., Bates, M., and Zhuang, X. *Sub-diffraction-limited imaging by stochastic optical reconstruction microscopy (STORM)*. Nat. Meth. 3, 793-796 (2006)
- [112] Sacconi, L., Froner, E., Antolini, R., Taghizadeh, M. R., Choudhury, A., and Pavone, F. S. *Multiphoton multifocal microscopy exploiting a diffractive optical element*. Opt. Lett. 28(20), 1918-1920 (2003)
- [113] Sales, T. R. M., and Morris, G. M. *Axial superresolution with phase-only pupil filters*. Opt. Commun. 156, 227-230 (1998)
- [114] Schmidt, R., Wurm, C. A., Jakobs, S., Engelhardt, J., Egner, A., and Hell, S. W. *Spherical nanosized focal spot unravels the interior of cells*. Nat. Meth. 5, 539-544 (2008)
- [115] Schrader, M., Bahlmann, K., Biese, G., and Hell, S. W. *4Pi-confocal imaging in fixed biological specimens*. Biophys. J. 75, 1659-1668 (1998)
- [116] Selvin, P. R. *The renaissance of fluorescence resonance energy transfer*. Nature Struct. Biol. 7(9), 730-734 (2000)
- [117] Sheppard, C. J. R., Calvert, G., and Wheatland, M. *Focal distribution for superresolving toraldo filters*. J. Opt. Soc. Am. A, 15(4), 849-856 (1998)
- [118] Sheppard, C. J. R., and Wilson, T. *The theory of the direct-view confocal microscope*. J. Microsc. (Oxford) 124, 107-117 (1981)
- [119] Staudt, T., Lang, M., Medda, R., Engelhardt, J., and Hell, S.W. *2,2-thiodiethanol: a new water soluble mounting medium for high resolution optical microscopy*. Microsc. Res. Tech. 70, 1-9 (2007)
- [120] Stoller, P., Kim, B. M., Rubenchik, A. M., Reiser, K. M., and Da Silva, L. B. *Polarization-dependent optical second-harmonic imaging of a rat tail tendon*. J. Biomed. Opt. 7, 205-214 (2002)
- [121] Stoller, Reiser, K. M., Celliers, P. M., and Rubenchick, A. M. *Polarization-modulated second-harmonic generation in collagen*. Biophys. J. 82, 3330-3342 (2002)
- [122] Straub, M., and Hell, S. W. *Multifocal multi-photon microscopy: A fast and efficient tool for 3-D fluorescence imaging*. Bioimaging 6, 177-185 (1998)
- [123] Toraldo di Francia, G. *Supergain antennas and optical resolving power*. Nuovo Cimento Suppl. 9, 426-435 (1952)

- [124] Wang, W., Wyckoff, J. B., Frohlich, V. C., Oleynikov, Y., Huttelmaier, S., Zavadil, J., Cermak, L., Bottinger, E. P., Singer, R. H., White, J. G., Segall, J. E., and Condeelis, J. S. *Single cell behavior in metastatic primary mammary tumors correlated with gene expression patterns revealed by molecular profiling.* Cancer Res. 62, 6278-6288 (2002)
- [125] Westphal, V., Rizzoli, S. O., Lauterbach, M. A., Kamin, D., Jahn, R. and Hell, S. W. *Video-Rate Far-Field Optical Nanoscopy Dissects Synaptic Vesicle Movement* Science 320, 246-249 (2008)
- [126] Williams, R. M., Zipfel, W. R., Webb, W. W. *Interpreting second-harmonic generation images of collagen I fibrils.* Biophys. J. 88(2), 1377-1386 (2005)
- [127] Wolf, E. *Electromagnetic diffraction in optical systems I. An integral representation of the image field.* Proc. R. Soc. Lond. A 253, 349-357 (1959)
- [128] Yeager, T. R., Neumann, A. A., Englezou, A., Huschtscha, L. I., Noble, J. R., and Reddel, R. R. *Telomerase-negative immortalized human cells contain a novel type of promyelocytic leukemia (PML) body.* Cancer Res. 59, 4175-4179 (1999)
- [129] Yelin, D., Oron, D., Korkotian, E., Segal, M., and Silberberg, Y. *Third-harmonic microscopy with a titanium-sapphire laser.* Appl. Phys. B 74(Suppl), 97-101 (2002)
- [130] Zumbusch, A., Holtom, G. R., and Xie, X. S. *Three-dimensional vibrational imaging by coherent anti-Stokes Raman scattering.* Phys. Rev. Lett 82, 4142-4145 (1999)

Acknowledgments

This work was performed at the German Cancer Research Center (DKFZ) in Heidelberg. I would like to express my sincere thanks and appreciation to the following persons and organizations who have considerably contributed to the success of this thesis:

- *Prof. Dr. Stefan W. Hell*, head of the department of Nanobiophotonics at the Max-Planck-Institute for Biophysical Chemistry (MPIBPC) in Göttingen, for the exceptional environment he provided to conduct scientific research in the outstandingly important and interesting field of live cell imaging.
- *Prof. Dr. Rainer H. Fink* at the Institute of Physiology and Pathophysiology, University of Heidelberg, for his interest in my work and his willingness to referee my thesis.
- *The Landesstiftung Baden-Württemberg* for financial support.
- *Dr. Johann Engelhardt* at the High Resolution Optical Microscopy Department at the DKFZ for his assistance, his expertise, his manifold contributions, invaluable discussions and dedication to this project from the beginning as well as his personal support.
- *My colleagues* in the High Resolution Optical Microscopy Department at the DKFZ for their manifold support, advice and real friendship.
- I would like to thank all people I have met and was connected to in close collaborations. For their interest in 4Pi microscopy and their willingness to contribute fascinating biological challenges to that branch of high resolution microscopy. Special thanks to *Sebastian Schürmann* at the Institute of Physiology and Pathophysiology, University of Heidelberg, to *Stefan Jakobs* at the Nanobiophotonics Department at the Max-Planck-Institute for Biophysical Chemistry (MPIBPC) in Göttingen, to *Sarah Osterwald* of the Genome Function and Organization Group at Bioquant, University of Heidelberg and last but not least *Jasmin Zahn* at the Biophysical Institute, University of Heidelberg for providing the samples described in my thesis. These people have contributed largely to the success of this thesis.

Bibliography

- I would also like to thank *Heinrich Rühle* and colleagues from the mechanical workshop of the DKFZ providing for customized parts and manufacturing even intricate microscope components.
- Special thanks also to *Jürgen Sauter, Johann Engelhardt, Matthias Reuss, Thorsten Staudt, Jale Özcelik, Franziska Curdt, Pit Bingen, Hans-Ludwig Hahn, Thomas Hahn, Tanja Schmock* and last but not least *Christian Wegmann* for proof-reading the manuscripts of this thesis. I really do apologize to have tortured you with endless sentences in bad grammar and innumerable -ings and -leys!
- Last but not least my sincere respect and very special thanks to *Jürgen Sauter*, my husband. For his never-ending manifold support and love. And to my parents *Inge* and *Hans-Ludwig Hahn* for their constant support and always being there.